Monthly Notices
of the
ROYAL ASTRONOMICAL SOCIETY

Mon. Not. R. Astron. Soc. **427,** 1666–1701 (2012) doi:10.1111/j.1365-2966.2012.22087.x

The morphologies of massive galaxies at $1 < z < 3$ in the CANDELS-UDS field: compact bulges, and the rise and fall of massive discs

V. A. Bruce,[1⋆] J. S. Dunlop,[1] M. Cirasuolo,[1,2] R. J. McLure,[1] T. A. Targett,[1] E. F. Bell,[3] D. J. Croton,[4] A. Dekel,[5] S. M. Faber,[6] H. C. Ferguson,[7] N. A. Grogin,[7] D. D. Kocevski,[6] A. M. Koekemoer,[7] D. C. Koo,[6] K. Lai,[6] J. M. Lotz,[7] E. J. McGrath,[6] J. A. Newman[8] and A. van der Wel[9]

[1]*SUPA† Institute for Astronomy, University of Edinburgh, Royal Observatory, Edinburgh EH9 3HJ*
[2]*UK Astronomy Technology Centre, Science and Technology Facilities Council, Royal Observatory, Edinburgh EH9 3HJ*
[3]*Department of Astronomy, University of Michigan, 500 Church Street, Ann Arbor, MI 48109, USA*
[4]*Centre for Astrophysics and Supercomputing, Swinburne University of Technology, PO Box 218, Hawthorn, VIC 3122, Australia*
[5]*Racah Institute of Physics, The Hebrew University, Jerusalem 91904, Israel*
[6]*UCO/Lick Observatory, University of California, Santa Cruz, CA 95064, USA*
[7]*Space Telescope Science Institute, 3700 San Martin Drive, Baltimore, MD 21218, USA*
[8]*University of Pittsburgh, Pittsburgh, PA 15260, USA*
[9]*Max-Planck Institut für Astronomie, Königstuhl 17, D-69117 Heidelberg, Germany*

Accepted 2012 September 7. Received 2012 September 7; in original form 2012 June 20

ABSTRACT

We have used high-resolution, *Hubble Space Telescope*, near-infrared imaging to conduct a detailed analysis of the morphological properties of the most massive galaxies at high redshift, modelling the WFC3/IR H_{160}-band images of the $\simeq$200 galaxies in the CANDELS-UDS field with photometric redshifts $1 < z < 3$, and stellar masses $M_* > 10^{11}\,\mathrm{M}_\odot$. We have explored the results of fitting single-Sérsic and bulge+disc models, and have investigated the additional errors and potential biases introduced by uncertainties in the background and the on-image point spread function. This approach has enabled us to obtain formally acceptable model fits to the WFC3/IR images of >90 per cent of the galaxies. Our results indicate that these massive galaxies at $1 < z < 3$ lie both on and below the local size–mass relation, with a median effective radius of $\sim$2.6 kpc, a factor of $\simeq$2.3 smaller than comparably massive local galaxies. Moreover, we find that bulge-dominated objects in particular show evidence for a growing bimodality in the size–mass relation with increasing redshift, and by $z > 2$ the compact bulges display effective radii a factor of $\simeq$4 smaller than local ellipticals of comparable mass. These trends also appear to extend to the bulge components of disc-dominated galaxies. In addition, we find that, while such massive galaxies at low redshift are generally bulge-dominated, at redshifts $1 < z < 2$ they are predominantly mixed bulge+disc systems, and by $z > 2$ they are mostly disc-dominated. The majority of the disc-dominated galaxies are actively forming stars, although this is also true for many of the bulge-dominated systems. Interestingly, however, while most of the quiescent galaxies are bulge-dominated, we find that a significant fraction (25–40 per cent) of the most quiescent galaxies, with specific star formation rates sSFR $< 10^{-10}\,\mathrm{yr}^{-1}$, have disc-dominated morphologies. Thus, while our results show that the massive galaxy population is undergoing dramatic changes at this crucial epoch, they also suggest that the physical mechanisms which quench star formation activity are not simply connected to those responsible for the morphological transformation of massive galaxies into present-day giant ellipticals.

⋆E-mail: vab@roe.ac.uk
†Scottish Universities Physics Alliance.

Key words: galaxies: elliptical and lenticular, cD – galaxies: evolution – galaxies: high-redshift – galaxies: spiral – galaxies: structure.

1 INTRODUCTION

The study of the high-redshift progenitors of today's massive galaxies can provide us with invaluable insights into the key mechanisms that shape the evolution of galaxies in the high-mass regime, placing important constraints on current models of galaxy formation and evolution. In recent years the new generation of optical–infrared surveys have revealed that a substantial population of massive galaxies is already in place by $z \simeq 2$, and that the star formation activity in a significant fraction of these objects largely ceases around this time, ∼3 Gyr after the big bang (e.g. Fontana et al. 2004; Glazebrook et al. 2004; Drory et al. 2005). These results have driven the modification of models of galaxy formation to include additional mechanisms for the quenching of star formation activity in massive galaxies at early times, such as active galactic nucleus (AGN) feedback (e.g. Granato et al. 2004; Bower et al. 2006; Croton et al. 2006; De Lucia & Blaizot 2007).

However, explaining the number densities and ages of massive galaxies at high redshift is only part of the challenge, as recent advances in imaging capabilities are now providing meaningful data on their sizes and morphologies during the crucial cosmological epoch $1 < z < 3$, when global star formation activity in the Universe peaked. In particular, over the last ≃5 years, deep/high-resolution ground-based and space-based [i.e. *Hubble Space Telescope* (*HST*)] surveys have revealed that a significant fraction of massive galaxies at $z > 1$ are surprisingly compact (e.g. Daddi et al. 2005; Trujillo et al. 2006, 2007; Cimatti et al. 2008; Franx et al. 2008; Damjanov et al. 2009; Targett et al. 2011), with derived effective radii ($R_e < 2$–3 kpc) and stellar mass measurements which place these galaxies well below the local galaxy size–mass relation, as derived from the Sloan Digital Sky Survey (SDSS) (Shen et al. 2003). Furthermore, it appears that the largest divergence from local values arises in galaxies which exhibit very little sign of ongoing star formation (e.g. Toft et al. 2007; Kriek et al. 2009; McLure et al. 2012).

As befits their potential importance, these studies have been carefully scrutinized to investigate possible sources of bias in the measurement of galaxy size and mass (Muzzin et al. 2009; Mancini et al. 2010). A particular concern has been the perceived potential for galaxy scalelengths to be underestimated due to low signal-to-noise ratio imaging (which might be inadequate to reveal faint extended envelopes), morphological *k*-corrections, or selection effects related to surface brightness bias (e.g. van der Wel et al. 2009). However, the latest generation of deeper rest-frame optical morphological studies have thus far provided mounting evidence for the truly compact nature of many high-redshift galaxies (e.g. van Dokkum et al. 2010; Cameron et al. 2011; Ryan et al. 2012; Szomoru, Franx & van Dokkum 2012). It should also be noted that the existence of such compact objects at early times, while perhaps initially unexpected, is in fact a natural prediction of modern galaxy-formation simulations (e.g. Khochfar & Silk 2006; Hopkins et al. 2010a; Wuyts et al. 2010). Moreover, several local studies have now clarified the relative dearth of comparably compact systems surviving to the present day (Trujillo et al. 2009; Taylor et al. 2010), strengthening the argument that the compact high-redshift systems must undergo a period of significant size evolution with limited mass growth in order to reach the local galaxy size–mass relation by $z = 0$ (e.g. McLure et al. 2012).

Various physical mechanisms have been suggested as the primary drivers of this process, including major or minor mergers (Khochfar & Silk 2006; Naab et al. 2007; Hopkins et al. 2009; Shankar et al. 2011) or AGN feedback (Fan et al. 2008, 2010). All of these scenarios can potentially induce sufficient size growth, but there are problems with some of the accompanying predictions of these growth mechanisms. For the major-merger scenario these include reconciling the number of major mergers required to facilitate the required size growth with the number of major mergers expected since $z \sim 1$ from *N*-body simulations (Hopkins et al. 2010b), and the disparity between the inferred large mass growth of these (already massive) systems and the latest estimates of the local galaxy stellar mass function (Baldry et al. 2012; McLure et al. 2012). These problems, coupled with results from numerical simulations, which show that AGN-driven expansion occurs when the galaxy is much younger than the typical ages of high-redshift compact objects (>0.5 Gyr) (Ragone-Figueroa & Granato 2011), have now led most researchers to conclude in favour of a picture in which most size growth since $z \simeq 2$ is driven by minor gas-poor mergers in the outer regions of galaxies, building up stellar haloes around compact cores, with (relatively) small overall mass growth (Bezanson et al. 2009; Naab, Johansson & Ostriker 2009; Hopkins et al. 2010b; van Dokkum et al. 2010; McLure et al. 2012; Trujillo, Carrasco & Ferré-Mateu 2012).

In addition to the basic question of how these compact high-redshift galaxies evolve in size, there is also still much debate about how these massive galaxies evolve in terms of their fundamental morphological type. Extensive studies of the local Universe have revealed a bimodality in the colour–morphology plane, with spheroidal galaxies typically inhabiting the red sequence and disc galaxies making up the blue cloud (Baldry et al. 2004; Driver et al. 2006; Drory & Fisher 2007). However, recent studies at both low (Bamford et al. 2009; Masters et al. 2010) and high redshift (McGrath et al. 2008; Stockton et al. 2008; Cameron et al. 2011; van der Wel et al. 2011; McLure et al. 2012) have uncovered a significant population of passive disc-dominated galaxies, providing evidence that the physical processes which quench star formation may be distinct from those responsible for driving morphological transformations. This result is particularly interesting in light of the latest morphological studies of high-redshift massive galaxies by Buitrago et al. (2011) and van der Wel et al. (2011) who find that, in contrast to the local population of massive galaxies (which is dominated by bulge morphologies), by $z \simeq 2$ massive galaxies are predominantly disc-dominated systems.

In this paper we attempt to provide significantly improved clarity on these issues by exploiting the new near-infrared *HST* WFC3/IR imaging provided by the CANDELS survey (Grogin et al. 2011; Koekemoer et al. 2011) of the central region of the UKIDSS UDS field. This provides the necessary combination of depth, angular resolution and area to enable the most detailed and robust study to date of the rest-frame optical morphologies of massive galaxies at $1 < z < 3$. We have also taken this opportunity to properly explore a number of challenging technical issues in the field, investigating the extent to which our results are robust to the method and

accuracy with which both the background and on-image point spread function (PSF) is determined, and undertaking both single- and multiple-component axisymmetric modelling (with allowance for an additional point-like component contribution where required). Unlike many previous studies in this area, we have placed special emphasis on obtaining a formally acceptable model fit to the observed galaxy images, in order to enable meaningful errors to be placed on the key morphological parameters extracted from our analysis.

This paper is structured as follows. First, since the CANDELS *HST* WFC3/IR near-infrared data have also proved crucial in the selection of our sample of massive galaxies, in Section 2 we summarize the CANDELS and associated ground-based and *Spitzer* data sets in the central region of the UDS field, and explain how these were analysed to produce the high-mass, high-redshift galaxy sample which we have then subjected to morphological analysis. In Section 3 we present our general morphological model-fitting technique and then, in Section 4 we detail our single-Sérsic model-fitting procedure, explain how meaningful errors on parameter values were determined, and describe our investigation of possible biases. This is followed by a description of our bulge+disc decomposition analysis in Sections 5 and 6. In Section 7 we present our new results on the size–mass relation, and combine our derived morphologies with specific star formation rate (sSFR) and redshift information to explore how bulge and disc fractions vary as a function of star formation activity and redshift. Finally, in Section 8 we discuss the implications of our results for our understanding of galaxy growth, morphological evolution, and the quenching of star formation activity, before closing with a summary of our main conclusions in Section 9. Throughout we quote magnitudes in the AB system, and calculate all physical quantities assuming a Lambda cold dark matter (ΛCDM) universe with $\Omega_{\rm m} = 0.3$, $\Omega_\Lambda = 0.7$ and $H_0 = 70\,{\rm km\,s^{-1}\,Mpc^{-1}}$.

2 DATA AND SAMPLE SELECTION

2.1 *HST* imaging and basic sample definition

The main aim of this paper is to present a comprehensive and robust analysis of the morphological properties of a significant sample of the most massive galaxies in the redshift range $1 < z < 3$. In order to achieve this we have focused our study on the UKIDSS Ultra Deep Survey (UDS; Lawrence et al. 2007), the central region of which has been imaged with *HST* WFC3/IR as part of the CANDELS multicycle treasury programme (Grogin et al. 2011; Koekemoer et al. 2011). The CANDELS near-infrared data comprise 4×11 WFC3/IR tiles covering a total area of 187 arcmin^2 in both the $F125W$ and $F160W$ filters (hereafter J_{125} and H_{160}). The integration times are (4/3)-orbit per pointing in H_{160} and (2/3)-orbit in J_{125}, giving 5σ point-source depths of 27.1 and 27.0 (AB mag), respectively. For this study we have used the catalogue from Cirasuolo et al. (in preparation) as a master sample. This sample was constructed using SEXTRACTOR (Bertin & Arnouts 1996) version 2.8.6 run on the H_{160} mosaic and then cut at a limiting total magnitude of 24.5 (i.e. a factor of 10 brighter than the 5σ point-source detection limit) to ensure that a reliable morphological analysis was possible (see Grogin et al. 2011); in practice the subsequent stellar mass cuts described below result in a sample in which >90 per cent of the objects under study have $H_{160} < 23$ (and so we are typically dealing with $>50\sigma$ detections).

2.2 Supporting multiwavelength data

In addition to the near-infrared imaging provided by *HST*, the data sets we make use of for sample selection (i.e. photometric redshifts, stellar mass determination, SFRs and star formation histories) include: deep optical imaging in the *B*-, *V*-, *R*-, *i*′- and *z*′-band filters from the Subaru *XMM–Newton* Deep Survey (SXDS; Sekiguchi et al. 2005; Furusawa et al. 2008); *U*-band imaging obtained with MegaCam on Canada–France–Hawaii Telescope; *J*-, *H*- and *K*-band United Kingdom Infrared Telescope (UKIRT) WFCAM imaging from Data Release 8 (DR8) of the UKIDSS UDS; and *Spitzer* 3.6-, 4.5-, 5.8- and 8.0-μm IRAC and 24-μm MIPS imaging from the SpUDS legacy programme (PI Dunlop).

2.3 Photometric redshifts

A multiwavelength catalogue for photometric redshift fitting was constructed for the CANDELS master sample using the dual-image mode in SEXTRACTOR with a ground-based PSF-matched H_{160} mosaic as the detection image, and including U, B, V, R, i', z', J, H, K, 3.6 μm, 4.5 μm, J_{125} and H_{160} photometry. For full details of the catalogue extraction, PSF matching and treatment of source deblending, see Cirasuolo et al. (in preparation).

Following Cirasuolo et al. (in preparation), photometric redshifts for this master sample were determined using a χ^2 fitting procedure, which utilizes both empirical and synthetic templates to characterize the spectral energy distribution (SED) of galaxies. The synthetic templates used here have been generated from the stellar population synthesis models of Bruzual & Charlot (2003) (BC03), assuming a Chabrier initial mass function (IMF). A fixed solar metallicity was used with a variety of single-component, exponentially decaying, star formation histories with e-folding times in the range $0 \leq \tau\,({\rm Gyr}) \leq 10$, where the age of the galaxy at each redshift was not allowed to exceed the age of the Universe at that redshift. Absorption from the intergalactic medium was accounted for using the prescriptions of Madau (1995), and the Calzetti et al. (2000) obscuration law was used to account for reddening due to dust within the range $0 \leq A_V \leq 4$. In order to test the accuracy of the photometric redshifts they were compared with known spectroscopic estimates where possible. This comparison demonstrated remarkably good agreement, with a distribution of $(z_{\rm spec} - z_{\rm phot})/(1 + z_{\rm spec})$ centred on zero, with a standard deviation $\sigma = 0.03$.

2.4 Stellar masses

Stellar masses were obtained directly from the best-fitting SED used to obtain the photometric redshift (for a full discussion on the stellar mass fitting procedure see Cirasuolo et al., in preparation). There is currently much discussion in the literature over the dependence of stellar mass estimates on the stellar population synthesis models employed during the fitting procedure, and more specifically on the treatment of thermally pulsating asymptotic giant branch (TP-AGB) stars. In particular it has been found that models including higher contributions from the TP-AGB population [Maraston 2005 (M05); Charlot & Bruzual, private communication (CB07)] lead to stellar masses on average ∼0.15 dex smaller (Pozzetti et al. 2007; Ilbert et al. 2010) than those derived using BC03 templates. However, the models with a strong contribution from the TP-AGB have now been essentially ruled out (Kriek et al. 2010; Zibetti et al. 2012), and in any case the TP-AGB contribution is only important in the specific age range ≃0.5–1.0 Gyr.

In this work we have therefore chosen to use the BC03 models, and to define the most massive galaxies by the mass threshold $M_* > 10^{11}\,\mathrm{M}_\odot$, as derived from single-component tau-models. The effects of including 'double burst models' in the SED fitting have been explored by Michałowski et al. (2012) and McLure et al. (2012). However, while Michałowski et al. (2012) show that two-component models can produce significantly larger stellar masses than single-component models for extreme starbursting objects such as submillimetre galaxies, McLure et al. (2012) report that the mass difference is relatively small for more typical $z \simeq 1$–2 galaxies ($\langle \Delta M_* \rangle \simeq 0.1$ dex), presumably because an exponentially decaying star formation history provides a reasonable description of reality for most massive galaxies at these epochs. Accordingly, for the present study we decided to adopt the stellar mass estimates obtained with the BC03 tau-models, in order to most easily facilitate direct comparison with previous studies.

In addition to inconsistencies in the stellar masses derived from various stellar population synthesis models, there is a further added offset in quoted stellar masses introduced by the IMF used in the fitting. To ease comparisons with previous studies, throughout this paper we convert stellar masses quoted in the literature to those that would be obtained using the BC03 models with a Chabrier IMF using the following conversions: $\log_{10} M_{*,\mathrm{M05}} = \log_{10} M_{*,\mathrm{BC03}} - 0.15$ (Cimatti et al. 2008); $\log_{10} M_{*,\mathrm{CB07}} = \log_{10} M_{*,\mathrm{BC03}} - 0.2$ (Salimbeni et al. 2009); $\log_{10} M_{*,\mathrm{Chabrier}} = \log_{10} M_{*,\mathrm{Salpeter}} - 0.23$ (Cimatti et al. 2008); $\log_{10} M_{*,\mathrm{Chabrier}} = \log_{10} M_{*,\mathrm{Kroupa}} - 0.04$ (Cimatti et al. 2008).

2.5 Final sample selection

From the master catalogue described above we define our sample as the most massive galaxies with $M_* > 10^{11}\,\mathrm{M}_\odot$ in the redshift range $1 \leq z_{\mathrm{phot}} \leq 3$. This gives a total of 215 galaxies identified from the H_{160} mosaic and provides a mass-complete sample where, for our cut at $H_{160} = 24.5$, the mass completeness limit is $M_* < 10^{11}\,\mathrm{M}_\odot$ over the full redshift range of this study (see Cirasuolo et al., in preparation, for a full discussion of mass completeness).

3 MORPHOLOGIES: 2D MODELLING

We have employed the GALFIT (Peng et al. 2002) morphology fitting code to determine the morphological properties for all 215 objects in our sample. GALFIT is a 2D fitting routine that can be used to model the surface brightness profile of an observed galaxy with pre-defined functions such as a Sérsic light profile (de Vaucouleurs 1948; Sérsic 1968):

$$\Sigma(r) = \Sigma_{\mathrm{e}} \exp\left[-\kappa\left(\left(\frac{r}{r_{\mathrm{e}}}\right)^{1/n} - 1\right)\right], \quad (1)$$

where Σ_{e} is the surface brightness at the effective radius r_{e}, n (the Sérsic index) is a measure of the concentration of the light profile and κ is a a correction factor coupled to n such that half of the total flux of the object lies with r_{e} [obtained by numerically solving $\Gamma(2n) = 2\gamma(2n, \kappa)$].

It is well established that the robustness of the GALFIT output depends heavily on the input files, such as the background-subtracted image, the σ map and the PSF (see Häussler et al. 2007 for a full discussion of these issues). As a result we have conducted rigorous tests of our fitting procedure to ensure that the morphological parameters that we determine using the GALFIT code are not biased by the realistic uncertainties in these inputs. Specifically, in the next section we summarize and illustrate the results of thorough tests of the robustness of the derived morphological parameters with respect to the accuracy of the adopted PSF, and the implementation of various background-level determinations (further details of these tests are provided in Appendixes A and B). These tests are carried out exclusively on the H_{160} mosaic, the reddest band accessible to *HST*, which thus best represents the majority of the assembled stellar mass in our objects at useful resolution.

We adopted a fixed set-up for the GALFIT fitting procedure. We first ran SEXTRACTOR on the H_{160} mosaic to determine initial estimates for the centroid x, y pixel positions, total magnitude, axial ratio and effective radius of each object, where the total magnitude is given by MAG_AUTO and the effective radius is taken as FLUX_RADIUS with the fraction of total flux within this radius set as 50 per cent. SEXTRACTOR is also used to produce a segmentation map of the image.

In addition to the image and segmentation map, GALFIT also requires an input σ map in order to conduct the χ^2 fitting. To first order this σ map can be given by the rms map generated for the CANDELS mosaic, see Koekemoer et al. (2011). This rms map contains noise from the sky, read noise and dark current contributions from all the input exposures and is used as an initial input, but is adapted later in the procedure to include the Poisson noise contribution from the object itself, which proves to be a non-trivial contribution for the bright objects in our sample.

From the image, segmentation map and rms map we then generated 6×6 arcsec stamps for each object centred on the x, y pixel positions from SEXTRACTOR. These are the actual input files read into GALFIT and the code is allowed to use the full 6×6 arcsec area in the fit, with the exception of any pixels associated with companion objects in the image stamps (which are masked out by the bad pixel map).

The method outlined here provides us with a σ map, a bad-pixel mask and the best guess initial model parameters, which are read directly into GALFIT. This set-up procedure has been implemented in a GALFIT wrap-around script and is consistent for all following tests of the PSF and background determinations used.

4 SINGLE SÉRSIC MODELS

As mentioned above, the two key elements which can significantly affect the best-fitting model parameters derived by GALFIT are, first, the accuracy of the adopted PSF and, secondly, the method used to establish the sky background. We have investigated both these issues, and their impact on derived parameter values and errors. Full details of our findings are relegated to Appendixes A and B, but here we provide a summary of the most important conclusions of this work. For simplicity, the discussion of these issues is here restricted to the single-Sérsic models.

4.1 PSF dependence

The precision of the PSF used in the fitting procedure, especially within a radius of $\simeq$0.6 arcsec (corresponding to a physical scale of $\simeq$5 kpc at the redshifts of interest here), is crucial for the accurate determination of the scalelengths of the galaxies in our sample, as many of them transpire to have effective radii of comparable angular size. Previous morphological studies of massive galaxies at $z > 1$ have adopted both empirical and modelled PSFs in their fitting procedures, with modelled *HST* PSFs being generally determined using the TINYTIM code (Krist 1995). We have explored the impact of using both empirical and TINYTIM PSFs on the resulting morphological fits. Our empirical PSF was constructed from a median

stack of seven bright (but unsaturated) stars in the WFC3/IR H_{160} image of the CANDELS-UDS field, after centroiding each stellar image. A detailed comparison of our empirical PSF and the TINYTIM model is presented in Appendix A. In brief, we find that the TINYTIM model significantly underpredicts the emission from the real PSF around the crucial radius of $\simeq$0.6 arcsec. Consequently, we found that adoption of the TINYTIM PSF returns fitted galaxy sizes that are on average systematically 5–10 per cent larger than those determined using the empirical stacked PSF. As also described in Appendix A, we have confirmed that our empirical PSF does an excellent job of reproducing the profile of individual stars in the CANDELS H_{160} image, providing reassurance that it is has not been significantly broadened or otherwise damaged by the stacking process on the angular scales of interest. Accordingly, for all subsequent galaxy fits presented in this paper we have adopted our empirical PSF.

4.2 Background dependence

The *HST* mosaics provided in the CANDELS data release have already been background subtracted, and so initially we attempted to use GALFIT on image stamps extracted from the H_{160} mosaic without additional background corrections. However, upon inspection of the radial profile plots of the fits, it became clear that additional object-by-object background corrections were required. Moreover, the impact of background determination on the best-fitting values of, and degeneracies between, the fitted values of Sérsic index and effective radius is non-trivial (Guo et al. 2009), and merits careful exploration.

To properly explore this issue, we constructed a grid of GALFIT runs sampling the full parameter space of Sérsic index, effective radius and plausible background values (see Appendix B for full details on how this grid was constructed). Such an analysis is computationally expensive, but it has allowed us to explicitly examine the impact of uncertainties in the background on the GALFIT results. This problem is, of course, well known, and previous studies have attempted similar tests using different approaches (e.g. Häussler et al. 2007; van Dokkum et al. 2010). However, by marginalizing over the additional background subtraction value which gives the best χ^2 fit for each combination of Sérsic index and effective radius we are able to properly expose the impact of background determination by constructing the χ^2 surface in the Sérsic index/effective radius plane for each object.

In Fig. 1 we show the resulting $\Delta\chi^2$ contours in the n–R_e plane for three examples of galaxies in our sample. The upper panels show the contours which result from adopting a single fixed background for each source, in this case the median background from the 6 $\times$ 6 arcsec image stamp centred on the object in question (but excluding the central region of radius 1 arcsec, in addition to excluding pixels masked out via the segmentation map). The lower panels show the corresponding contours which result from fitting to the same three galaxies, but in addition marginalizing over a varying background (from our full background-grid search). As can be seen from these examples, allowing the background to vary during the

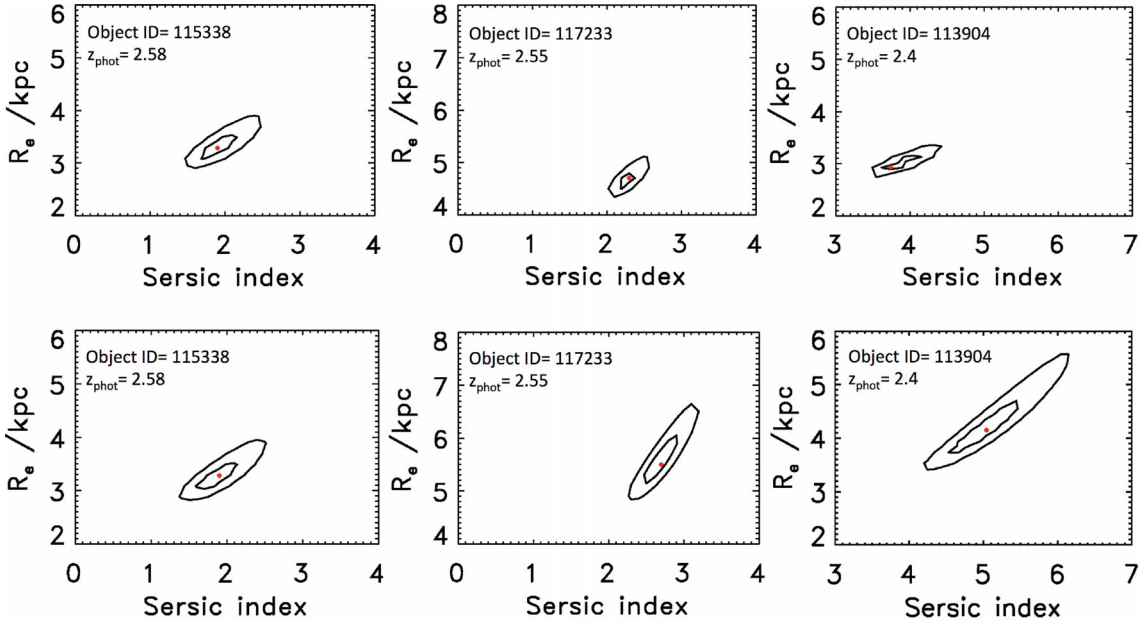

Figure 1. An illustration of the errors in, and degeneracies between, fitted effective radius R_e and Sérsic index n, also showing the effect of allowing the background to vary during the fitting process. Results are shown for three example objects, with contours plotted in the n–R_e plane at $\Delta\chi^2 = 4$ ($\equiv 2\sigma$ for 1 degree of freedom) and $\Delta\chi^2 = 9$ ($\equiv 3\sigma$ for 1 degree of freedom) above the the minimum χ^2 value achieved by the best-fitting model (marginalizing over all other fitted parameters). The location of the best-fitting model is indicated by the red dot in each case. The upper panels show the contours which result from adopting a single fixed background for each source, in this case the median background from the 6 $\times$ 6 arcsec image stamp centred on the object in question, but excluding the central region of radius 1 arcsec (in addition to excluding pixels masked out via the segmentation map). The lower panels show the corresponding contours which result from fitting to the same three galaxies, but in addition marginalizing over a varying background (from the full background-grid search described in the text). As can be seen from these examples, allowing the background to vary during the fitting process can significantly open up the contours for some galaxies, increasing the errors on the fitted parameters to arguably more realistic values. Moreover, from inspection of the third example (far right) it is clear that, for some of the largest objects in our sample, use of the 6 $\times$ 6 arcsec median background can clip the wings of the galaxy and lead to an underestimate of effective radius (note that the contours from the full background grid fitting do not in fact include the best-fitting solution achieved with the fixed median background, and vice versa).

fitting process can significantly open up the contours for some galaxies, increasing the errors on the fitted parameters to arguably more realistic values. Moreover, from inspection of the third example (far right) it is clear that, for some of the largest objects in our sample, use of the 6 × 6 arcsec median background can clip the wings of the galaxy and lead to an underestimate of effective radius (note that the contours from the full background-grid fitting do not in fact include the best-fitting solution achieved with the fixed median background, and vice versa). However, as discussed further below, it transpires that the number of such objects (i.e. objects whose scalelength is substantially boosted by the full background-grid search) within our sample is relatively small.

However, it should also be noted that, even with allowance for a variable background, there are a considerable number of objects within our sample for which the derived 1σ error bars for the Sérsic index and effective radius parameters fell below the size of the grid steps used in the full parameter search (0.025 in arcsec, 0.1 in Sérsic index). Such accuracy testifies to the power of the deep, high-resolution imaging provided by WFC3/IR for these (relatively) bright objects. However, it does mean that it is difficult to establish a robust error for the parameter values in these tightly constrained fits; to be conservative, for such objects we have simply adopted the smallest grid steps as the 1σ errors on R_e and n.

This analysis has thus enabled us to produce more realistic errors on the Sérsic index and effective radius parameters for all the objects in our sample than would be inferred from the errors provided directly by GALFIT. The error bars produced by GALFIT are purely statistical and are determined from the covariance matrix used in the fitting, and it is well known that this often results in unrealistically small uncertainties in the derived galaxy parameters. This issue is well documented in Häussler et al. (2007), where they used GEMS data (Rix et al. 2004) to test how well GALFIT can recover the input parameters of simulated $n = 1$ (disc) and $n = 4$ (bulge) galaxies. They found that GALFIT returns errors which are significantly smaller than the offset between the fitted and simulated input parameters, and so concluded that the dominant contribution to the real errors in the fitting procedure arises not from statistical shot noise or read noise (as is calculated by GALFIT), but from contamination of the fitting region by companion objects, underlying substructure in the sky, correlated pixels or potentially profile mismatching.

From our full background grid search we find that the distribution of errors is centred on $\simeq$5 per cent for Sérsic index and $\simeq$10 per cent for effective radius. This can be compared with the errors returned by GALFIT (which are often simply adopted in the literature) where we find that, for the deep, high-quality imaging used here, the error distributions are centred on $\simeq$2 per cent for Sérsic index and $\simeq$1 per cent for effective radius.

To complete our analysis of the impact of background determination on derived morphological parameters we have considered not only the best-fitting background from the grid and the original 6 × 6 median background, but also an alternative median background determination involving exclusion of all pixels within a larger central aperture (i.e. the median of those pixels lying within an annulus between 3 and 5 arcsec radius), and finally also zero background correction (i.e. just adopting the CANDELS mosaics as supplied, as we initially attempted). All four of these background values typically lie within the range searched within the background grid, but it is nevertheless instructive to consider these four specific alternatives because they represent choices frequently adopted in the literature.

Since our aim is to establish how robust our derived morphological parameters are to such choices, we used each of these four background estimates to establish a minimum and maximum scalelength that could plausibly be derived for each object. The resulting extremes are almost certainly pessimistically large representations of the uncertainty in scalelength, but nevertheless, as we show in Fig. 2, the impact on the typical sizes of the galaxies in our sample is still reassuringly small. Fig. 2 shows the two alternative versions of the size–mass relation for the galaxies in our sample which result from adopting the minimum (left-hand panel) or maximum (right-hand panel) scalelengths as explained above. Those objects where the maximum value of R_e is >15 per cent larger than the minimum value have been highlighted in red, but it is clear that such objects are in a small minority (<15 per cent), and the overall impact on the size–mass distribution exhibited by the sample as a whole can be seen to be small. The implications of the size–mass distribution displayed by our galaxy sample are discussed later (Section 6).

In Fig. 3 we provide an additional representation of the robustness of our scalelength measurements, and also show that the determination of Sérsic index is extremely reliable, little affected by the alternative background determinations, except for the very small number of objects with unusually large values of n.

In conclusion, therefore, our full background-grid search has enabled us to place realistic errors on the values of the derived parameter values such as R_e and n, but has also shown that, *for the quality of data utilized here*, our results for the sample as a whole are reassuringly robust to sensible alternative choices of the background level for each object.

We stress the point that the problems of systematic bias we have explored here could be much more serious for alternative data sets, especially for ground-based observations with broader PSFs and higher backgrounds (or alternatively when pushing *HST* data closer to the detection limit).

Given the results presented in Figs 2 and 3, we did not invoke the full background search again for the multiple-component modelling described in the next section. For those objects which yielded robust values of R_e in the single-Sérsic fitting described in this section, we have continued to simply adopt the 6 × 6 arcsec (excluding the central aperture of 1 arcsec radius) median background determination. For the subset of $\simeq$15 per cent of objects whose sizes varied by more than 15 per cent (i.e. those marked in red in Fig. 2) we found that the median background as determined in the 3–5 arcsec annulus returned a size centred close to the middle of the derived range in R_e, and so adopted this larger annular median as the appropriate background level for this subset of (generally larger) objects hereafter.

5 MULTIPLE-COMPONENT MODELS

Encouraged by the robustness of the single-component Sérsic fits, we decided to attempt to decompose the H_{160} images of all the galaxies in our sample into separate bulge ($n = 4$) and disc ($n = 1$) subcomponents. For each object we adopted the median background measurements as described above, and locked all subcomponents at the galaxy centroid as determined from the single-Sérsic fits.

To determine whether multiple components were actually merited to describe the data, we first fitted three models to each galaxy, namely (i) a bulge-only model with $n = 4$ (i.e. a de Vaucouleurs spheroid), (ii) an exponential disc-only model with $n = 1$ and (iii) a double-component bulge+disc model, with again the Sérsic indices locked to $n = 4$ and $n = 1$, but the relative amplitudes of the components, their scalelengths, axial ratios and position angles all allowed to vary independently.

Here we limit our analysis to fixing the Sérsic index of both components as opposed to allowing the spheroid

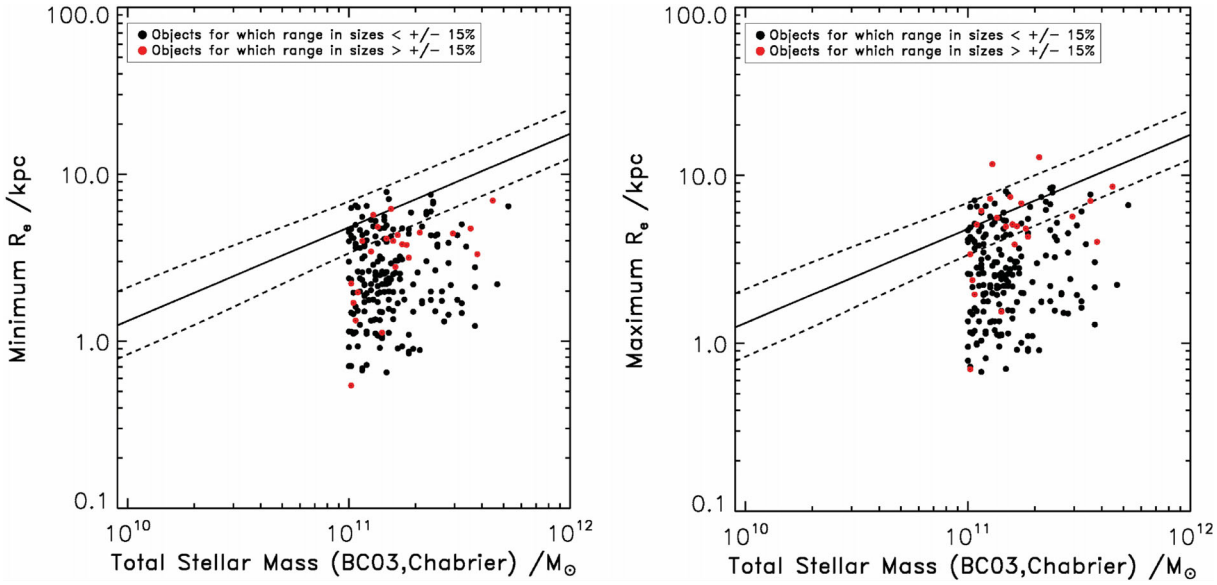

Figure 2. The size–stellar mass (R_e–M_*, using semimajor axis R_e values) relation displayed by our $M_* > 10^{11}$ M$_\odot$, $1 < z < 3$ galaxy sample utilizing the minimum (left-hand panel) and maximum (right-hand panel) derived values of scalelength, R_e, as determined utilizing the full range of background estimators as described in the text of Section 4.2. The objects marked in red ($\simeq$15 per cent of the sample) are those for which the maximum value of R_e is >15 per cent larger than the minimum, although it should be noted that the adopted range of plausible values of R_e has here been chosen to be unrealistically pessimistic. Also plotted (solid line) is the local relation for early-type galaxies from Shen et al (2003), with its 1σ scatter indicated by the dashed lines. Despite our efforts to here exaggerate the uncertainty in R_e, it is clear that the size–mass relation for this sample as a whole, as derived from the high-quality CANDELS WFC3/IR imaging, is remarkably robust.

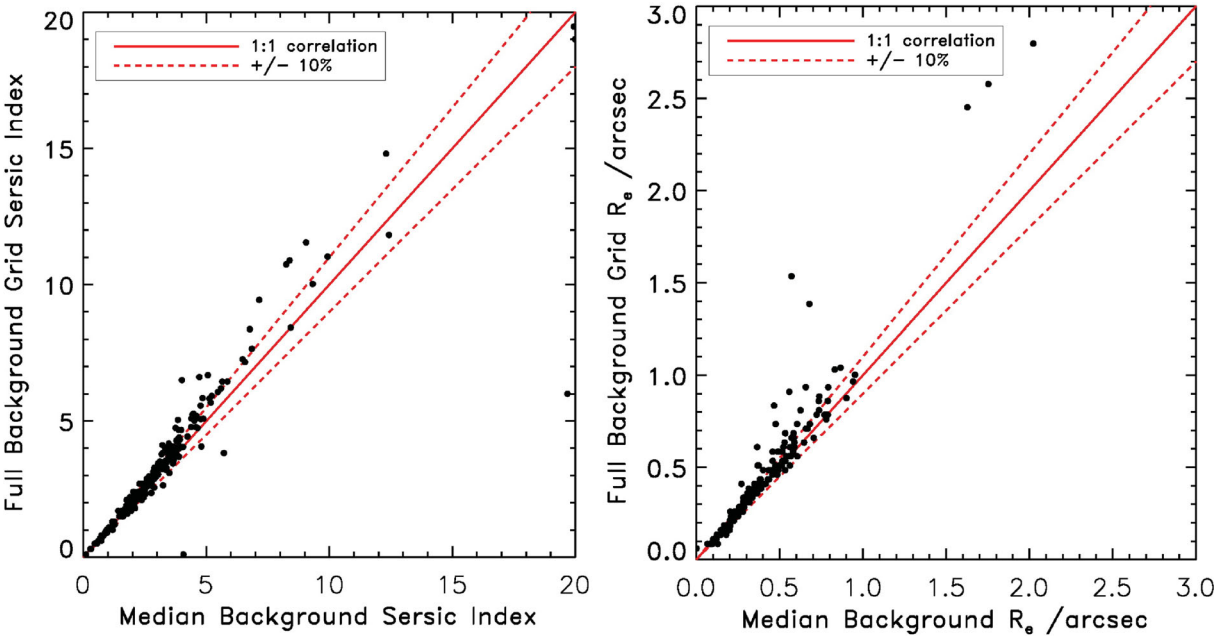

Figure 3. A comparison of the Sérsic indices and effective radii R_e of the galaxies in our sample as derived using the background determined from the median value within a 6 × 6 arcsec square image stamp (excluding pixels within 1 arcsec of the object centroid), and as obtained allowing the background level to float as part of the fitting process. For $\simeq$90 per cent of the objects in the sample the results are in excellent agreement; the full background-grid search yields significantly larger values of Sérsic index and R_e for $\simeq$5 per cent of the galaxies in our sample.

component to have a variable index value during the fitting (as has been adopted for some lower redshift studies). Decomposition of the CANDELS data at these redshifts is already a challenge, and the addition of the spheroid Sérsic index as a free parameter will cause significant degeneracies in our fits.

It might seem that the first two of these models are simply a subset of the third (i.e. the bulge+disc model). However, our aim was to see if the second component was actually required (i.e. whether the more sophisticated model was statistically justified). In addition, inspection of the results from the double-component fits revealed that whenever the fainter component contributed less than

$\simeq$10 per cent of the H_{160}-band light, the parameter values for the fainter component were often unphysical and could not be trusted for scientific interpretation (e.g. left to its own devices, GALFIT will still often choose a secondary component with, for example, a completely unphysical scalelength in order to fix some unevenness in the background, even when such a component is not really required to achieve a formally acceptable fit). Thus, as explained further below, whenever a secondary component contributed less than 10 per cent of the flux, we simply reverted to the appropriate single-component model, designating the object as disc-only or bulge-only as appropriate.

Finally, we also explored the effect of introducing a further additional component in the form of a point source at the galaxy centre. This was to allow for the possibility of an AGN or central star cluster, both to quantify the evidence for such components, and to check whether any point sources were distorting the galaxy fits. We explored adding an additional point-source contribution to the single variable Sérsic, bulge-only, disc-only and disc+bulge models. Consequently, in total we eventually fitted eight alternative models to each galaxy.

The exact fitting procedures implemented are detailed in the following subsections, while the process by which we decided which model to adopt for a given galaxy is described in Section 6.

5.1 Bulge-only and disc-only models

The bulge-only and disc-only models are the simplest we attempted to fit to each galaxy. We constructed a GALFIT parameter file for each object using the best-fitting single-Sérsic parameter values as a starting point, locking the centroid position, and locking the Sérsic parameter at $n = 4$ or $n = 1$. Thus GALFIT was free to vary only the total magnitude, the effective radius, the axial ratio and the position angle of the forced disc or de Vaucouleurs bulge model. As with all the model fitting, great care was taken (via image masking) to exclude pixels which contained any significant flux from companion objects, so as not to distort the best-fitting value of χ^2.

5.2 Double-component bulge+disc models

For the bulge+disc models we again locked the centroid (of both components) at the x, y position returned from the single-Sérsic fitting, and locked the Sérsic indices of the two components to $n = 4$ and $n = 1$. The other parameters of both components were allowed to vary independently (i.e. allowing the bulge and disc to have very different fluxes, sizes, axial ratios and position angles if required).

When using GALFIT for this simultaneous double-component fitting, with the consequent increase in the number of degrees of freedom, we were aware of the increased danger of the fit becoming trapped in a local χ^2 minimum during the minimization routine. To tackle this issue, and ensure that our double-component fits do indeed reflect the global minimum in χ^2, we constructed a grid of different starting values for the total magnitudes and effective radii of the two components, and repeatedly restarted GALFIT from different positions on this grid. The grids were constructed with 11 steps in starting magnitudes for the two components, for each of which there were then 21 steps in initial effective radii. The grid initial magnitudes were set at 99 per cent of the SEXTRACTOR MAG_AUTO for each object in the bulge (and hence 1 per cent in the disc), then 90 per cent bulge and 10 per cent disc, 80 per cent bulge and 20 per cent disc, continuing similarly to 10 per cent bulge and 90 per cent disc and finally 1 per cent bulge and 99 per cent disc. Meanwhile the grid of effective radius values steps from 99 per cent of twice the SEXTRACTOR r_{50} value for each object in the bulge and 1 per cent in the disc, to 95 per cent bulge and 5 per cent disc, 90 per cent bulge and 10 per cent disc, and again continuing similarly to 5 per cent bulge and 95 per cent disc and finally 1 per cent bulge and 99 per cent disc. We restarted GALFIT from each of these 231 alternative starting points in order to ensure we found the global minimum in χ^2, and then adopted the corresponding parameter values as our best-fitting double-component model. After this extensive additional fitting, we found that the models fitted for the individual components are actually relatively robust to the initial starting conditions to an accuracy of $\simeq$20 per cent in the fitted effective radii and magnitudes.

5.3 Introduction of an additional point source

When conducting the single-Sérsic model fits (as described in Section 4) we allowed the Sérsic index, which is a measure of the central concentration of the light profile, to range across the full 0–20 parameter space allowed by GALFIT, as opposed to capping it at more physical values limited to $n < 8$. This allowed us to fully explore how n and R_e are traded off against each other by GALFIT when attempting to deliver model fits to some of the more unusual objects in the sample.

We found that 28 out of our full sample of 215 objects yielded Sérsic indices in the range $5 < n < 20$. Upon inspection it appeared that these objects did indeed often have strongly peaked central components. We therefore introduced the option of an additional point source to the single-Sérsic fits, allowing GALFIT to vary the relative amplitude of the point source and the single-Sérsic component.

This additional option of a point source yielded significantly improved fits for 10 of these 28 objects, at the same time also yielding new, arguably more realistic, values of $n < 5$. Of the remaining 18 'high-Sérsic objects', 13 had $5 < n < 8$, and remained essentially unchanged (rejecting the additional option of a point source) while the remaining five yielded only slightly reduced values of n, and thus remained outside of the generally accepted Sérsic index range.

Finally, in order to maintain a fully consistent approach across our entire sample, we decided to revisit the single-Sérsic, disc-only, bulge-only and disc+bulge models of every object to allow the option of an additional point source in every case. This was done by again locking the centroid of all components at the single-Sérsic centroid, and initially setting the brightness of the point source at 1 per cent of the SEXTRACTOR MAG_AUTO value. For the bulge+disc+point-source models we again generated a grid of initial starting parameters as detailed in Section 5.2.

Out of the complete sample of 215 objects, 59 preferred to accept the contribution of a point source comprising >10 per cent of the overall light of the galaxy (as before, we deemed unreliable/insignificant any contribution of <10 per cent by any individual model subcomponent). In no case did the contribution of the point source ever exceed 43 per cent of the total brightness of the object, indicating that none of our objects is 'stellar' or AGN dominated. Out of curiosity we checked whether those fits which preferred to accept a significant contribution from a point source showed any enhanced probability of yielding a 24 μm detection in the SpUDS *Spitzer* MIPS imaging, but we did not find any significant correlation. However, we note that a point-source contribution might arise from a central starburst rather than an AGN. We also note that a preference for a point-source contribution does not necessarily mean that it is statistically required, an issue which we discuss

further below in the general context of choosing between the array of alternative models we ultimately generated for each object.

6 FINAL GALAXY MODELS

With the inclusion of the point-source option in all models, we were left with eight alternative model fits, of varying complexity, for every object in the sample. In deciding which 'best-fitting' model to adopt for each source for future science analysis,we chose to split the models into two categories within which the models are formally nested, and thus χ^2 statistics can be used to determine the 'best' model given the appropriate number of model parameters. The first category consists of the single-Sérsic models and the single-Sérsic plus point-source models. The second category comprises the bulge-only and disc-only models, the bulge+point-source and disc+point-source models, the bulge+disc models and the bulge+disc+point-source models. Comparison between these two categories is more problematic, except in those cases where no satisfactory fit was achieved with a category 1 model, while a satisfactory fit was achieved with a category 2 model. As other researchers in the field may be interested in both the variable-Sérsic and bulge+disc fits, we have retained and present the parameter values for the best-fitting models from both categories in the tables given in Appendix D.

6.1 Selection of the best model

For each object we recorded the best-fitting parameters from each of the eight (two single-Sérsic and six multiple component) models fitted to the data. However, before undertaking a statistical comparison of the alternative model options, we applied a series of criteria to reject unreasonable or physically unrealistic models.

The first criterion imposed is the one already mentioned above, namely that we decided to throw away any model in which any subcomponent contributed <10 per cent of the total H_{160}-band light. Accordingly, any model with a very weak point source was rejected as unnecessary, as was any model with a very weak bulge or disc component. As discussed above, this decision was made after intensive inspection of the alternative model results revealed that such low-level components were often, in effect, artefacts of an unjustifiably complex fit (and even when physically plausible, their derived parameter values were too uncertain to be trusted in further analysis).

The second criterion again directly addresses how meaningful the fitted parameters are, as we decided to exclude any model with a subcomponent whose effective radius exceeded 50 pixel (i.e. 3 arcsec), the fitting radius of our image stamps. This criterion did not in fact lead to the rejection of many models, but those that were rejected on this basis had clearly unphysical effective radii (i.e. they substantially exceeded the 3 arcsec angular diameter threshold).

The third criterion, again aimed at confining our best-fitting models to those which are physically realistic, involved the rejection of any model which contained a bulge component with an extreme axial ratio $b/a < 0.1$. This additionally served to exclude any bulge models where the fitted effective radii were less than 1 pixel in size.

Having applied these criteria, it remained to consider, for each object, the relative merits of the surviving model alternatives within each category. First, we rejected any of the remaining models which did not deliver formally acceptable fits at the 3σ level, as judged from the absolute value of χ^2 achieved, and the number of degrees of freedom, ν (where the number of degrees of freedom means the number of data points minus the number of fitted parameters minus 1, and is typically 7000–10 000 for the images and models fitted here, the precise value for each object depending on the degree of image masking; see Appendix C).

A model fit was thus deemed formally acceptable if the minimum value of χ^2 is satisfied:

$$\chi^2 \leq \nu + 3\sqrt{(2\nu)} \tag{2}$$

and if any model failed this test it was no longer considered (although see below for model refinement).

Finally, if more than one model within each category survived all of the above tests, we chose between the acceptable fits of varying complexity by adopting the simplest acceptable model, unless a model of higher complexity satisfied

$$\chi^2_{\rm complex} < \chi^2_{\rm simple} - \Delta\chi^2(\nu_{\rm complex} - \nu_{\rm simple}), \tag{3}$$

where now ν represents the number of degrees of freedom in the model (in effect the number of parameters), and $\Delta\chi^2(\nu_{\rm complex} - \nu_{\rm simple})$ is the 3σ value for the given difference in the degrees of freedom between the two competing fits.

In this way we narrowed down the alternative models to a single, final, best-fitting model within each category, and the best-fitting parameters for these (two) models of each object are given in Table D2 in Appendix D.

In the relatively small number of cases where no formally acceptable model survived the first of the χ^2 tests described above, we have still applied the final *relative* quality-of-fit test, so as to retain parameter values for every galaxy in case this is required (note that very few other studies in this area have actually been concerned with assessing whether the best-fitting models are genuinely formally acceptable, even though a failure to achieve this renders the assessment of errors in parameter values problematic). The parameter values from these best-fitting, albeit formally unacceptable models are also presented in Table D2 for completeness, but are flagged by an asterisk in the bulge effective radius column. These unacceptable fits, and our efforts to minimize the number of such cases, are discussed further in the next subsection and in Appendix C.

6.2 Model fit refinement

As a final comment on the technical aspects of the model-fitting described in this paper, we briefly consider the problems we encountered in achieving formally acceptable fits to a subset of our objects, and the steps we took to minimize the number of objects for which the modelling still proved formally inadequate. A fuller description of this work is provided in Appendix C for the interested reader.

Upon completion of our initial model fitting, we found that 70 out of our full sample of 215 objects had no formally acceptable model fits as judged by the first of the two χ^2 tests described above (i.e. equation 2). To establish the cause of the excessively high values of χ^2, we visually inspected the images of all 70 objects. We found that there were several obvious, but different, reasons for these high χ^2 values, with the problematic objects including (i) $z < 2$ spiral galaxies with very prominent spiral arms, (ii) interacting/asymmetric systems, (iii) objects in very crowded fields and (iv) objects with extremely close companions which had not been separately identified by SEXTRACTOR.

We therefore included an additional round of modelling for these objects, refitting after masking out the problematic non-axisymmetric structures (such as spiral arms or close companions) on the basis of χ^2 maps produced from the original attempted fits.

Table 1. Percentages of the final sample of 192 objects with multiple-component best fits corresponding to each of the six fitted models.

bulge (per cent)	bulge +psf (per cent)	disc (per cent)	disc +psf (per cent)	bulge +disc (per cent)	bulge+disc +psf (per cent)
10 ± 2	1 ± 1	18 ± 3	8 ± 2	58 ± 7	5 ± 2

Using this approach we re-ran all the model fits as described in Section 5, and re-selected the best-fitting models. Doing this delivered acceptable fits for all but 14 objects in our entire catalogue. The quality of the final fits achieved in this work is demonstrated by the final distribution of minimum χ^2 for the full sample, which is shown in Fig. C4 and discussed further in Appendix C.

Finally, it is important to stress that, while this re-fitting was sometimes required to achieve formally acceptable values of χ^2 (and hence set meaningful errors on the best-fitting parameters), it in fact very rarely resulted in any significant change in the best-fitting *values* of these parameters. This is shown explicitly by the comparisons of the best-fitting parameter values (as achieved before and after this additional round of image masking) shown in Appendix C. The reason for this is simply that while high surface brightness features which cannot be represented via axisymmetric modelling can contribute significantly to χ^2, they rarely actually dominate a sufficiently large fraction of our object image stamps (which each contain $\simeq$10 000 pixel) to significantly distort the morphological properties of the underlying mass-dominant galaxy as established via our modelling.

For all multiple-component science results presented we use a final sample of 192 objects, where from our original sample of 215 objects we have removed the 14 objects which still had formally unacceptable multiple-component model χ^2 values even after the χ^2 masking described in the text, as well as seven objects which have unrealistically large single-Sérsic indices ($n > 10$), and two unresolved objects which may be stars. For completeness the percentages of the final sample of 192 objects with multiple-component best fits corresponding to each of the six fitted models is given in Table 1.

7 SCIENCE RESULTS

Having determined both accurate and acceptable single-Sérsic models and bulge+disc decompositions for the vast majority of the objects within our sample, we are now able to proceed to explore the scientific implications of our results. First, however, it is interesting to consider the correlation between single-Sérsic index and *B*/*T* flux ratio delivered by our modelling of these massive galaxies at $1 < z < 3$, a relation which has been extensively studied and debated at lower redshifts (e.g. Ravindranath et al. 2006; Cameron et al. 2009; Simard et al. 2011; Lackner & Gunn 2012). This is plotted in Fig. 4, where it can be seen that, in contrast to some previous studies at lower redshift ($z < 1$), we find that Sérsic index and *B*/*T* flux ratio are generally in remarkably good agreement; from Fig. 4 it can be seen that disc-dominated systems with $B/T < 0.5$ are almost completely confined to the Sérsic index range $0 < n < 2$, and that virtually all bulge-dominated galaxies with $B/T > 0.5$ have $n > 2$. These results provide further confidence in the reliability of our morphological analysis, and suggest that our attempt to separate the galaxies into bulge and disc components is meaningful and, moreover, justified by the quality of the WFC3/IR data.

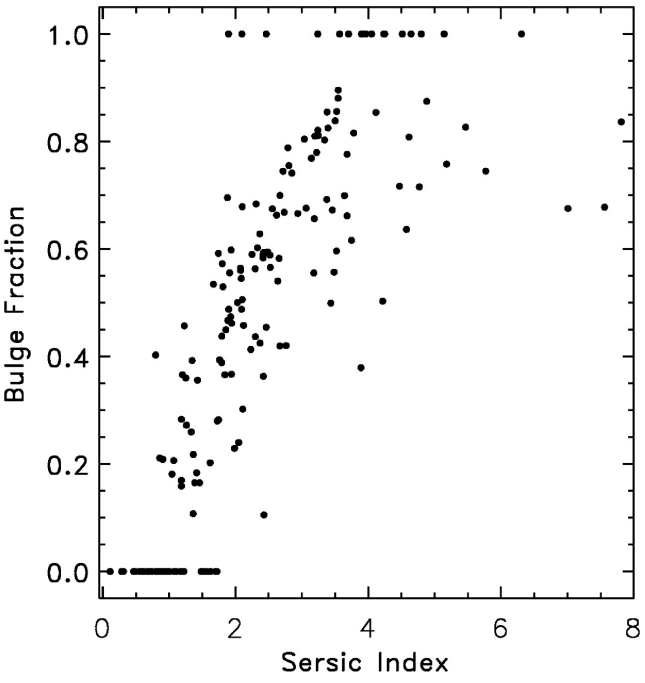

Figure 4. Sérsic index from the single-Sérsic fits, versus bulge to total (*B*/*T*) fractional contribution to the H_{160}-band light (as determined from the multicomponent modelling) for the final sample of 192 objects used in all subsequent double-component science plots and analysis. We have removed the 14 objects which still had formally unacceptable χ^2 values even after the χ^2 masking described in the text, as well as seven objects which have unrealistically large single-Sérsic indices ($n > 10$), and two unresolved objects which may be stars. It can be seen that there is a good correlation between the two estimators of bulge dominance, with $n \simeq 2$ corresponding to roughly equal bulge and disc contributions. Note that the objects at the top and bottom of the plot are located at $B/T = 1.0$ or 0.0 due to our insistence (based on intensive inspection of the modelling results) that any subcomponent contributing less that 10 per cent of total flux is discarded as insignificant and unreliable. This of course also leads to two artificial gaps in the distribution of bulge fraction. Reassuringly, the group of objects with *B*/*T* rounded down to zero is centred on $n = 1$, while the 'pure-bulge' objects with *B*/*T* equal to unity is centred on $n = 4$.

7.1 The size–mass relation

We now use our modelling results to explore the size–mass (R_e–M_*) relation for massive galaxies in the redshift range $1 < z < 3$, considering first the results from the single-Sérsic fits, and then the output from our bulge+disc decompositions.

The best-fitting results from our single-Sérsic analysis detailed in Section 4 are shown in Fig. 5, overplotted with the local relation from Shen et al. (2003). The galaxy sizes determined by Shen et al. were determined by fitting 1D surface brightness profiles within circular apertures, therefore we have converted their results to reflect estimated semimajor axis sizes by dividing the circularized Shen et al. sizes by the square root of the median axial ratio (*b*/*a*) for the $1 \times 10^{11} < M_* < 1 \times 10^{12}\,M_\odot$ SDSS sample. This median axial ratio value was taken to be 0.75, following the results from Holden et al. (2012). Alongside our single-Sérsic analysis in Fig. 5 is a compilation of results from some of the previous literature at $1 < z < 3$. Unsurprisingly, previous studies have adopted a variety of different techniques for stellar mass determinations and morphological modelling. However, the results plotted in the left-hand panel of Fig. 5 have been adapted to provide the fairest comparison with our results by ensuring that all stellar mass estimates have

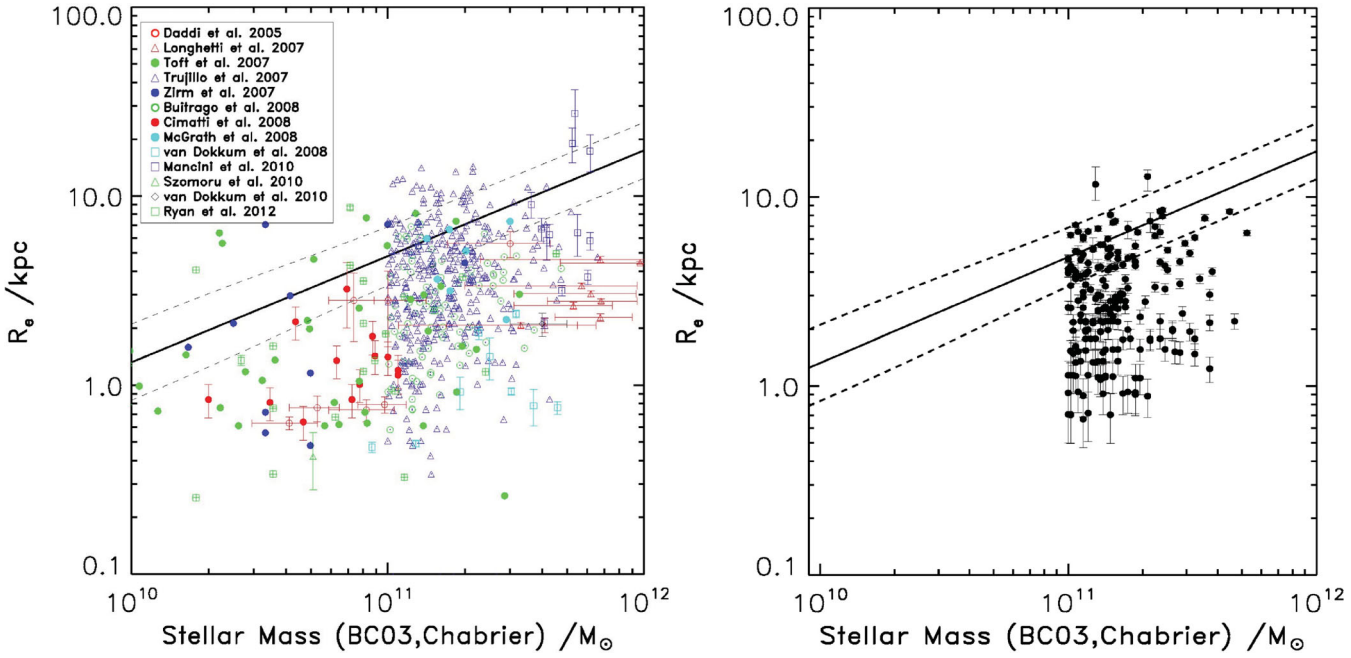

Figure 5. Various determinations of galaxy size versus stellar mass at $1 < z < 3$ from the literature are shown in the left-hand panel, for comparison with our new results for $M_* > 10^{11}\,\mathrm{M}_\odot$ galaxies over the same redshift range as shown in the right-hand panel. In order to facilitate comparison of the semimajor axis scalelengths determined here with an appropriate low-redshift baseline we have plotted a solid line on both panels to indicate the local early-type galaxy relation from Shen et al. (2003) (with the scatter in this relation indicated by the dashed lines). Because the galaxy sizes determined by Shen et al. were determined by fitting 1D surface brightness profiles within circular apertures, we have converted their results to reflect estimated semimajor axis sizes by dividing the circularized Shen et al. sizes by the square root of the median axial ratio (b/a) for the $1 \times 10^{11} < M_* < 1 \times 10^{12}\,\mathrm{M}_\odot$ SDSS sample. This median axial ratio value was taken to be 0.75, following the results from Holden et al. (2012). The results from the literature shown in the left-hand panel have all been converted to the masses that would have been derived using the Bruzual & Charlot (2003) models with a Chabrier IMF (see text for details). Unfortunately the scalelengths plotted in the left-hand panel contain a mix of both circularized and semimajor axis values, but since they come mainly from studies of early-type galaxies the correction from circularized back to semimajor axis values is generally small. Our own points shown in the right-hand panel are all based on Chabrier BC03 masses, and semimajor axis effective radii derived from our single-Sérsic modelling of the H_{160} images. This figure serves to demonstrate the extent to which our study has advanced knowledge of the size–mass relation for galaxies in this crucial redshift range in this high-mass regime. It can be seen that, while the majority of the objects in our sample lie below the local relation, a significant subset (32 ± 4 per cent) are consistent with it within the plotted 1σ errors.

been converted to those that would have been determined using a Chabrier IMF with a Bruzual & Charlot (2003) stellar population synthesis model. Nevertheless, the comparison remains imperfect both because the literature results are taken from imaging at a range of different rest-frame wavelengths, and because they comprise a mixture of both circularized and semimajor axis effective radii (although, as the literature results come predominantly from studies of early-type galaxies, the correction from circularized to semimajor axis values is generally small). An additional complication arises from the fact that the studies in the literature have utilized a variety of different selection criteria, with most previous studies deliberately biased towards passive and/or early-type galaxies. In contrast our own sample is based on a relatively straightforward mass limit; while this inevitably limits the dynamic range of our study, it can be seen from Fig. 5 that this work represents a significant contribution towards populating the high-mass regime of the size–mass plane at these redshifts.

Armed with our modelling results for this first substantial, complete, high-mass-limited sample, we find that the majority (68 ± 7 per cent) of these galaxies have effective radii which place them well below the local relation and its 1σ scatter (where in this high-mass regime the local early and late-type relations are essentially the same). However, there is also a significant subset of 32 ± 4 per cent of our objects which, within the error bars, are consistent with the sizes of similarly massive local galaxies. Within the limited redshift range spanned by our study, we see no dramatic trend in these statistics with redshift; splitting the sample at $z = 2$, in the redshift range $1 < z < 2$ we find 70 ± 10 per cent of objects lie below the local relation, with 30 ± 5 per cent essentially on it, while at $2 < z < 3$ the corresponding figures are 62 ± 11 and 38 ± 8 per cent, respectively.

One consequence of the majority of the galaxies lying significantly below the local relation is that the median size of these most massive galaxies at $1 < z < 3$ is a factor of 2.3 ± 0.1 times smaller (2.6 ± 0.2 kpc) than comparably massive local galaxies. Again we see no really significant redshift trend in this global statistic within our limited redshift range, although there is a gradual trend to smaller sizes with increasing redshift; splitting our sample below and above $z = 2$, the median size becomes 2.7 ± 0.3 and 2.5 ± 0.3 kpc, respectively, corresponding to 2.2 ± 0.2 and 2.3 ± 0.2 times smaller than the local relation.

Since Fig. 5 includes all objects, of whatever morphology, we next use the results from our bulge+disc modelling to check for any significant trends with morphological type, or indeed for trends with redshift within a given morphological subclass. Since we have attempted bulge+disc decomposition for all galaxies in the sample, we can plot the relevant size–mass relations not just for pure bulge or disc galaxies, or bulge- or disc-dominated galaxies, but for *all* bulges and discs (i.e. including the bulges from the disc-dominated objects and vice versa).

The size–mass relations for the separate bulge and disc components from the best-fitting multiple-component model are plotted in Fig. 6, shown both for the full redshift range, and subdivided for $z < 2$ and $z > 2$. Because we are plotting subcomponents, these plots contain some objects with stellar masses M_* substantially smaller than our original mass limit. This provides additional dynamic range, but we note that the stellar mass subdivision has been performed here solely on the basis of the fractional contribution of each subcomponent to the H_{160}-band light. This is clearly not quite correct, but a full SED-based mass determination for each subcomponent is deferred to a future paper involving fitting of the bulge+disc models to multiband optical–infrared imaging. It also does not mean that our study is in any sense mass-complete at masses substantially smaller than $M_* \simeq 10^{11}\,\mathrm{M}_\odot$. Nonetheless, it is instructive to see whether the minor components (e.g. the bulges in disc-dominated galaxies) follow the same trends as the dominant components (although to avoid pushing the data too far, we do not plot any subcomponents with estimated masses $M_* < 2 \times 10^{10}\,\mathrm{M}_\odot$). In Fig. 6 we also overplot the local early and late-type size–mass relations as described in the figure caption.

These plots reveal a number of interesting features. First, consistent with previous studies, it can be seen that the size evolution is more dramatic in the bulges than in the discs, but nevertheless most discs are also smaller than in the local Universe; over the full redshift range 81 ± 10 per cent of the bulges lie significantly below their relevant local relation, while for the discs the corresponding figure is 58 ± 7 per cent (conversely this means that only 19 ± 4 per cent of bulges are consistent with the local relation, but this figure rises to 42 ± 6 per cent for the discs).

An interesting aspect of the more dramatic size evolution displayed by the bulges is that their size–mass distribution, especially at the highest redshifts, appears bi-modal (although the statistics are weak), with the dominant population of compact bulges becoming increasingly separated from the minority of objects which appear still consistent with the local relation (see the top-right panel of Fig. 6). Interestingly these trends also seem to apply to the lower mass bulges embedded in the disc-dominated galaxies, which display the smaller sizes as 'expected' from a simple offset of the size–mass relation as determined from the more-massive bulge-dominated galaxies. [We note that it is at least plausible that

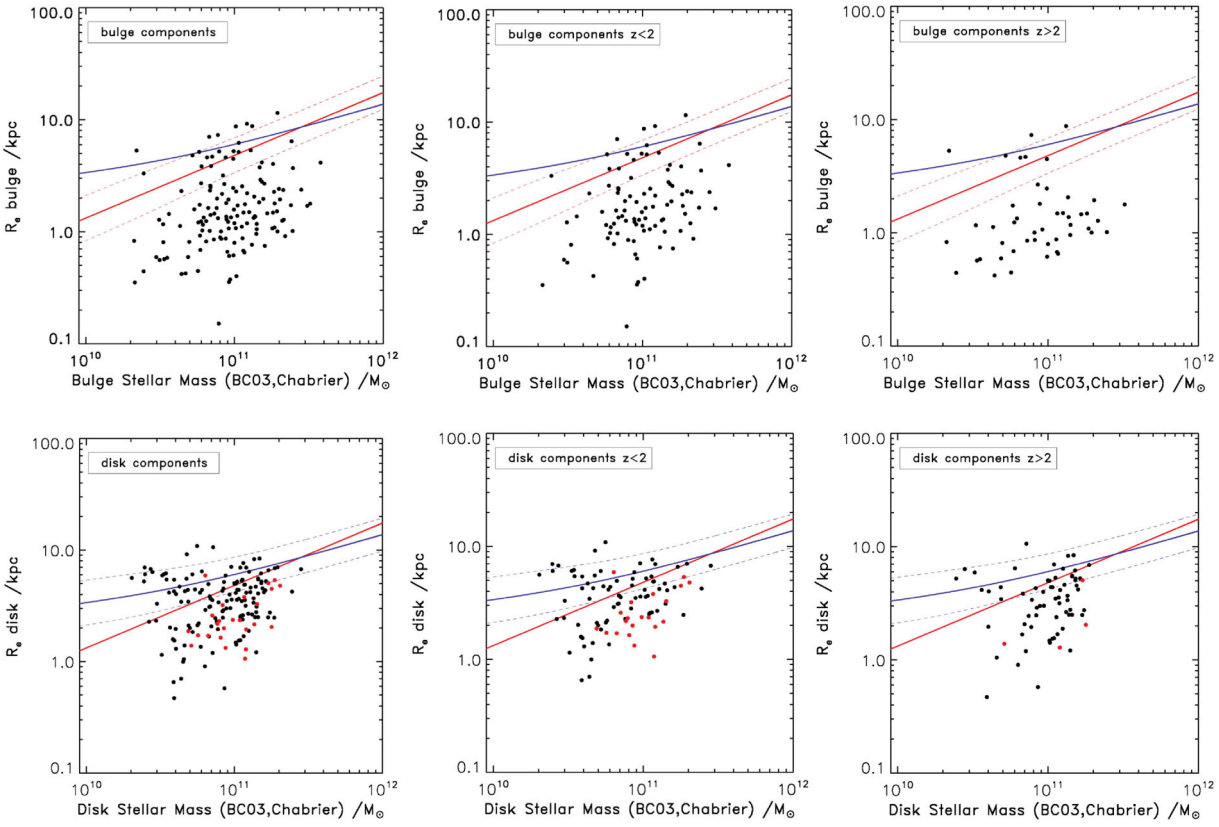

Figure 6. The size–mass relations displayed by the separate bulge components (upper row) and disc components (lower row) as produced from our bulge+disc modelling analysis of our massive galaxy sample (shown both for $1 < z < 3$ and then subdivided into two redshift bins). The masses plotted here for the individual subcomponents simply reflect the total mass of the 'parent' galaxy subdivided in proportion to the contribution of each component to the H_{160}-band light. For consistency, and to avoid overinterpreting the location of the weakest subcomponents, we have excluded nine objects whose component masses fall below $2 \times 10^{10}\,\mathrm{M}_\odot$. In the lower row of plots, the disc components from the passive disc-dominated galaxies discussed in Section 6.3 (i.e. objects with sSFR $< 10^{-10}\,\mathrm{yr}^{-1}$, no 24 μm counterparts and $B/T < 0/.5$) are overplotted in red. In order to provide a comparison with the sizes of comparably massive low-redshift bulge and disc counterparts, we have taken the local early-type and late-type galaxy relations from Shen et al. (2003) and converted them to non-circularized sizes [as described in the caption to Fig. 5, where the median axial ratio values were taken to be 0.75 for bulges (Holden et al. 2012) and 0.62 for discs (Padilla & Strauss 2008)]. These non-circularized relations are plotted as a solid red line for the local early-type relation, and a solid blue line for the local late-type galaxy relation; the dashed lines indicate the typical 1σ scatter in these relations. As discussed in detail in the text, these plots reveal the more dramatic size evolution displayed by the bulges which, by $z > 2$ are on average a factor of >4 smaller than their local counterparts. Nevertheless some bulges, and a rather large fraction of discs are still found to lie on the local relation throughout the redshift range.

some low-mass bulges at these redshifts become the cores of local discs (Graham 2011).]

The trends with redshift shown in Fig. 6 can be quantified in terms of the fractions of bulges and discs on or significantly below their respective local relations at $1 < z < 2$ and $2 < z < 3$. For the bulges the relevant figures are 20 ± 5 per cent on and 80 ± 12 per cent below in the lower redshift bin, and 15 ± 9 per cent on and 85 ± 18 per cent below in the upper redshift bin. For the discs there really is no evidence for any evolution in the relevant fractions within our redshift range; the percentages are 41 ± 8 per cent of disc components on and 59 ± 10 per cent of disc components below the local relation at $1 < z < 2$, and 43 ± 9 per cent on and 57 ± 11 per cent below at $2 < z < 3$.

These trends are also reflected in the evolution of the median sizes of the bulge and disc components. Even within our limited redshift range the (apparent) evolution in size of the bulges is fairly dramatic, where taking the median sizes of bulges which lie below the local early-type relation gives an offset from the local early-type relation already a factor of 3.5 ± 0.5 at $1 < z < 2$ rising to a factor of 4.4 ± 0.3 at $2 < z < 3$. In contrast, the offset for the discs from the local late-type relation is more modest and apparently unchanging, a factor of 2.4 ± 0.4 at $1 < z < 2$, and 2.5 ± 0.2 at $2 < z < 3$.

Finally, marked in red on the lower panels of Fig. 6 are the locations of the 'passive' discs in our sample, a population discussed further in Section 7.3. Interestingly, the vast majority of the passive discs lie below the local late-type size–mass relation.

7.2 Evolution of morphological fractions

We next consider how the relative number density of galaxies of different morphological type changes over the redshift range probed by our sample. In Fig. 7 we illustrate this by binning our sample into four redshift bins of width $\Delta z = 0.5$, and consider three alternative cuts in morphological classification as measured by B/T from our disc-bulge decompositions. We present the data in this way both to try to provide a complete picture, and to facilitate comparison with different categorizations in the literature. In the left-hand panel of Fig. 7 we have simply split the sample into two categories: bulge-dominated ($B/T > 0.5$) and disc-dominated ($B/T < 0.5$). In the central panel we have separated the sample into three categories, with any object for which $0.3 < B/T < 0.7$ classed as 'Intermediate'. Finally, in the right-hand panel we have expanded this Intermediate category to encompass all objects for which $0.1 < B/T < 0.9$.

From the first panel it can be seen that discs dominate at $z > 2$ and that this situation is reversed at $z < 2$. However, the other two panels help to emphasize that, at $z < 2$, pure bulges and discs are rare, and that the vast majority of lower redshift objects are, to a varying degree, disc+bulge systems. Interestingly, however, it is clear that, however the cuts are made, at $z > 2$ the population is disc-dominated, and a substantial fraction of the sample are 'pure' discs, which have largely disappeared by $z < 2$. Since the number density of galaxies in this high-mass regime falls dramatically with increasing redshift at $z > 3$, these plots illustrate that the redshift range $2 < z < 3$ is the *era of massive discs*.

Conversely, at the lowest redshifts probed by this study ($z \simeq 1$) it is seen that, while bulge-dominated objects are on the rise, pure-bulge galaxies (i.e. objects comparable to present-day giant ellipticals) have yet to emerge in significant numbers, with >90 per cent of these high-mass galaxies still retaining a significant disc component. This is compared with 64 per cent of the local $M_* > 10^{11}$ M$_\odot$ galaxy population, which would be classified as pure-bulges from our definition ($B/T > 0.9$, corresponding to $n > 3.5$ from Fig. 4) from the sample of Buitrago et al. (2011).

7.3 Star-forming and passive discs

The primary aim of this paper is to focus on the morphological analysis of the H_{160} images, with a full treatment of the SEDS, including dependence of morphology on wavelength, deferred to a future paper. Nevertheless, in Fig. 8 we make use of the SED fitting already employed in the sample selection to explore the relationship between star formation activity and morphological type.

Fig. 8 shows specific sSFR versus morphological type for the massive galaxies in our sample, where morphology is quantified by single-Sérsic index in the left-hand panel, and by bulge-to-total H_{160}-band flux ratio (B/T) in the right-hand panel. The values of sSFR plotted are derived from the original optical–infrared SED fits employed in the sample selection, and include correction for dust extinction as assessed from the best-fitting value of A_V derived during the SED fitting. As a check of the potential failure of this approach to correctly identify reddened dusty star-forming

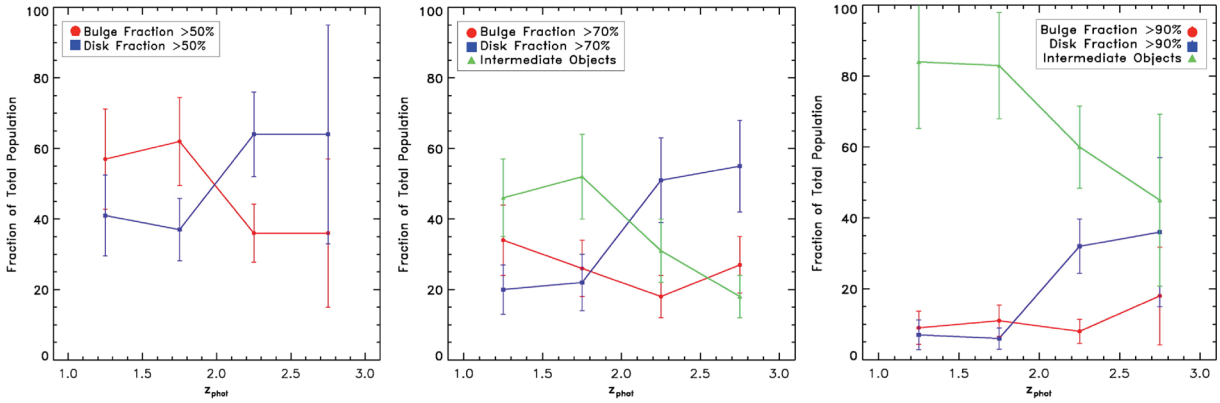

Figure 7. The redshift evolution of the morphological fractions in our galaxy sample, after binning into redshift bins of width $\Delta z = 0.5$. We show three alternative cuts in morphological classification, both to try to provide a complete picture, and to facilitate comparison with different categorizations in the literature. In the left-hand panel we have simply split the sample into two categories: bulge-dominated ($B/T > 0.5$) and disc-dominated ($B/T < 0.5$). In the central panel we have separated the sample into three categories, with any object for which $0.3 < B/T < 0.7$ classed as 'Intermediate'. Finally, in the right-hand panel we have expanded this Intermediate category to encompass all objects for which $0.1 < B/T < 0.9$ (see Section 7.2 for discussion).

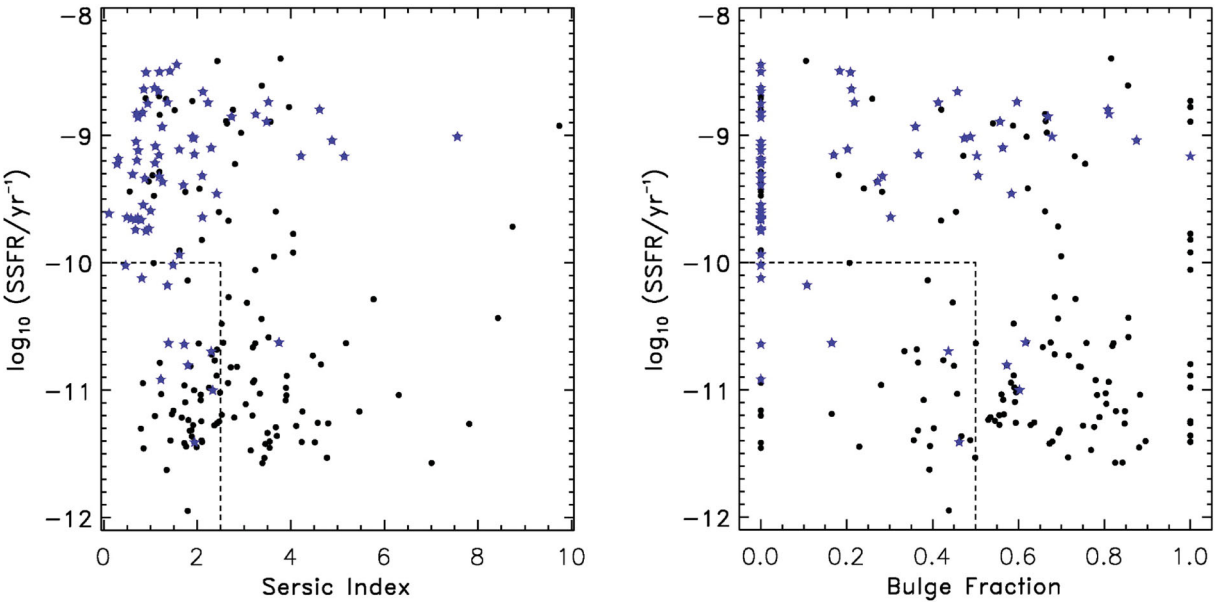

Figure 8. Plots of sSFR versus morphological type as judged by single-Sérsic index (left-hand panel) and bulge-to-total H_{160}-band flux ratio (B/T) (right-hand panel). The values of sSFR plotted are derived from the original optical–infrared SED fits employed in the sample selection, and include correction for dust extinction as assessed from the best-fitting value of A_V derived during the SED fitting. Highlighted by blue stars are those galaxies which we found have a 24 μm counterpart in the *Spitzer* SpUDS MIPS imaging of the UDS, indicative of some dust enshrouded star formation and/or AGN activity. It is clear from these plots that the vast majority of disc-dominated galaxies are star forming, and the majority of bulge-dominated galaxies are not (as judged by sSFR $< 10^{-10}\,\mathrm{yr}^{-1}$). However, we have indicated by a box on both the panels the region occupied by a potentially interesting population of passive disc-dominated objects; in the left-hand panel disc-dominated is defined as $n < 2.5$, and 52 ± 9 per cent of the quiescent galaxies lie within this box, while in the right-hand panel disc-dominated is defined by $B/T < 0.5$, in which case 34 ± 7 per cent of the quiescent objects lie within this region.

galaxies, we have also searched for 24 μm counterparts in the *Spitzer* SpUDS MIPS imaging of the UDS, and have highlighted in blue those objects which yielded a MIPS counterpart within a search radius of <2 arcsec. Reassuringly, relatively few 24 μm detections have been uncovered in the lower regions of the panels shown in Fig. 8, while the vast majority of star-forming objects are confirmed via MIPS counterparts. This shows that the determination of sSFR as deduced from the optical–mid-infrared SED fitting has been (perhaps surprisingly) good at cleanly separating the star-forming galaxies from the more quiescent objects.

It is clear from these plots that the majority of disc-dominated galaxies are star forming, whereas the majority of bulge-dominated galaxies are not (as judged by sSFR $< 10^{-10}\,\mathrm{yr}^{-1}$). Nonetheless, the sample also undoubtedly contains star-forming bulge-dominated galaxies and, perhaps more interestingly, a significant population of apparently quiescent disc-dominated objects, which we quantify and discuss further below.

First, though, we note that the most obvious feature of Fig. 8 is the prominent group of pure-disc galaxies which dominate the star-forming population. Since we already emphasized in Fig. 7 that the pure-disc population is largely confined to $2 < z < 3$, it becomes clear that, at $z > 2$, our massive galaxy sample is dominated by disc-dominated/pure-disc star-forming galaxies. As we discuss in a related CANDELS paper, this population of massive star-forming discs at $2 < z < 3$ is, to first order, the same as the population of submillimetre galaxies revealed by continuum submillimetre and millimetre wavelength surveys over the last decade (Targett et al. 2012).

Equally interesting, however, is the apparently significant population of quiescent discs revealed on these plots. To highlight and quantify this population we have indicated by a box on both the panels the region occupied by objects with disc-dominated morphologies and sSFR $< 10^{-10}\,\mathrm{yr}^{-1}$. In the left-hand panel, disc-dominated is defined as $n < 2.5$, and 52 ± 9 per cent of the quiescent galaxies lie within this box (40 ± 7 per cent if we exclude the 24 μm detections as indicating obscured star formation activity), while in the right-hand panel, disc-dominated is defined by $B/T < 0.5$, in which case 34 ± 7 per cent of the quiescent objects lie within this region (25 ± 6 per cent if we exclude the 24 μm detections).

As discussed further in Sections 8.3 and 8.4, quiescent disc galaxies are of particular interest because they suggest that the quenching or exhaustion of star formation activity need not be simply linked to a process (e.g. major merging) which is also directly associated with inducing morphological transformations. We re-emphasize that it is clear the majority of disc-dominated galaxies in our sample are star forming, and that this is true for an even clearer majority of the pure discs. However, our sample does appear to include a significant population of quiescent disc-dominated objects, including $\simeq$5 pure discs (10 pure discs lie in the box, but the upper five of these possess 24 μm detections indicating that they may be reddened star-forming discs, or contain obscured AGN; note that at the depth of the *Spitzer* SpUDS MIPS imaging, and the redshifts and masses of interest here, a significant detection at 24 μm always corresponds to an sSFR above our adopted threshold of sSFR $= 10^{-10}\,\mathrm{yr}^{-1}$ if the mid-infrared emission is interpreted as due to star formation activity).

We have double-checked that none of the quiescent disc-dominated objects not already marked by the blue stars in Fig. 8 (indicating a counterpart in the MIPS catalogue) have even marginal detections in the 24 μm imaging. We have also checked that this population is not biased towards higher redshift, which might make MIPS detections more challenging. We thus conclude that this population really is quiescent as judged by sSFR, and needs to be explained in any viable model of galaxy formation/evolution.

7.4 Axial-ratio distributions

Some additional (and independent) information on the morphologies of the galaxies in our sample can potentially be gained from examining the distribution of their axial ratios. In Fig. 9 we have split our sample into disc-dominated ($B/T < 0.5$) and bulge-dominated ($B/T > 0.5$) galaxies, and then plotted the axial-ratio distributions of the disc components in the disc-dominated galaxies (left-hand panel), and of the bulge components in the bulge-dominated galaxies (right-hand panel) (we do this to avoid potential contamination of these plots by poorly constrained axial ratios from weak subcomponents; Fig. 9 thus displays the axial-ratio distributions of our more robustly measured discs and bulges). In addition, in each panel we split the subsamples further into star-forming (black outlined histogram) or quiescent (shaded grey histogram) objects, as again defined by whether a given galaxy lies above or below our adopted specific star formation threshold $\mathrm{sSFR} = 10^{-10}\,\mathrm{yr}^{-1}$.

From the right-hand panel of Fig. 9 it can be seen that the axial-ratio distributions of the star-forming and quiescent bulges are indistinguishable, both peaking around $b/a \simeq 0.7$ [the Kolmogorov–Smirnov (KS) test yields $p = 0.71$ for the null hypothesis that they are drawn from the same distribution]. This result is consistent with previous studies of bulge-dominated objects, both at low (Padilla & Strauss 2008) and high redshifts (Ravindranath et al. 2006).

Perhaps of more interest are the axial distributions of the disc components as plotted in the left-hand panel of Fig. 9. Here the two distributions look markedly different (although the statistical significance of the difference is marginal; $p = 0.09$). Specifically, it appears that the passive discs display a fairly flat distribution (as expected for a set of randomly oriented thin discs), whereas the star-forming discs display a significantly more peaked distribution, in fact indistinguishable from the axial-ratio distributions displayed by the bulges.

The flat axial-ratio distribution found for the passive disc-dominated galaxies lends some additional support to our conclusion that we have uncovered a genuine population of passive disc-dominated galaxies, but the peaked distribution of the star-forming discs might be viewed as surprising. However, these results agree well with other recent studies of star-forming disc-dominated galaxies at comparable redshifts, as we illustrate in Fig. 10. The left-hand panel of Fig. 10 shows again the axial-ratio distribution of our star-forming discs (simply taken from the left-hand panel of Fig. 9), but this time overplotted with results from Law et al. (2012), who utilized a larger sample of galaxies at $z \sim 1.5$–3.6, but plot only the single-Sérsic model axial ratios of $n \simeq 1$ galaxies. It can be seen that the two distributions are in good agreement, both peaked around $b/a \simeq 0.6$–0.7, and displaying a deficit of objects with $b/a < 0.3$; these results are also consistent with those obtained by Ravindranath et al. (2006) who used *HST* ACS optical data to model the rest-frame ultraviolet (UV) morphologies of galaxies at $z \sim 3$–4, and with Yuma et al. (2011) who conduct a similar analysis at $z \simeq 2$. The implications of these peaked axial-ratio distributions are discussed further in Section 8.4.

Finally, in the right-hand panel of Fig. 10 we confirm that the axial-ratio distribution displayed by our *passive* discs at $1 < z < 3$ is indeed consistent with that displayed by the disc-galaxy population at low redshift as deduced from the SDSS. Tha axial-ratio distribution for our passive discs is shown here both with and without inclusion of the 24-μm-detected objects, to demonstrate that its shape is unchanged by this extra level of caution in excluding potential star-forming objects. These histograms have been overplotted with the data points and best-fitting model from Padilla & Strauss (2008); their normalized frequencies have simply been re-scaled here by the area under our solid histogram to ease direct comparison with our results. As can be seen, our distribution agrees well with the relatively flat distribution displayed by present-day disc-dominated galaxies. We also compared our results with the axial-ratio distribution presented by van der Wel et al. (2011) for a sample of 14 $z \simeq 2$ disc-dominated passive galaxies, and found them to be consistent, although the statistics are weak given the limited size of both samples ($p = 0.15$).

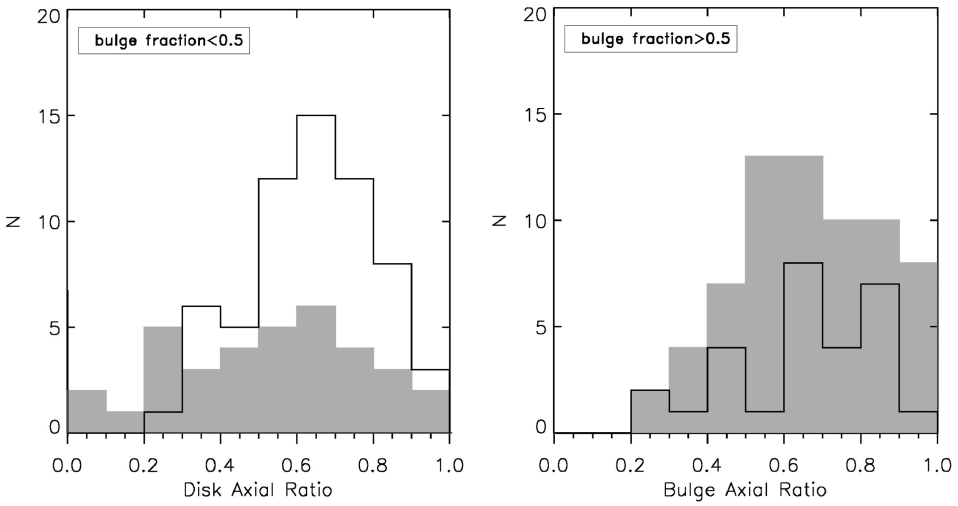

Figure 9. Axial-ratio distributions displayed by the dominant disc components in the disc-dominated galaxies ($B/T < 0.5$; left-hand panel) and by the dominant bulge components in the bulge-dominated galaxies ($B/T > 0.5$; right-hand panel). These subsamples have been further split into star-forming objects ($\mathrm{sSFR} < 10^{-10}\,\mathrm{yr}^{-1}$; black outlined histograms) and quiescent objects ($\mathrm{sSFR} < 10^{-10}\,\mathrm{yr}^{-1}$; grey shaded histograms). Both the star-forming and quiescent bulge populations show similar distributions peaked, as broadly expected, at $b/a \simeq 0.7$. However, the active and passive disc populations are marginally different, with the passive discs showing a relatively flat distribution as seen for low-redshift discs (see also Fig. 10), while the star-forming discs display a peaked distribution more comparable to that displayed by the bulges (see text for details and KS statistics).

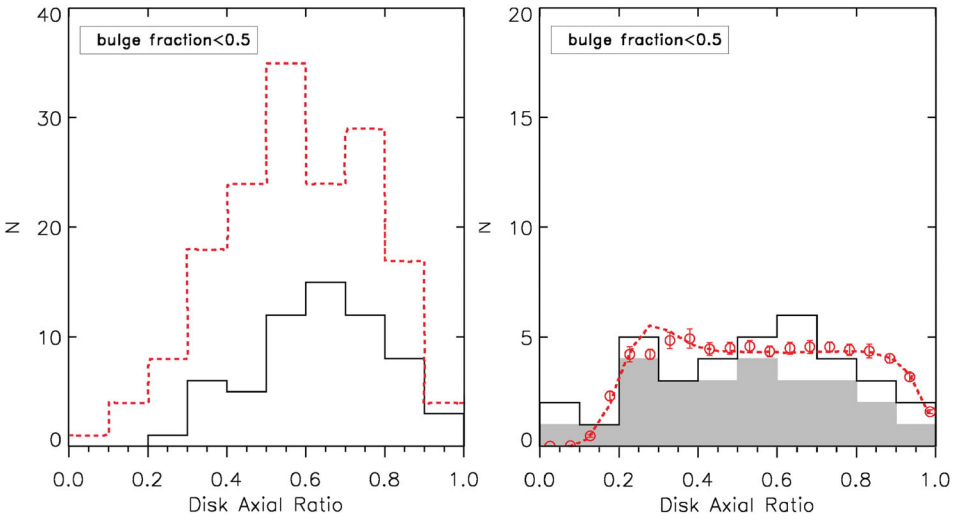

Figure 10. Comparison of our disc-galaxy axial-ratio distributions with other relevant recent results from the literature. In the left-hand panel we again plot the axial-ratio distribution of our *star-forming* discs (in black solid outline), but also overplot (in the red/dashed histogram) the axial-ratio distribution of $n \simeq 1$, $z \simeq$ 1.5–3.6 star-forming disc galaxies from Law et al. (2012); the two distributions are indistinguishable. In the right-hand panel we plot (in black solid outline) the axial-ratio distribution of our *passive* discs as judged by sSFR $= 10^{-10}\,\mathrm{yr}^{-1}$ from SED fitting and overplot (in grey shaded regions) the corresponding distribution after excluding the apparently passive discs which appear to have 24 μm counterparts. These are compared with local results in the form of the best-fitting model axial-ratio distribution (red dashed line) and the actual measured distribution of axial ratios from a fitted single-component model (red points with corresponding error bars) of local SDSS spiral galaxies from Padilla & Strauss (2008) (here we plot their normalized frequency scaled appropriately for direct comparison with our results). This comparison illustrates that the relatively flat axial-ratio distribution displayed by our sample of passive discs at $1 < z < 3$ is consistent with results from local discs, whilst the peaked distribution of star-forming galaxies is in good agreement with previous studies of similar galaxies conducted at $z \simeq 2$.

8 DISCUSSION

We now discuss the implications of our results in the context of other recent studies of massive galaxies at comparable redshifts, and current models of galaxy formation and evolution.

8.1 Galaxy growth

Based on a complete, mass-selected sample of ≃200 galaxies with $M_* > 10^{11}\,\mathrm{M}_\odot$, our *HST* WFC3/IR study provides the most detailed information to date on the sizes of the most massive galaxies at $1 < z < 3$. Considering the sample as a whole, our most basic statistical measurement is that the median size of these galaxies is 2.6 ± 0.2 kpc, a factor of 2.3 ± 0.1 smaller than the size of comparably massive galaxies today. Splitting the sample into $z < 2$ and $z > 2$ subsamples yields a gentle trend with redshift, with the median descending from 2.7 ± 0.3 kpc at $1 < z < 2$, to 2.5 ± 0.3 kpc at $2 < z < 3$, corresponding to factors of 2.2 ± 0.2 and 2.3 ± 0.2 below the local size–mass relation. These figures are somewhat (≃20 per cent) smaller than the results reported for a comparable mass-selected sample of galaxies at comparable redshifts by van Dokkum et al. (2010) ($R_\mathrm{e} \simeq 4 \pm 0.3$ kpc at $z \simeq 1.6$, $R_\mathrm{e} \simeq 3 \pm 0.3$ kpc at $z \simeq 2.0$), but their results were based on stacks of ground-based images taken in 1.1 arcsec seeing, and are thus superseded by the results presented here.

However, these basic statistics conceal a number of potentially important details. First, the scatter in size is large, spanning ≃1 dex (see Fig. 5b) and, due to our relatively small errors on R_e (<10 per cent; e.g. Fig. 1) and our exploration of systematic effects (e.g. Fig. 2), we can say with confidence that this scatter is real. Our analysis reveals that massive galaxies display half-light radii which range from $R_\mathrm{e} \simeq 8$ kpc, fully consistent with comparably massive local galaxies, to $R_\mathrm{e} \simeq 1$ kpc, consistent with the very small sizes previously reported for the most extreme examples of compact galaxies at these redshifts (e.g. Kriek et al. 2009).

Secondly, when our galaxies are split into their bulge and disc components, it is clear that the bulges display more rapid evolution to small sizes, both in terms of median size, and in terms of the relative numbers of objects which lie on and below the present-day size–mass relation. For the discs, we find that, throughout our redshift range, ≃40 per cent lie on the local relation, with ≃60 per cent below, while for the bulges the percentage of objects which lie significantly below the local relation rises from an already high 80 per cent at $1 < z < 2$ to 85 per cent at $2 < z < 3$. Clearly bulges consistent with the local size–mass relation are rare at these redshifts and, moreover, the compact bulge population appears to become increasingly compact with increasing look-back time, lying a factor of 3.5 ± 0.5 below the local relation at $1 < z < 2$ but a factor of 4.4 ± 0.3 below at at $2 < z < 3$ (the corresponding figures for the subset of compact discs are more modest, 2.4 ± 0.4 and 2.5 ± 0.2, respectively). Here, our results for bulges match very well those recently reported by Szomoru et al. (2012), who used the CANDELS imaging in GOODS-South to deduce that quiescent galaxies at $1.5 < z < 2.5$ with median Sérsic indices $n \simeq 3.7$ lie a factor of ≃4 in size below the local size–mass relation. A related issue is the morphological mix of the objects selected as compact. For example, it has recently been suggested by van der Wel et al. (2011) (albeit based on a sample of only 14 objects) that the 'majority' of compact galaxies at $z \simeq 2$ are disc-dominated. Fig. 6 illustrates that such a statement is not straightforward, as it depends on what one defines as compact and what mass range is to be considered. Certainly it is clear from Fig. 6 that the most massive and compact objects (i.e. the galaxies with $M_* > 2 \times 10^{11}\,\mathrm{M}_\odot$, and $R_\mathrm{e} < 3$ kpc) are *all* bulge-dominated, but at more moderate masses the situation is certainly

more mixed. A direct comparison is limited by the somewhat complex mix of criteria used by van der Wel et al. (2011) to classify an object as disc-dominated (as compared to our straightforward use of $B/T < 0.5$) but clearly Fig. 6 does reveal a substantial population of compact discs as quantified above, and we confirm that essentially all the *passive* discs are comparably compact to their spheroidal counterparts.

Thirdly, while our sample is clearly somewhat limited in terms of dynamic range in stellar mass, we find evidence for a lower envelope in size which tracks the slope of the present-day size–mass relation. This trend is strengthened by the results of our bulge+disc decomposition, which extends the size–mass relation down to estimated subcomponent masses $M_* \simeq 2 \times 10^{10}\,\mathrm{M}_\odot$. Thus, for $M_* > 2 \times 10^{11}\,\mathrm{M}_\odot$ we find no objects significantly smaller than $R_\mathrm{e} \simeq 1$ kpc, while at $M_* < 1 \times 10^{11}\,\mathrm{M}_\odot$ we start to see examples of even smaller bulges and discs, with some bulges as small as $R_\mathrm{e} \simeq 0.4$ kpc. These details, including the trend of minimum size with stellar mass are important when comparing with previous studies; for example, Szomoru et al. (2010) have reported a very small scalelength of $R_\mathrm{e} = 0.42 \pm 0.14$ kpc from WFC3/IR imaging of a compact bulge-dominated galaxy at $z = 1.91$, but with an estimated stellar mass of $M_* \simeq 5 \times 10^{10}\,\mathrm{M}_\odot$ (Wuyts et al. 2008), it is clear that this object lands perfectly on the lower envelope of the size–mass relation displayed by our bulge components in Fig. 6. The single object studied by Szomoru et al. (2010) was the most massive, quiescent $z \simeq 2$ galaxy available for study in the *Hubble Ultra Deep Field*. A comparably detailed study of the brightest galaxy at $z > 1.5$ in the 10-times-larger ERS field by van Dokkum & Brammer (2010) again yielded a Sérsic index $n \simeq 4$, but this time an effective radius $R_\mathrm{e} \simeq 2.1 \pm 0.3$ kpc and a much larger galaxy mass $M_* \simeq 4 \times 10^{11}\,\mathrm{M}_\odot$; again, comparison with the results shown in Fig. 6 shows that this is perfectly consistent with the size–mass locus for bulges uncovered here. We also note that within Fig. 6 we see no real evidence in support of the claim advanced by Ryan et al. (2012) that the required size growth of galaxies from $z \simeq 1.5$ to the present is a strong function of stellar mass. A direct comparison is difficult because our extension to lower masses is primarily based on bulge+disc decomposition, but we note here that Cimatti, Nipoti & Cassata (2012) also find no evidence for any stellar mass dependence in the redshift growth rate of early-type galaxies.

Fourthly, it is also clear that the objects which remain on the local relation, even out to the highest redshifts, are star-forming discs, with the passive galaxies, including the passive disc components, confined to the more compact population. This result mirrors that recently reported by McLure et al. (2012) who found, for spectroscopically confirmed galaxies of comparably high mass at $z \simeq 1.4$, that all objects with low sSFR (i.e. $\mathrm{sSFR} < 10^{-10}\,\mathrm{Gyr}^{-1}$) lie below the present-day size–mass relation, irrespective of morphological classification. At $z \simeq 2.3$ a comparable trend for star-forming objects to be two to three times larger then their quiescent counterparts has been reported by Kriek et al. (2009) for a sample of 28 galaxies with $M_* \simeq 3 \times 10^{10}\,\mathrm{M}_\odot$, a result confirmed as extending to even lower masses by Szomoru et al. (2011), who also found star-forming galaxies at $z \simeq 2$ to be larger than their quiescent counterparts in the mass range $M_* \simeq 1$–$10 \times 10^{10}\,\mathrm{M}_\odot$.

In summary, our results confirm and clarify a number of trends in the galaxy size–mass relation previously reported from detailed studies of small numbers of objects with *HST*, or larger samples studied via ground-based imaging. Within the high-mass regime our study provides significantly improved statistics on the scatter in size, and how the size–mass relation evolves differently for bulges and discs in the redshift range $1 < z < 3$. Our bulge+disc decomposition is the most extensive attempted to date, and suggests that these trends extend to the bulge components of disc-dominated galaxies, and to the disc components of bulge-dominated galaxies. We also provide the first clear evidence for a lower envelope in size which our bulge+disc decomposition suggests extends from our high-mass sample down to lower masses ($M_* \simeq 2 \times 10^{10}\,\mathrm{M}_\odot$), tracking the slope of the present-day size–mass relation.

Many authors have discussed the theoretical challenge of explaining the growth in the size of massive galaxies from $z \simeq 2$ to the present. Various arguments, based on ΛCDM simulations, clustering analyses (e.g. Quadri et al. 2007; Hartley et al. 2010) and simple comoving number density comparisons (e.g. van Dokkum et al. 2010) indicate that the $M_* \simeq 10^{11}\,\mathrm{M}_\odot$ galaxies studied here at $1 < z < 3$ must evolve into galaxies with stellar masses $M_* \simeq 3 \times 10^{11}\,\mathrm{M}_\odot$ which are essentially all giant elliptical galaxies on the high-mass end of the local early-type size–mass relation plotted in red in Fig. 6. The issue of what happens to the disc components so evident in the high-redshift population (but essentially absent in the present-day descendants) is discussed further below. But in terms of size evolution, the challenge is to explain how such compact massive galaxies (especially the extremely compact bulges at $z > 2$ which lie a factor of ≃4 below the present-day relation) can evolve on to the present-day size–mass relation without simultaneously attaining excessively high masses which violate constraints imposed by the measured present-day mass function (Baldry et al. 2012).

As pointed out by various authors (e.g. McLure et al. 2012), major mergers do not provide a sufficiently vertical evolutionary track on the size–mass plane to lift the compact high-redshift galaxies on to the present-day relation without yielding excessively high masses. In any case, size growth driven primarily by major mergers would require many more major mergers since $z \simeq 2$ than appears plausible from N-body simulations (which suggest <2 per massive galaxy by the present day; e.g. Hopkins et al. 2010b), or indeed from observed merger rates (e.g. Robaina et al. 2010).

Thus while the rare major mergers may be responsible for the relaxation process which at some stage destroys the disc component (although a series of minor mergers may also achieve this; Naab, Burkert & Hernquist 1999; Bournaud, Jog & Combes 2007) it appears that the bulk of the size growth must be attributed to minor mergers which are much more effective at adding stars and dark matter in the outer regions of galaxies, increasing observed size with relatively limited increase in stellar mass. It is also worth noting that minor mergers are more effective than major mergers at raising the dark matter to stellar mass ratio to the levels observed for the most massive galaxies today, are better able to add mass while leaving the age and metallicity gradients in the central regions of massive galaxies unscrambled, and may provide a natural explanation for the kinematically decoupled cores frequently observed in present-day ellipticals (e.g. van den Bosch et al. 2008).

As illustrated by McLure et al. (2012), a combination of five minor (mass ratio 1:10) mergers and a single major merger (mass ratio 1:3) appears sufficient to achieve the required evolution since $z \simeq 1.4$. Recent simulations analysed by Oser et al. (2012) also support the idea that minor mergers can produce the required size evolution at $z < 2$. However, whether this sort of evolutionary path can also solve the problem for the most compact spheroids at $z > 2$ is still a matter of some debate (Cimatti et al. 2012; Newman et al. 2012).

Finally, it is worth emphasizing that despite the ongoing debate of how such compact high-redshift galaxies can climb on to the present-day size–mass relation, the existence of such compact objects at early times, while perhaps initially unexpected, is in fact a natural prediction of modern galaxy-formation simulations (e.g. Khochfar & Silk 2006; Obreschkow & Rawlings 2009; Hopkins et al. 2010a; Wuyts et al. 2010).

8.2 Morphological evolution

As the bulge components decline in size with increasing redshift, we also find a clear trend for the massive galaxies in our sample to become increasingly disc-dominated. As shown in Fig. 7, $z \simeq 2$ appears to mark a morphological transition epoch, at least for our chosen galaxy mass range; crudely speaking, the majority of our galaxies are bulge-dominated ($B/T > 0.5$) at $z < 2$, while the situation is reversed at $z > 2$. Moreover, at the highest redshifts ($z \simeq 2.5$), over half the galaxies have $B/T < 0.3$ and over half of these (i.e. $\simeq$35 per cent of all objects in the relevant redshift range) are 'pure discs' as judged by $B/T < 0.1$ (which we cannot distinguish from $B/T = 0$). Such highly disc-dominated objects are virtually absent in our high-mass sample by $z \simeq 1.5$, although it is still true that the vast majority of objects contain some detectable disc component, with 'pure de Vaucouleurs bulges' (i.e. $B/T > 0.9$) still largely absent until $z < 1$.

The relative lack of pure de Vaucouleurs bulges at $z > 1$ appears broadly consistent with the findings of Buitrago et al. (2011) who reported that ellipticals have been the dominant morphological class for massive galaxies only since $z \sim 1$, although a direct comparison of our results is difficult as Buitrago et al. (2011) did not attempt bulge+disc decomposition and relied on a combination of single-Sérsic fitting and visual classification.

The presence of a significant fraction of disc-dominated objects, even among the apparently passive subsample, has already been reported at $z \simeq 1.5$ for masses $M_* > 10^{11}\,\mathrm{M}_\odot$ by McLure et al. (2012) (44 ± 12 per cent) and at $z \simeq 2$ for masses $M_* > 6 \times 10^{10}\,\mathrm{M}_\odot$ by van der Wel et al. (2011) (40–65 per cent). However, these studies do not extend to high enough redshift to capture the full extent to which disc-dominated galaxies, primarily star forming, come to dominate the massive galaxy population at $z > 2$ as illustrated in Figs 7 and 8.

Given the axial-ratio distributions plotted in Figs 9 and 10, it might be argued that, while the more passive discs may indeed be discs, the star-forming disc-like objects might be more triaxial in nature, given their more peaked (i.e. typical rounder) axial ratios. However, as discussed further in the next subsection, visual inspection of both the active and passive disc dominated objects supports the view that they are indeed discs; the only mystery is the lack of any very thin edge-on discs in the star-forming population which we return to at the end.

It is worth again bearing in mind that virtually all the objects in this study are destined to evolve into today's very massive $M_* > 3 \times 10^{11}\,\mathrm{M}_\odot$ giant elliptical galaxies which display, at most, very low level disc components. This alone means it may be naive to expect the properties of many of these discs to correspond closely to those of $M_* \simeq 1 \times 10^{11}\,\mathrm{M}_\odot$ disc galaxies in the present-day Universe. Indeed it has been argued that the stellar densities of these high-redshift massive discs are comparable to those found in the cores of massive present-day bulges (Bezanson et al. 2009; van Dokkum et al. 2010), consistent with the inside-out model of massive galaxy growth discussed above.

8.3 Star-forming and quiescent galaxies

This paper is deliberately focused on H_{160} morphologies, with a detailed analysis of the colours of the bulge and disc components deferred to a future paper. Nevertheless, as explained in Section 7.3, the SED fitting undertaken to deduce the photometric redshifts also yielded dust-corrected SFRs and stellar masses, from which we can derive an estimate of sSFR for each galaxy in our sample. As illustrated in Fig. 8, we have then followed Bell et al. (2012) by also searching for 24 μm detections to try to ensure against misinterpreting dust-reddened star-forming galaxies as quiescent objects. In general the results of this latter test are reassuring, with the vast majority of star-forming objects (defined as sSFR $> 10^{-10}\,\mathrm{yr}^{-1}$) yielding 24 μm detections, as compared to relatively few of the objects with UV sSFR $> 10^{-10}\,\mathrm{yr}^{-1}$ being detected by the SpUDS MIPS imaging. As already summarized in Section 7.3, the vast majority of the disc-dominated galaxies are star forming, while the majority of the bulge-dominated objects are quiescent, but yet our sample contains a significant number of star-forming bulges and a significant number of 'quiescent' discs; 25–50 per cent of the passive subsample are disc-dominated, depending on whether one splits by Sérsic index or B/T, and on whether the few 24 μm detections of the supposedly passive objects are deemed symptomatic of star formation or buried AGN.

Thus, to first order, our results show that the well-documented bimodality in the colour–morphology plane seen at low redshift, where spheroidal galaxies inhabit the red sequence, while disc galaxies occupy the blue cloud (Baldry et al. 2004; Driver et al. 2006; Drory & Fisher 2007) is at least partly already in place by $z \simeq 2$. However, the colour–morphology division is undoubtedly much less clean than in the nearby Universe, and a key challenge is to determine the prevalence and physical significance of the passive discs and the active bulges.

Recent studies have produced apparently conflicting results over the prevalence or otherwise of massive passive discs at these redshifts. Specifically, while van der Wel et al. (2011) and McLure et al. (2012) both conclude that $\simeq$50 per cent of passive objects at these redshifts are disc dominated, Bell et al. (2012) find that the key parameter which correlates best with quiescence at these redshifts is still Sérsic index, with the presence of a substantial bulge a necessary (but not necessarily sufficient) condition for the termination of star formation activity. This confusion may be partly a matter of definition; it is not clear what a 'substantial' bulge component means, or how comparable the morphological criteria applied in these studies really are. Nevertheless, given the controversy over this issue, and its potential importance, we have carefully revisited the passive disc-dominated objects in our sample, motivated in part by the fact that five of the 10 apparently passive 'pure discs' (i.e. $B/T < 0.1$) originally isolated on the basis of optical/near-infrared photometry in Fig. 8 transpired to have 24 μm detections.

In Fig. 11 we show the H_{160} image stamps for these 10 interesting objects, along with their 24 μm MIPS imaging. The 24 μm detections of the five MIPS catalogue-matched objects (shown in the bottom row) are clear, but equally clear is the fact the the top five objects do not possess even marginal mid-infrared detections at the depth of the SpUDS imaging. We note that the 24-μm-detected objects in the bottom row of Fig. 11 have fluxes which, if interpreted as arising from star formation, imply typical values of sSFR $\simeq 10^{-9}\,\mathrm{yr}^{-1}$, and that the SpUDS MIPS detection limit conveniently corresponds rather closely to the adopted passive/active sSFR threshold of sSFR $\simeq 10^{-10}\,\mathrm{yr}^{-1}$ (for galaxies in this redshift and mass range). Thus, since we have no real reason to assign the MIPS detections to AGN

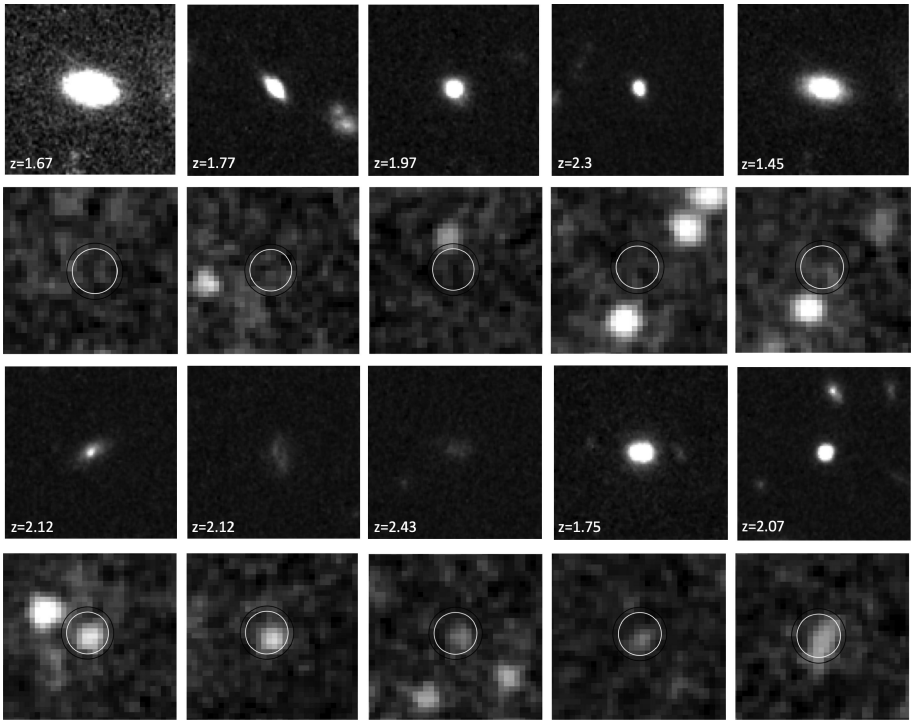

Figure 11. The WFC3/IR H_{160} and *Spitzer* 24 μm images of the 10 apparently bulgeless pure-disc objects in our sample which the optical–near-infrared SED fitting suggests are passive (i.e. sSFR $< 10^{-10}\,\mathrm{yr}^{-1}$). The top row shows 6×6 arcsec images of the five objects which have no significant 24 μm counterpart, as shown in the 20×20 arcsec MIPS image stamps in the second row (the circle indicates a 5 arcsec radius aperture, which is a very generous search radius). The third and fourth rows show the same information for the five objects which do have 24 μm counterparts.

activity (other than the fact that several of these objects prefer a small contribution from a point source rather than a resolved bulge in the multicomponent H_{160} modelling) we have taken a conservative approach, and have classified the lower five objects in Fig. 11 as star forming, which reduces the number of passive 'pure' discs by half, to five. This represents less than 15 per cent of the 'pure disc' sample, and so clearly the vast majority of *apparently bulgeless* discs are actively star-forming galaxies on the main sequence. Nevertheless, this still means that a substantial fraction of the passive galaxy subsample (25–40 per cent) is disc-dominated, and it is as yet unclear whether the relative rarity of completely bulgeless quiescent discs reflects an important causal link between bulge growth and passivity at these redshifts, or is simply an inevitable symptom of the dimming of star-forming discs as star formation activity dries up (for whatever reason). These issues, and the prospects for further progress, are discussed further in Section 8.4.

Moving now to consider the active discs, we attempt to investigate a little further the apparent contradiction between the results of our Sérsic fitting and the axial-ratio distribution displayed by these supposedly disc-like star-forming objects. As already mention in Section 7.4 (and see Figs 9 and 10) while the axial distribution for the passive disc components is as flat as that displayed by low-redshift disc galaxies, that displayed by the star-forming 'discs' does not extend to such low values, and peaks at $b/a \simeq 0.7$. This is essentially identical to the distribution found by Law et al. (2012), who also commented that such an axial-ratio distribution was more in line with that expected from a population of triaxial objects.

We have therefore tried to check whether our active disc-dominated objects do indeed look like star-forming discs. This is somewhat against the spirit of our analysis which seeks to deliberately avoid the pitfalls of visual classification. Nevertheless, image inspection can still offer an interesting sanity check on the interpretation of modelling results. In Fig. 12, we therefore show, for illustrative purposes, the images, model-fits and residual data-model images of the five star-forming galaxies which we find to have Sérsic indices closest to unity (in practice, $n \simeq 0.9$–1.1). By (possible) coincidence all five of these objects are in fact fairly round, but it is visually obvious that they are not spheroidal galaxies, but rather face-on discs with spiral arms and/or star-forming clumps. We are thus left to conclude that we have no reason to really doubt the disc-like nature of these objects just because of their axial-ratio distribution. Perhaps it is simply the case that very few of the (violently) star-forming discs at these epochs are genuinely thin enough to display low axial ratios, or alternatively such discs may be so dusty that near edge-on examples have in fact evaded our detection limit (this might seem unlikely, but see Targett et al. 2012).

A full review of the already extensive observational and theoretical literature on the nature and importance of clumps in star-forming disc galaxies at $z \simeq 2$ is beyond the scope of this paper. Suffice to say that, given the above-mentioned lack of evidence for major mergers being the primary driver of elliptical galaxy evolution, it has now been suggested that the progenitors of today's giant ellipticals are these high velocity dispersion, clumpy discs, in which star formation is fed by cold streams and minor mergers (e.g. Dekel, Sari & Ceverino 2009b; Ceverino, Dekel & Bournaud 2010; Ceverino et al. 2012) with the clumps eventually coalescing to form a spheroid. However, this view of the potential importance of the observed clumps in building bulges (e.g. Guo et al. 2012) has been challenged observationally (e.g. Wuyts et al. 2012) and theoretically

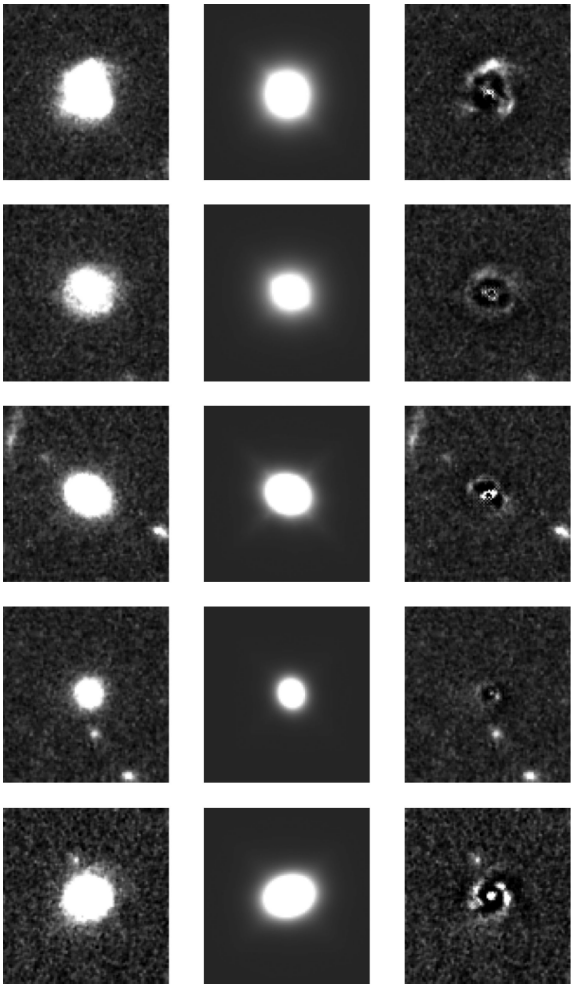

Figure 12. H_{160} images (left), models (centre) and model-data residual (right) (all 6×6 arcsec) for a subset of five of our star-forming (sSFR $> 10^{-10}\,\mathrm{yr}^{-1}$) disc-dominated ($B/T < 0.5$) galaxies. The five galaxies shown here have been chosen to have single-Sérsic indices in the range $\simeq$0.9–1.1 thus demonstrating that, despite the bulge-like axial-ratio distributions for our sample of star-forming galaxies (as discussed in Section 7.4), the galaxies with single-Sérsic index consistent with traditional disc-like ($n = 1$) values show clear face-on disc morphologies, and are not especially disturbed systems. In addition our residual image stamps highlight the clumpy structure within these discs, as expected for violently star-forming discs at high redshift (see Section 8.3).

(e.g. Genel et al. 2012). Nevertheless, whether or not the clumps are the direct ancestors of bulges, what is clear from our study is that the majority of progenitors of today's most massive elliptical galaxies are indeed, at least at $2 < z < 3$, clumpy, and fairly extended, star-forming disc galaxies (a result reinforced by the properties of the extreme star-forming galaxies as deduced from the CANDELS imaging of submillimetre galaxies by Targett et al. 2012).

Finally, we note that the presence of at least some star-forming spheroids in our $1 < z < 3$ sample is unsurprising. Various authors have observed this before at comparable redshifts, including Bell et al. (2012) who, while arguing that bulge formation was a potentially necessary condition for the quenching of star formation, also concluded that it was not sufficient to ensure this, given the presence of star-forming galaxies in their sample with $n > 2.5$ (although see also Wang et al. 2012).

8.4 Passive discs and quenching

We conclude this discussion by exploring further the nature of the apparently passive disc-dominated objects in our sample, and considering briefly the potential implications for the the connection, if any, between termination of star formation activity and morphological transformation.

As already noted, the axial-ratio distributions presented in Figs 9 and 10 suggest that the passive discs in our sample have similar intrinsic shapes to low-redshift discs, while, on average, the star-forming discs do not. As a final check on the nature of the passive discs we show, in Fig. 13, images of the model discs fitted to all 25 of the confirmed passive discs in our sample (i.e. those with $B/T < 0.5$ and sSFR $< 10^{-10}\,\mathrm{yr}^{-1}$ which also have no 24 μm detection). In this plot the discs are shown at high resolution [i.e. full width at half-maximum (FWHM) 0.05 arcsec] and scaled to comparable surface brightness levels, making it easier to see the full range of axial ratios found. This figure demonstrates that the flat axial-ratio distribution of passive discs is not a result of strange, excessively elongated or otherwise unphysical discs which GALFIT has attempted to fit to deal with other peculiarities in the data. In addition, the full range of fitted sizes can be seen at a wide range of axial ratios (i.e. viewing angles). We thus have no reason to doubt that these are, as suggested by the Sérsic and double-component fits, genuine passive discs.

The presence of a significant population of passive discs among the massive galaxy population at these redshifts indicates that star formation activity can cease without a disc-galaxy being turned directly into a disc-free spheroid, as generally previously expected if the process that quenches star formation is a major merger. Thus, while some fraction of the substantial population of star-forming discs may indeed suffer a major merger (possibly transforming rapidly into a compact passive spheroid, although see also Kaviraj et al. 2012) our results argue that another process must exist which is capable of terminating star formation activity while leaving a substantial disc intact.

One possibility arises from the latest generation of hydrodynamical simulations (Kereš et al. 2005; Dekel et al. 2009a) and analytic theories (Birnboim & Dekel 2003; Dekel & Birnboim 2006), which suggest a formation scenario whereby at high redshift star formation in massive discs takes place through inflows of cold gas until the dark matter haloes in which the galaxies reside reach a critical mass ($>10^{12}\,\mathrm{M}_{\odot}$) below $z = 2$. At this point the virial temperature of the haloes is high enough to prevent efficient cooling such that pressure can be built to support a stable extended virial shock, which can be triggered by minor mergers. This results in the galaxy residing in a hot medium and below $z = 2$ a stable shock can also be sustained in the cold streams, which stops cold gas inflowing and quenches star formation, but does not cause any accompanying change in underlying morphology.

The idea that star formation quenching and morphological transformation are distinct processes is also consistent with the empirical description of Peng et al. (2010), who suggest that, in this high-mass regime, the star formation quenching of galaxies is driven by a process governed by 'mass-quenching', where the rate of star formation suppression is proportional to the SFR of the galaxy (although Peng et al. do not attempt to posit a physical mechanism responsible for this observed relation).

Another scenario which can account for star formation quenching, whilst still being consistent with the existence of passive discs, is the model of violent disc instabilities (Dekel et al. 2009b; Ceverino et al. 2010; Cacciato, Dekel & Genel 2012). This model

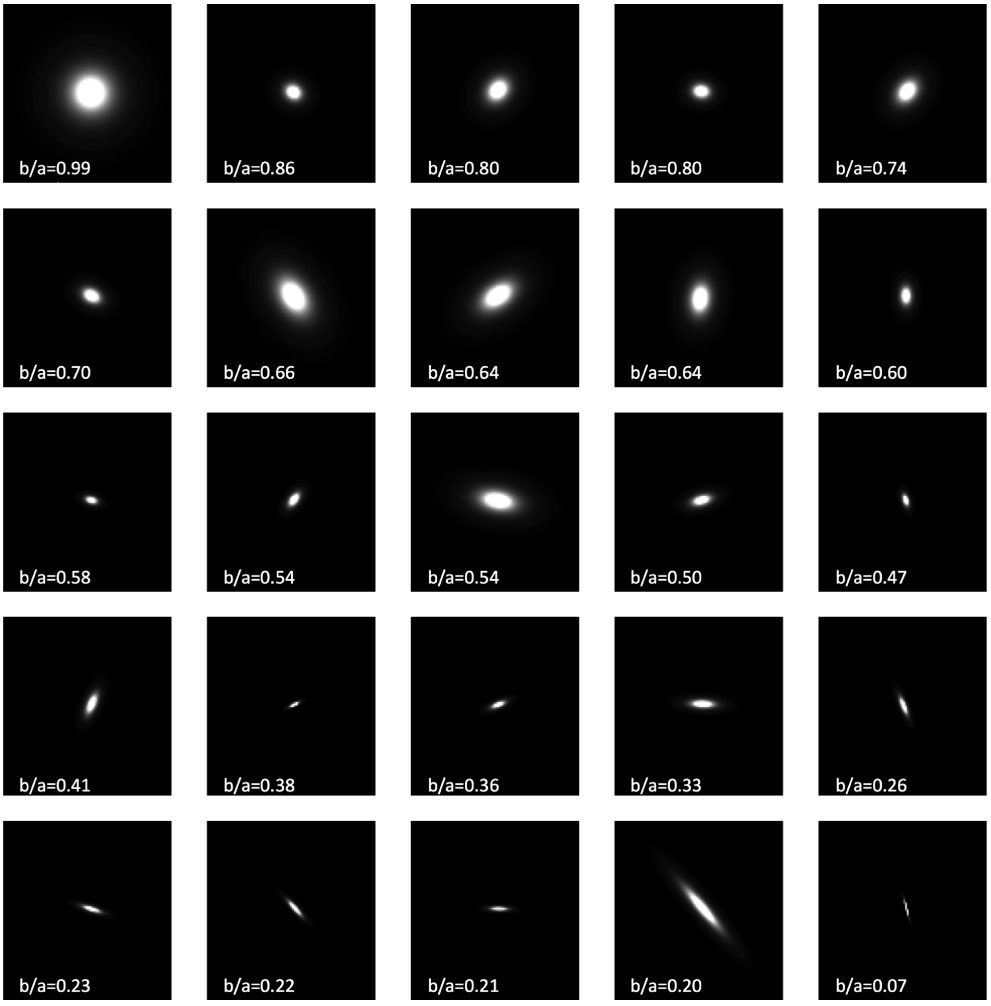

Figure 13. The model disc components of the 25 disc-dominated ($B/T < 0.5$) galaxies within our sample which show no evidence for star formation from either SED fitting (sSFR $< 10^{-10}\,\mathrm{yr}^{-1}$) or 24 μm counterparts. The models have been constructed from the best-fitting disc parameters from our double-component analysis and have been convolved with a model PSF generated from a Gaussian of FWHM = 0.05 arcsec, providing artificial imaging comparable to that achievable by *HST* at the bluest optical wavelengths. Each stamp is again 6 × 6 arcsec in size, and the grey-scale for these images is set at black = 0 and white = 1/3 of the maximum pixel value of each image, so as to provide consistent brightness cuts for each stamp at an appropriate level. The models have been ranked by descending axial ratio from the top left to the bottom right (the value of axial ratio, *b*/*a* is given in the corner of each stamp). These are the 25 models which were used to produce the axial-ratio distribution of passive discs shown in Fig. 10 (in the grey histogram of Fig. 10b), and this illustration shows that there is no reason to doubt that they are genuine discs (i.e. no disc displays an unreasonable scalelength, and discs covering the full range of fitted sizes are apparently visible over the full range of inclination angles). This provides further evidence of the genuine disc-like morphologies of these passive systems, the implications of which are discussed in Sections 8.3 and 8.4.

suggests that, as the disc evolves, there is an inflow of mass to the centre of the disc, which gradually builds to form a massive bulge. This mass inflow can quench star formation whilst still retaining a massive disc in a process known as 'morphology quenching' (Martig et al. 2009). In addition to this, it also agrees with the observed trend in morphologies with redshift observed in this study, i.e. the transition from predominantly bulge systems in the local Universe, to the increase in mixed bulge+disc morphologies between $1 < z < 2$, and then the dominance of disc-dominated objects beyond $z = 2$.

Finally, returning to the data, in considering the possible evolutionary links between the active and passive discs in our sample, we must remember that there are important observational differences between these populations. First, while the passive discs are not especially compact (median disc-component $r_e = 2.6 \pm 0.7$ kpc), they are, on average, significantly smaller that the active discs (median disc-component $r_e = 4.0 \pm 0.5$ kpc). However, it is not clear that this is a serious problem; Fig. 6 shows a significant fraction of the active discs are also reasonably compact and, in any case, some scenarios (e.g. the model of morphology quenching described above) might naturally lead to a disc reducing in size somewhat as star formation activity turns off. Secondly, of course, we still need to explain how the relatively thin discs in the passive population emerge from a star-forming population which apparently lacks objects with low axial ratios. Again, it is hard to know if this is a real problem. It seems entirely plausible that a maximally unstable, violently star-forming disc will settle down into a significantly flatter configuration once the fuelling source of, and violent feedback from star formation activity ceases, but (to our knowledge) this has yet to be convincingly and quantitatively demonstrated by simulations. There are also still potential issues of selection effects which might mean that edge-on star-forming discs are unrepresented in flux-limited optical–UV selected samples (due, possibly, to dust

obscuration). Interestingly, the axial-ratio distribution presented by Targett et al. (2012) for the extreme population of star-forming discs selected via submillimetre emission is relatively flat, and statistically indistinguishable from the axial-ratio distribution displayed by the passive discs in the current study.

9 CONCLUSIONS

We have isolated a sample of $\simeq$200 galaxies in the CANDELS-UDS field for which we have determined stellar masses $M_* > 10^{11}\,M_\odot$, and photometric redshifts in the range $1 < z < 3$. These objects are relatively bright, being selected from a parent sample with $H_{160} < 24.5$ (a factor of 10 brighter than the CANDELS WFC3/IR 5σ detection limit of $H_{160} < 27$), and in practice virtually all objects have $H_{160} < 23$ (equivalent to 100σ detections). Consequently, we have been able to exploit the exquisite CANDELS imaging to undertake a detailed analysis of their rest-frame optical morphologies, and how these vary as a function of redshift, mass and SFR.

Crucial to this work is proper control of both the random and systematic errors. We have undertaken a detailed study of the form of the adopted PSF, constructing and justifying the use of an empirical on-image PSF over that produced by the TINYTIM modelling software. We have also explored in detail the effect of errors in background determination on both the best-fitting values of, and errors in, the derived physical parameters such as Sérsic index and effective radius. In addition we have placed a high premium on the importance of obtaining formally acceptable model fits to as many objects as possible, in order to enable realistic error estimation. In the end, via careful object-by-object masking, and the use of models ranging from single-Sérsic fits to disc+bulge+point-source combinations, we achieved satisfactory models for $\simeq$95 per cent of the massive galaxies in our complete $1 < z < 3$ sample.

Armed with the resulting unparalleled, robust morphological information on massive galaxies during this key epoch in cosmic history, we have been able to reach the following conclusions.

(1) Our single-Sérsic results indicate that these massive galaxies at $1 < z < 3$ lie both on and below the local size–mass relation, with a median effective radius of $\sim$2.6 kpc, a factor of $\simeq$2.3 smaller than comparably massive local galaxies.

(2) Our study is the first to attempt bulge+disc decomposition on such a large sample at these redshifts. We find that bulges in particular show evidence for a growing bimodality in the size–mass relation with increasing redshift; the fraction of bulges consistent with the local size–mass relation is 20 ± 5 per cent at $1 < z < 2$, and 15 ± 9 per cent at $2 < z < 3$, while the offset in size of the (dominant) compact population from the the local early-type relation is already a factor of 3.5 ± 0.5 at $1 < z < 2$ and rises to a factor 4.4 ± 0.3 at $2 < z < 3$. These trends appear to extend to the bulge components we have isolated from the disc-dominated galaxies, and we find evidence that the lower envelope of galaxy size is a function of mass which broadly parallels the local relation; no galaxies more compact than $R_e = 1$ kpc are found at masses $M_* > 2 \times 10^{11}\,M_\odot$, while bulges as small as $R_e < 0.5$ kpc are found at lower stellar masses $M_* \simeq 5 \times 10^{10}\,M_\odot$.

(3) The statistics for discs are less dramatic, with $\simeq 40 \pm 8$ per cent of discs still consistent with the relevant local size mass relation over our full redshift range, and the offset of the compact population from the local late-type relation growing gently from a factor 2.4 ± 0.4 at $1 < z < 2$, to 2.5 ± 0.2 at $2 < z < 3$. We do, however, find that the objects which remain consistent with the present-day size–mass relation are virtually all active star-forming discs, with the population of apparently passive discs confined to the more compact subset.

(4) Even within the relatively limited redshift range of our study, we find evidence for dramatic changes in the morphologies of massive galaxies with redshift, with $z \simeq 2$ apparently marking a key transition epoch. While similarly massive galaxies at low redshift are generally bulge-dominated (and the expected more massive $M_* \simeq 3 \times 10^{11}\,M_\odot$ descendants of our high-redshift galaxies are virtually all giant ellipticals today), by a redshift of $1 < z < 2$ they are predominantly mixed bulge+disc systems, and by $z > 2$ they are mostly disc-dominated. Furthermore, at the lowest redshifts covered by this study while bulge-dominated objects are on the rise, pure-bulge galaxies (i.e. objects comparable to present-day giant ellipticals) have yet to emerge in significant numbers, with >90 per cent of these high-mass galaxies still retaining a significant disc component.

(5) We find that the majority of the disc-dominated galaxies are actively forming stars, although this is also true for many of the bulge-dominated systems. Interestingly, however, while most of the quiescent galaxies are bulge-dominated (indicating early emergence of the red sequence), we find that a significant fraction (25 ± 6 per cent using a disc-dominated definition of $B/T < 0.5$, and 40 ± 7 per cent using a disc-dominated definition of $n < 2.5$) of the most quiescent galaxies, with sSFR $< 10^{-10}\,\mathrm{yr}^{-1}$, have disc-dominated morphologies (including a small number (five) of 'pure disc' galaxies with $B/T < 0.1$). We show that these passive discs appear to be 'normal' discs in the sense that they display an axial-ratio distribution comparable to that displayed by present-day discs, while the more prevalent actively star-forming discs seem, on average, rounder and clumpier. We consider various possible reasons for this, including selection effects, and briefly discuss the theoretical implications.

Our results challenge theoretical models of galaxy formation to (i) include a mode in which star formation quenching is not simply connected to morphological transformation, (ii) explain the relationship between active and passive discs, (iii) predict the relatively rapid demise of massive star-forming discs, but the relatively gradual emergence of genuinely bulge-dominated morphologies, and (iv) provide the necessary dramatic size evolution (but with limited mass increase) to lift the compact bulges we see at $z \simeq 2$ on to the local size–mass relation $\simeq 10$ Gyr later.

ACKNOWLEDGMENTS

We acknowledge the contribution from an anonymous referee via a careful and thoughtful report. VAB and MC acknowledge the support of the Science and Technology Facilities Council (STFC) via the award of an STFC Studentship and an STFC Advanced Fellowship, respectively. JSD and TAT acknowledge the support of the European Research Council via the award of an Advanced Grant. JSD and RJM acknowledge the support of the Royal Society via a Wolfson Research Merit Award and a University Research Fellowship, respectively. RJM acknowledges the support of the Leverhulme Trust via the award of a Philip Leverhulme Research Prize. DJC acknowledges the support of an Australian Research Council QEII Fellowship. The work of AD has been partly supported by the ISF through grant 6/08, by GIF through grant G-1052-104.7/2009, by the DFG via DIP grant STE1869/1-1.GE625/15-1 and by an NSF grant AST-1010033 at UCSC.

This work is based in part on observations made with the NASA/ESA *Hubble Space Telescope*, which is operated by the

Association of Universities for Research in Astronomy, Inc, under NASA contract NAS5-26555. This work is based in part on observations made with the *Spitzer Space Telescope*, which is operated by the Jet Propulsion Laboratory, California Institute of Technology under NASA contract 1407.

REFERENCES

Baldry I. K., Glazebrook K., Brinkmann J., Ivezić Ž., Lupton R. H., Nichol R. C., Szalay A. S., 2004, ApJ, 600, 681
Baldry I. K. et al., 2012, MNRAS, 421, 621
Bamford S. P. et al., 2009, MNRAS, 393, 1324
Bell E. F. et al., 2012, ApJ, 753, 167
Bertin E., Arnouts S., 1996, A&A, 117, 393
Bezanson R., van Dokkum P. G., Tal T., Marchesini D., Kriek M., Franx M., Coppi P., 2009, ApJ, 697, 1290
Birnboim Y., Dekel A., 2003, MNRAS, 345, 349
Bournaud F., Jog C. J., Combes F., 2007, A&A, 476, 1179
Bower R. G., Benson A. J., Malbon R., Helly J. C., Frenk C. S., Baugh C. M., Cole S., Lacey C. G., 2006, MNRAS, 370, 645
Bruzual G., Charlot S., 2003, MNRAS, 344, 1000
Buitrago F., Trujillo I., Conselice C. J., Bouwens R. J., Dickinson M., Yan H., 2008, ApJ, 687, L61
Buitrago F., Trujillo I., Conselice C. J., Haeussler B., 2011, MNRAS, preprint (arXiv:1111.6993)
Cacciato M., Dekel A., Genel S., 2012, MNRAS, 421, 818
Calzetti D., Armus L., Bohlin R. C., Kinney A. L., Koornneef J., Storchi-Bergmann T., 2000, ApJ, 533, 682
Cameron E., Driver S. P., Graham A. W., Liske J., 2009, ApJ, 699, 105
Cameron E., Carollo C. M., Oesch P. A., Bouwens R. J., Illingworth G. D., Trenti M., Labbé I., Magee D., 2011, ApJ, 743, 146
Ceverino D., Dekel A., Bournaud F., 2010, MNRAS, 404, 2151
Ceverino D., Dekel A., Mandelker N., Bournaud F., Burkert A., Genzel R., Primack J., 2012, MNRAS, 420, 3490
Cimatti A. et al., 2008, A&A, 482, 21
Cimatti A., Nipoti C., Cassata P., 2012, MNRAS, 422, L62
Croton D. J. et al., 2006, MNRAS, 365, 11
Daddi E. et al., 2005, ApJ, 626, 680
Damjanov I. et al., 2009, ApJ, 695, 101
De Lucia G., Blaizot J., 2007, MNRAS, 375, 2
de Vaucouleurs G., 1948, Ann. Astrophys., 11, 247
Dekel A., Birnboim Y., 2006, MNRAS, 368, 2
Dekel A. et al., 2009a, Nat, 457, 451
Dekel A., Sari R., Ceverino D., 2009b, ApJ, 703, 785
Driver S. P. et al., 2006, MNRAS, 368, 414
Drory N., Fisher D. B., 2007, ApJ, 664, 640
Drory N., Salvato M., Gabasch A., Bender R., Hopp U., Feulner G., Pannella M., 2005, ApJ, 619, L131
Fan L., Lapi A., De Zotti G., Danese L., 2008, ApJ, 689, L101
Fan L., Lapi A., Bressan A., Bernardi M., De Zotti G., Danese L., 2010, ApJ, 718, 1460
Fontana A. et al., 2004, A&A, 424, 23
Franx M., van Dokkum P. G., Schreiber N. M. F., Wuyts S., Labbé I., Toft S., 2008, ApJ, 688, 770
Furusawa H. et al., 2008, ApJS, 176, 1
Genel S. et al., 2012, ApJ, 745, 11
Glazebrook K. et al., 2004, Nat, 430, 181
Graham A. W., 2011, in 'Planets, Stars and Stellar Systems'. Springer, preprint (arXiv:1108.0997)
Granato G. L., De Zotti G., Silva L., Bressan A., Danese L., 2004, ApJ, 600, 580
Grogin N. A. et al., 2011, ApJS, 197, 35
Guo Y. et al., 2009, MNRAS, 398, 1129
Guo Y., Giavalisco M., Ferguson H. C., Cassata P., Koekemoer A. M., 2011, ApJ, 757, 120
Hartley W. G. et al., 2010, MNRAS, 407, 1212
Häussler B. et al., 2007, ApJS, 172, 615
Holden B. P., van der Wel A., Rix H.-W., Franx M., 2012, ApJ, 749, 96
Hopkins P. F., Cox T. J., Younger J. D., Hernquist L., 2009, ApJ, 691, 1168
Hopkins P. F., Bundy K., Hernquist L., Wuyts S., Cox T. J., 2010a, MNRAS, 401, 1099
Hopkins P. F. et al., 2010b, ApJ, 724, 915
Ilbert O. et al., 2010, ApJ, 709, 644
Kaviraj S. et al., 2012, MNRAS, preprint (arXiv:1206.2360)
Kereš D., Katz N., Weinberg D. H., Davé R., 2005, MNRAS, 363, 2
Khochfar S., Silk J., 2006, ApJ, 648, L21
Koekemoer A. M. et al., 2011, ApJS, 197, 36
Kriek M., van Dokkum P. G., Franx M., Illingworth G. D., Magee D. K., 2009, ApJ, 705, L71
Kriek M. et al., 2010, ApJ, 722, L64
Krist J., 1995, in Shaw R. A., Payne H. E., Hayes J. J. E., eds, ASP Conf. Ser. Vol. 77, Astronomical Data Analysis Software and Systems IV. Astron. Soc. Pac., San Francisco, p. 349
Lackner C. N., Gunn J. E., 2012, MNRAS, 421, 2277
Law D. R., Steidel C. C., Shapley A. E., Nagy S. R., Reddy N. A., Erb D. K., 2012, ApJ, 745, 85
Lawrence A. et al., 2007, MNRAS, 379, 1599
Longhetti M. et al., 2007, MNRAS, 374, 614
Madau P., 1995, ApJ, 441, 18
Mancini C. et al., 2010, MNRAS, 401, 933
Maraston C., 2005, MNRAS, 362, 799
Martig M., Bournaud F., Teyssier R., Dekel A., 2009, ApJ, 707, 250
Masters K. L. et al., 2010, MNRAS, 405, 783
McGrath E. J., Stockton A., Canalizo G., Iye M., Maihara T., 2008, ApJ, 682, 303
McLure R. J. et al., 2012, MNRAS, preprint (arXiv:1205.4058)
Michałowski M. J., Dunlop J. S., Cirasuolo M., Hjorth J., Hayward C. C., Watson D., 2012, A&A, 541, A85
Muzzin A., van Dokkum P., Franx M., Marchesini D., Kriek M., Labbé I., 2009, ApJ, 706, L188
Naab T., Burkert A., Hernquist L., 1999, ApJ, 523, L133
Naab T., Johansson P. H., Ostriker J. P., Efstathiou G., 2007, ApJ, 658, 710
Naab T., Johansson P. H., Ostriker J. P., 2009, ApJ, 699, L178
Newman A. B., Ellis R. S., Bundy K., Treu T., 2012, ApJ, 746, 162
Obreschkow D., Rawlings S., 2009, MNRAS, 400, 665
Oser L., Naab T., Ostriker J. P., Johansson P. H., 2012, ApJ, 744, 63
Padilla N. D., Strauss M. A., 2008, MNRAS, 388, 1321
Peng C. Y., Ho L. C., Impey C. D., Rix H.-W., 2002, ApJ, 124, 266
Peng Y. et al., 2010, ApJ, 721, 193
Pozzetti L. et al., 2007, A&A, 474, 443
Quadri R. et al., 2007, ApJ, 654, 138
Ragone-Figueroa C., Granato G. L., 2011, MNRAS, 414, 3690
Ravindranath S. et al., 2006, ApJ, 652, 963
Rix H.-W. et al., 2004, ApJS, 152, 163
Robaina A. R., Bell E. F., van der Wel A., Somerville R. S., Skelton R. E., McIntosh D. H., Meisenheimer K., Wolf C., 2010, ApJ, 719, 844
Ryan R. E., Jr, et al., 2012, ApJ, 749, 53
Salimbeni S., Fontana A., Giallongo E., Grazian A., Menci N., Pentericci L., Santini P., 2009, in Giobbi G., Tornambe A., Raimondo G., Limongi M., Antonelli L. A., Menci N., Brocato E., eds, AIP Conf. Ser. Vol. 1111, Probing Stellar Populations Out to the Distant Universe. Am. Inst. Phys., New York, p. 207
Sekiguchi K., Akiyama M., Furusawa H., Simpson C., Takata T., Ueda Y., Watson M. W., SXDS Team, 2005, in Renzini A., Bender R., eds, Multiwavelength Mapping of Galaxy Formation and Evolution. Springer, Berlin, p. 82
Sérsic J. L., 1968, Atlas de galaxias australes. Observatoriò Astronomico, Cordoba
Shankar F., Marulli F., Bernardi M., Mei S., Meert A., Vikram V., 2011, MNRAS, preprint (arXiv:1105.6043)
Shen S., Mo H. J., White S. D. M., Blanton M. R., Kauffmann G., Voges W., Brinkmann J., Csabai I., 2003, MNRAS, 343, 978
Simard L., Mendel J. T., Patton D. R., Ellison S. L., McConnachie A. W., 2011, ApJS, 196, 11
Stockton A., McGrath E., Canalizo G., Iye M., Maihara T., 2008, ApJ, 672, 146

Szomoru D. et al., 2010, ApJ, 714, L244
Szomoru D., Franx M., Bouwens R. J., van Dokkum P. G., Labbé I., Illingworth G. D., Trenti M., 2011, ApJ, 735, L22
Szomoru D., Franx M., van Dokkum P. G., 2012, ApJ, 749, 121
Targett T. A., Dunlop J. S., McLure R. J., Best P. N., Cirasuolo M., Almaini O., 2011, MNRAS, 412, 295
Targett T. A. et al., 2012, MNRAS, preprint (arXiv:1208.3464)
Taylor E. N., Franx M., Glazebrook K., Brinchmann J., van der Wel A., van Dokkum P. G., 2010, ApJ, 720, 723
Toft S. et al., 2007, ApJ, 671, 285
Trujillo I. et al., 2006, ApJ, 650, 18
Trujillo I., Conselice C. J., Bundy K., Cooper M. C., Eisenhardt P., Ellis R. S., 2007, MNRAS, 382, 109
Trujillo I., Cenarro A. J., de Lorenzo-Cáceres A., Vazdekis A., de la Rosa I. G., Cava A., 2009, ApJ, 692, L118
Trujillo I., Carrasco E. R., Ferré-Mateu A., 2012, ApJ, 751, 45
van den Bosch R. C. E., van de Ven G., Verolme E. K., Cappellari M., de Zeeuw P. T., 2008, MNRAS, 385, 647
van der Wel A., Bell E. F., van den Bosch F. C., Gallazzi A., Rix H.-W., 2009, ApJ, 698, 1232
van der Wel A. et al., 2011, ApJ, 730, 38
van Dokkum P. G., Brammer G., 2010, ApJ, 718, L73
van Dokkum P. G. et al., 2008, ApJ, 677, L5
van Dokkum P. G. et al., 2010, ApJ, 709, 1018
Wang T. et al., 2012, ApJ, 752, 134
Wuyts S., Labbé I., Schreiber N. M. F., Franx M., Rudnick G., Brammer G. B., van Dokkum P. G., 2008, ApJ, 682, 985
Wuyts S., Cox T. J., Hayward C. C., Franx M., Hernquist L., Hopkins P. F., Jonsson P., van Dokkum P. G., 2010, ApJ, 722, 1666
Wuyts S. et al., 2012, ApJ, 753, 114
Yuma S., Ohta K., Yabe K., Kajisawa M., Ichikawa T., 2011, ApJ, 736, 92
Zibetti S., Gallazzi A., Charlot S., Pierini D., Pasquali A., 2012, MNRAS, preprint (arXiv:1205.4717)
Zirm A. W. et al., 2007, ApJ, 656, 66

APPENDIX A: PSF DEPENDENCE

We show in Fig. A1 radial profile plots of the two PSFs tested here, the empirical stellar stack and the TINYTIM model, along with the residuals between them and a magnified plot between 0.5 and 0.8 arcsec, the range encompassing a physical size comparable to the fitted sizes of the objects (which more clearly demonstrates

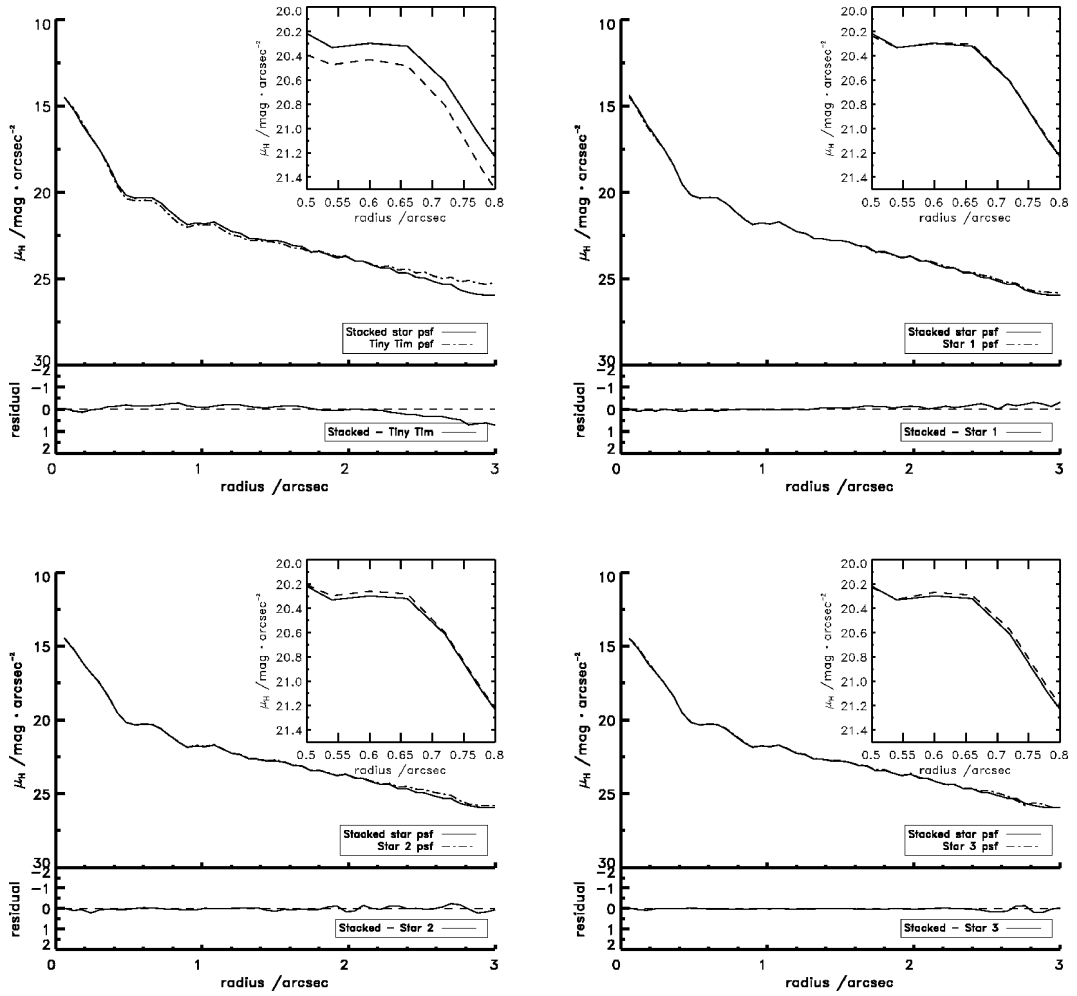

Figure A1. Comparison of the radial surface brightness profiles of alternative H_{160} PSFs. The top-left panel compares the empirical PSF we obtained from stacking stars taken from the real H_{160} CANDELS mosaic (solid line) with the PSF produced by the TINYTIM model (dashed line) (with the residuals given below). The inset shows a magnified view of the crucial region around 6 arcsec, which corresponds to a physical size of $\simeq$5 kpc at $1 < z < 3$, comparable to the typical effective radii of the galaxies in our sample (the surface brightness scale in the inset has been expanded to demonstrate more clearly the level of the offset between the TINYTIM model and the empirical stack at these important scales). The remaining three panels simply show how well the empirical PSF matches the profiles of three of the seven individual stars which went into it, demonstrating that our empirical PSF has not been significantly broadened or otherwise damaged by the stacking process at any angular scales of interest.

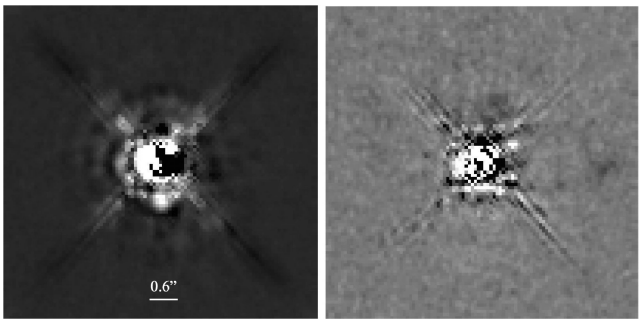

Figure A2. Left: difference image of the stacked empirical PSF – the TINYTIM model. The image is 6 × 6 arcsec with a pixel scale of 0.06 arcsec (an illustrative 0.6 arcsec line has been added for clarity). The grey-scale shows negative pixels as darker and positive pixels as whiter. The discrepancy between the two PSFs at the centre is due to minor mismatching during centroiding, but a real positive halo can be clearly seen at a radius of 0.5 arcsec and greater. This is due to the empirical PSF including a stronger airy disc pattern than is modelled by the TINYTIM PSF, and perhaps also containing additional scattered light. Inconsistencies in the contribution from diffraction spikes are also visible in the image. Right: a difference image of the stacked PSF – one of the component star PSFs is given for comparison, where the images have been constructed using the same cut in the brightness level.

the difference between the PSFs). In the top-left plot we show the difference between the empirical stacked PSF and the TINYTIM model. The other plots are included to emphasize the uniformity of the individual stars that were included in the stack as they compare the stack with three out of the seven stars that comprise the stack.

This figure clearly highlights that the TINYTIM model underpredicts the flux in the PSF at this critical radius and thus explains why the fitted sizes using this PSF are 5–10 per cent larger than those from the empirical stacked PSF.

In order to ascertain the reason for this discrepancy between the modelled and empirical PSFs we constructed a difference image of the empirical stack – TINYTIM PSF, shown in Fig. A2. The offsets at the very centre of the image are due to centroiding issues but it is clear that further out, beyond 0.5 arcsec, there is a distinct halo in the empirical PSF which is not present in the TINYTIM model. This unequivocally shows that the empirical stacked PSF contains a much stronger contribution from the airy rings, which is not properly modelled by the TINYTIM PSF. In addition to this, the TINYTIM model does not accurately reproduce the diffraction spikes.

As a result of these tests, we adopted the empirical stacked PSF for all the model fitting and testing undertaken in this work. Consequently we have generally derived fitted sizes which are systematically a factor of 5–10 per cent smaller than those which would have been determined using a TINYTIM PSF.

APPENDIX B: BACKGROUND DEPENDENCE

In Section 4.2 we discuss the additional level of background subtraction needed before the image stamps taken from the CANDELS mosaics can be fitted with GALFIT, and how the fitting procedure trades off the treatment of background light with the fitting of the the degenerate Sérsic index and effective radius parameters. We fully explored this issue by constructing a grid of GALFIT runs throughout the full parameter space of Sérsic index and effective radius parameters, and background subtraction values.

This grid contains a set of additional background values to be subtracted from the image. This is done by determining two initial estimates of the additional background light. The first is done by masking out an aperture of radius 1 arcsec around the object centroid position and calculating the median background value in the remaining 6 × 6 arcsec image stamp. This method provides a reliable estimate of the median background light in most cases, with the exception of those for the largest objects in our sample. These largest objects are particularly susceptible to biased size estimates as careful consideration must be given to their extended wings. For these cases it is clear that the masking of a 1 arcsec radius aperture may not be sufficient to mask out the full extent of the wings, therefore for every object we adopt a second median background estimator. This secondary method expands the image stamp of each object to 12 × 12 arcsec, generates an annular aperture centred on each source with an inner radius of 3 arcsec and an outer radius of 5 arcsec, and measures the median background light within this aperture. By adopting this second technique, although our median background estimate is conducted further from the source, it ensures we have not biased our median background estimate too high by failing to account properly for the extended wings of the largest objects.

For each object we therefore have two estimates of the local median background, where comparison of these estimates gives us an indication of the error associated with determining median background estimates from the CANDELS images. We find that the offset between these two estimates for each object is well described by a Gaussian distribution centred on 0 with a 2 × FWHM value of 0.001 electrons s^{-1} (for comparison the typical sky level has a mean value of 2.12×10^{-4} electrons s^{-1} with a standard deviation of 3.33×10^{-4}). We subsequently use this 2 × FWHM as the error associated with any median background estimate, where the factor of two was chosen to minimize the parameter space searched while ensuring that all possible best-fitting backgrounds for each object were still included in the parameter space.

From our inspection of the individual sources we are aware that sources can be equally subject to background oversubtraction from the first order analysis performed on the images, as well as undersubtraction. Thus, for each object, we generate a grid of additional background subtraction values to be used in the fitting procedure, which is taken to be the range −0.001 to +0.001 electrons s^{-1} (where −0.001 is the upper limit of background light that will be added back into the image, accounting for original oversubtraction, and +0.001 is the upper limit to the amount of background light that will be additionally subtracted off the images, accounting for original undersubtraction).

For each of the points in additional background subtraction space we then construct a loop over Sérsic index and effective radius parameters allowed in the fit. We run an initial fit on every object using the median additional background subtraction value determined above using a 1 arcsec masking aperture. The Sérsic index and effective radius parameters returned for these fits are used as the centroid points for the Sérsic index and effective radius loops. For Sérsic index we construct a loop of steps of 0.1 in size, and for effective radius we make steps of size 0.025 arcsec. These step sizes have been determined to incorporate the full range of generally accepted realistic Sérsic index and effective radius values (i.e. 0.1–10 in Sérsic index and 0.025–2 arcsec in angular effective radius).

For each point in the effective radius and Sérsic index grid we lock these values during the GALFIT fit and step through a range of different additional background subtraction values to find the best-fitting background subtraction value at that grid point, using the χ^2 values of each background fit.

APPENDIX C: MODEL FIT REFINEMENT

As detailed in Section 6.2 a significant fraction of our sample (∼30 per cent) were initially found to have statistically unacceptable model fits, as judged by

$$\chi^2 > \nu + 3(\sqrt{(2\nu)}). \quad \text{(C1)}$$

However, from close visual inspection of these objects it was found that they display additional levels of complex structure such as $z < 2$ grand design spirals with clear spiral arms, interacting systems, objects in very crowded fields and objects with extremely close companions, which have not been separately identified by SEXTRACTOR despite the high level of de-blending employed in our catalogue generation (DEBLEND_MINCONT = 0.0008). Examples of these systems are shown in Fig. C1, and they contain some of the best examples of prominent spiral structure.

By additional masking based on closer examination of the residual images of the model fits to these complex systems (and refinements to our fitting procedure), we have been able to achieve formally acceptable model fits to the vast majority of these objects. Furthermore, from comparison of the morphological parameters fitted by our general procedure and those from the refined procedure employed on this subset of systems, we find that, despite the unacceptable χ^2 statistics produced by the initial attempt to model these objects, we did in fact successfully recover their key morphological parameters (even if errors on these quantities would have been underestimated on the basis of $\delta\chi^2$) despite the presence of additional high surface brightness features which cannot be reproduced by our smooth models. This is clearly illustrated in Fig. C2, which shows the tight correlation between the underlying physical properties determined from our initial general fitting procedure and the first stage of additional modelling refinement.

Our refinement procedure is outlined in Section 6.2 and, in brief, incorporates masking of pixels for which the model fit to our data exceeds a certain χ^2 threshold. This serves to mask out any additional structure, which is not modelled by our symmetric Sérsic profiles, by ensuring that such pixels are not considered during the fitting process, and so do not contribute to the χ^2 returned for the overall fit.

Our first refinement involved setting the χ^2 threshold for each pixel at 9, the point at which secondary structure became clearly visible in the χ^2 maps of these objects, and the point in the χ^2 distribution for all pixels for these objects where the distribution has peaked and begins to fall into the tail. Applying the refinement with this threshold improved the fits of 32 objects to within statistically acceptable levels, but we were still left with a further 37 objects which still failed to meet the acceptability criterion.

Accordingly, we re-ran our modelling with a lower χ^2 threshold for a second refinement in the fitting. This second pass used a χ^2 threshold of 5, a value cutting further into the main distribution of the χ^2 values for each pixel (from inspection of the χ^2 maps of these complex objects it became apparent that spiral structure could be present and significant enough to influence the fits even at this low level. Examples of the χ^2 masks used in both levels of refinement are shown in Fig. C3 for three representative objects.

This second level of refinement resulted in formally acceptable model fits for all but 14 objects. Residual image stamps of these 14 objects are shown in Fig. C4.

Throughout the analyses presented in this paper it is the parameters derived from the best-fitting refined models which have been utilized. For the 14 remaining unacceptable fits, we report the morphological properties from the second refinement in Table D2 with an asterisks marked in the column for the bulge effective radius in order to clearly distinguish them from the acceptable models. These 14 unacceptable models have been removed from all further results presented in Section 7 onwards so as not to potentially bias any science results.

The statistical quality of our final model fits is illustrated in Fig. C5, which shows the distribution of minimum χ^2 achieved from the modelling of the 69 'troublesome' galaxies in our sample both before and after the refinement in the model fitting as described above. The figure also shows the distribution of degrees of freedom for all objects, which is typically $\simeq$10 000 but varies on an object-by-object basis depending on the degree of object masking employed. As can be seen, our model fits have reduced χ^2 values centred exceptionally close to unity with very little spread (as detailed in the caption to Fig. C5, in practice equation C1 dictates that an acceptable model has to have typically $\chi^2 < 1.05 \times 10^4$ given the number of degrees of freedom involved in the fit).

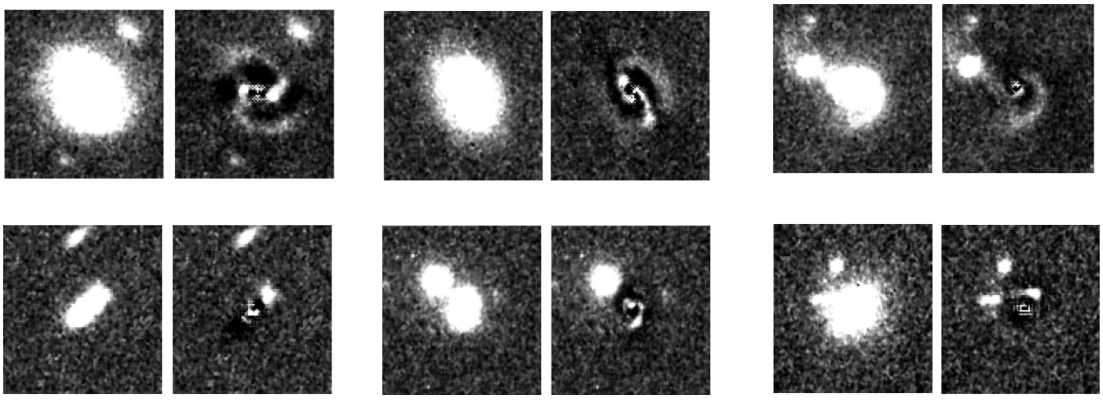

Figure C1. Six examples of objects where our initial modelling failed our χ^2 acceptability test due to additional structure which could not be properly accounted for by the smooth models. For each object we show the 6 × 6 arcsec image stamp on the left, and the data–model residual image on the right at the same grey-scale (as produced by the best-fitting double-component model). The top row shows some clear examples of spiral structures and interacting systems, whereas the bottom row shows objects where the fits have been influenced by close companions the light from which has not been adequately masked out.

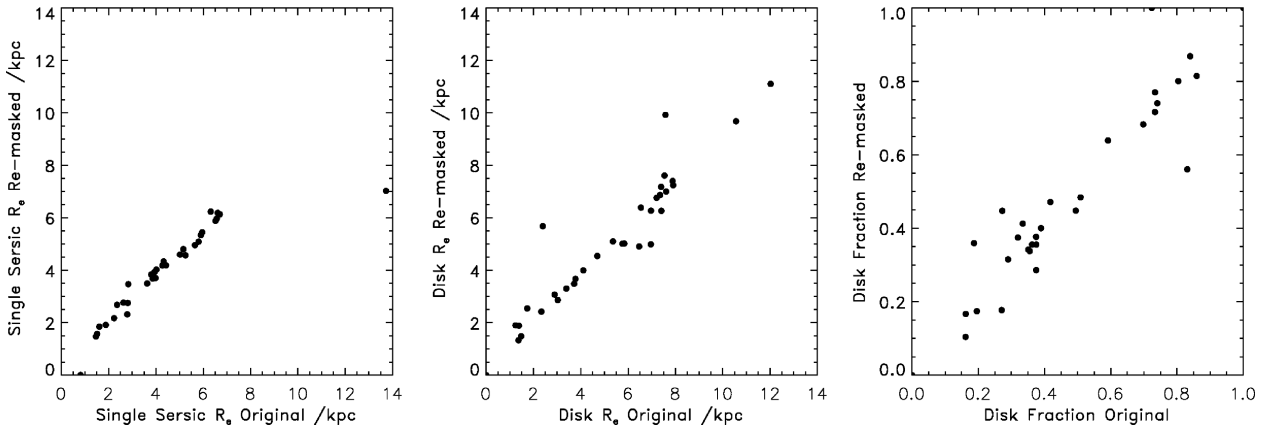

Figure C2. These plots demonstrate the excellent agreement between the key derived galaxy physical parameter values obtained with the original model-fitting and with the first set of re-masked/refined fits. Left: comparison between single-Sérsic model effective radii, middle: comparison between disc effective radii; right: comparison between disc fractions. These plots clearly illustrate that the underlying structure of these more complicated systems has in fact been accurately fitted by our procedure and has not been significantly influenced by the high surface brightness features, such as spiral arms, etc.

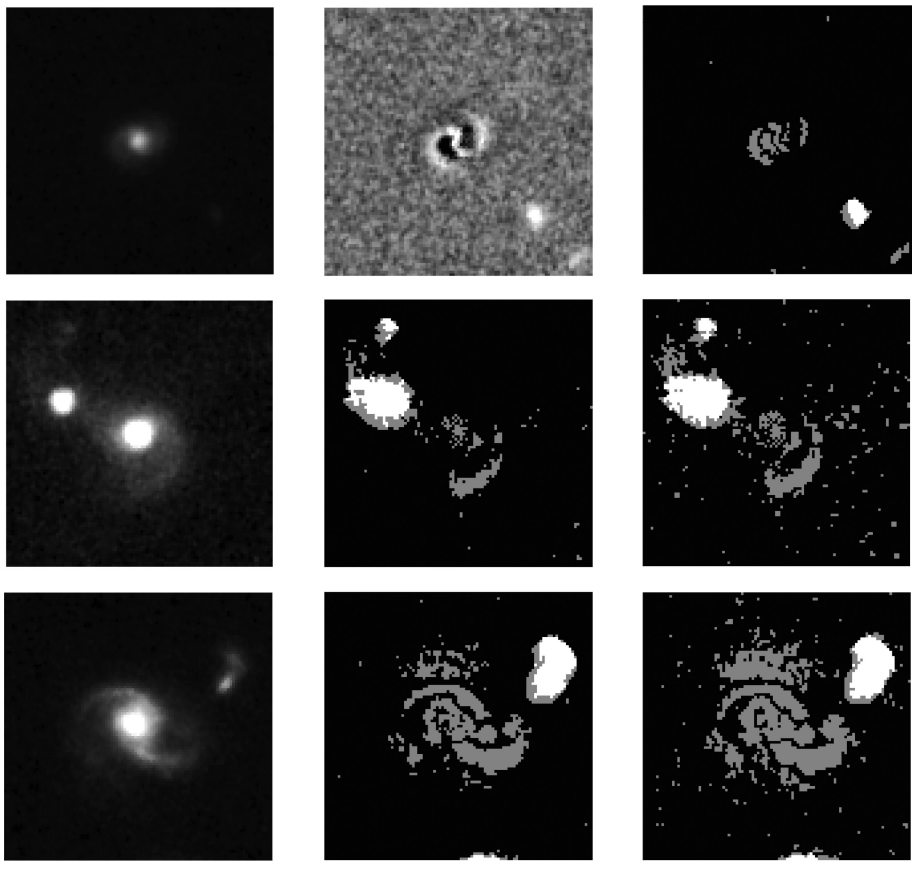

Figure C3. Examples of three objects where our initial modelling failed our χ^2 acceptability test due to additional structure, which were then re-fitted with masking of pixels for which the model fit to our data exceeded a certain χ^2 threshold. The top row is an example of an object for which we were able to achieve a statistically acceptable model fit after only one level of re-fitting, with masking based on our highest χ^2 threshold. The middle row shows an object where the additional lower χ^2 threshold masking was needed to achieve an acceptable fit, and the bottom row is one of the 14 objects which continued to fail the formal model-fitting acceptability criteria, even after both degrees of additional masking. The images displayed for the top row are the 6×6 arcsec image stamp on the left, the residual of our initial (non-χ^2-masked) fit in the middle and the χ^2 mask for the first degree of masking on the right. Whereas for the middle and bottom rows the images displayed are the 6×6 arcsec image stamp on the left, the χ^2 mask for the first degree of masking in the middle and the χ^2 mask for the second degree of masking on the right. The brightness levels of the χ^2 masks make the distinction between pixels which were masked out in all initial fits as being associated with companion objects identified by the segmentation maps (brighter pixels), and the additional levels of χ^2 masking in both cases of χ^2 thresholds (darker pixels).

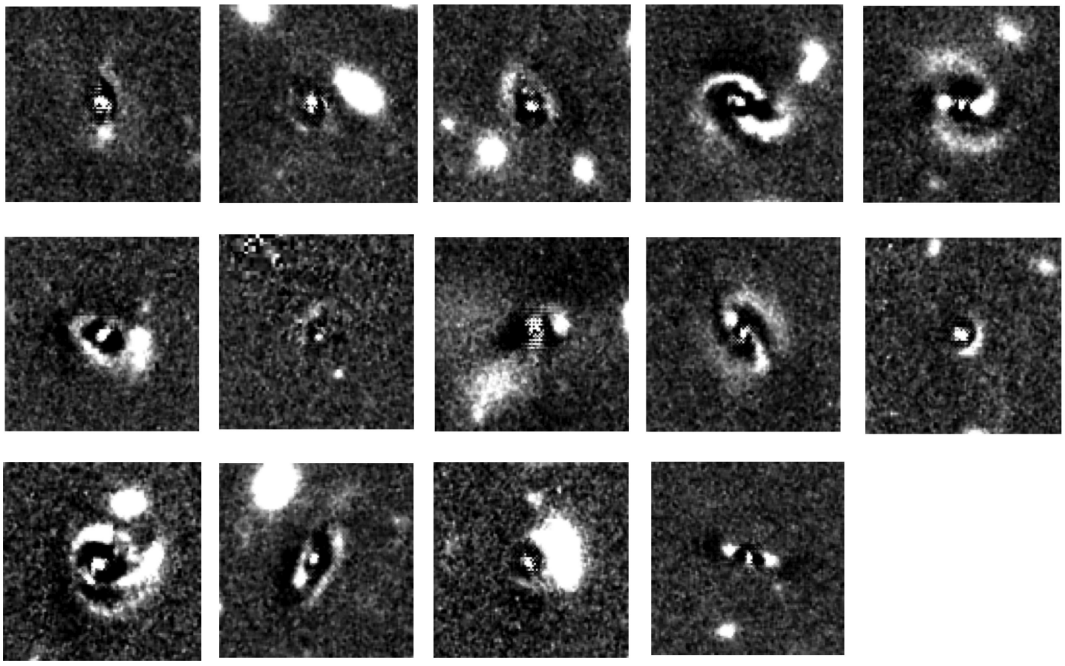

Figure C4. Residual map image stamps for the 14 objects which continued to fail the formal model-fitting acceptability criteria, even after additional masking. These image stamps have been constructed in the same way as in Fig. C1, with the same brightness level and pixel scale.

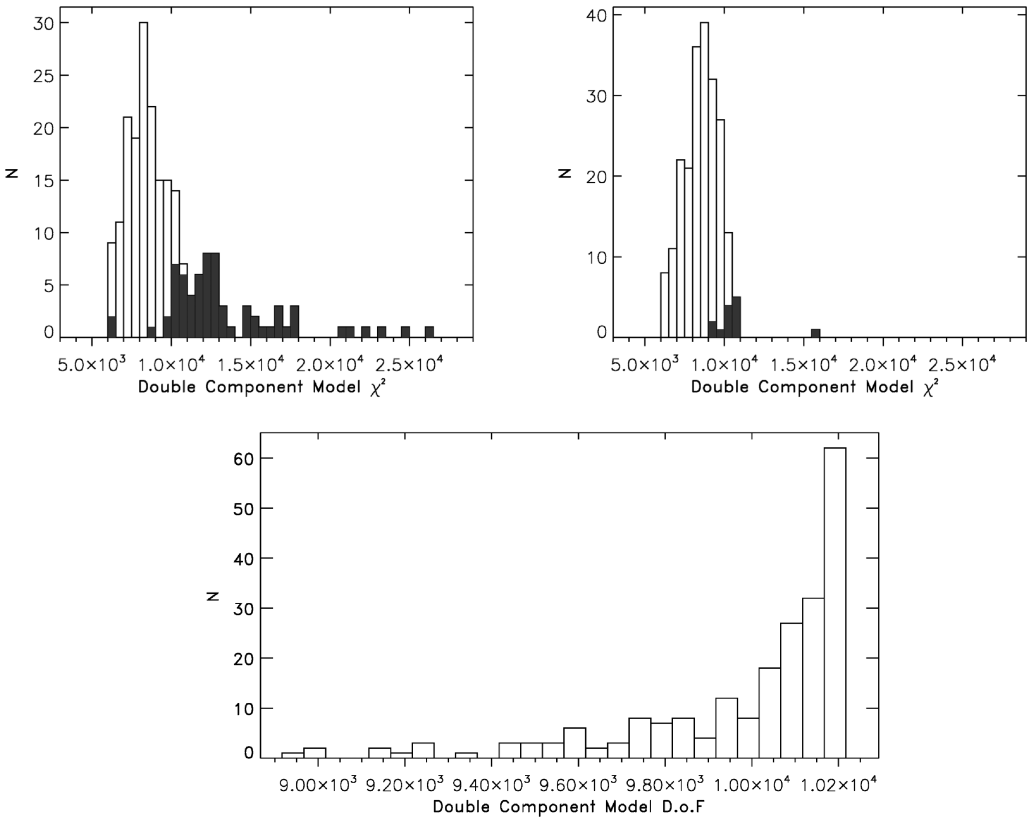

Figure C5. Distributions of minimum χ^2 achieved by the modelling of all objects in the sample. The upper-left panel shows this distribution as it resulted from the first pass of modelling, with the shaded region indicating those objects which failed to pass the acceptability criterion as defined in equation (C1), given the number of degrees of freedom (which is typical $\simeq$10 000, but varies on an object-by-object basis depending on the level of local pixel masking, as illustrated in the lower panel). The upper-right panel shows the final distribution achieved after the model refinement including additional pixel masking of high surface brightness features as described in the text. Here the remaining shaded region indicates the 14 objects for which we still failed to achieve an acceptable model fit (and whose residual images are shown in Fig. C4). In practice, equation (C1) means that a formally acceptable model has to typically have $\chi^2 < 1.05 \times 10^4$. As a result of the careful treatment given to modelling of all the objects in our sample, this have been achieved for 94 per cent of the galaxies studied here.

APPENDIX D: TABLES OF SAMPLE PROPERTIES AND BEST-FITTING PARAMETERS

Table D1. The physical properties of each object, listed by ascending redshift. We estimate errors on our total magnitudes of order ±0.05 mag, as our sample of galaxies are at the extreme bright end ($>10\sigma$) so their errors are limited to uncertainties in photometric zero-points. Errors on photometric redshifts are of the order of $\delta z/(1+z_{\rm spec}) = 0.05$, from Cirasuolo et al. (in preparation). Finally, we quote errors on our stellar mass estimates of a factor of 2 (Michałowski et al. 2012), where these are driven by uncertainties in the photometry from the IRAC bands and from photometric redshifts.

ID	RA	Dec.	H_{160} total magnitude	$z_{\rm phot}$	Mass/10^{11} $M_\odot$
			Galaxy properties		
104291	02:18:19.44	−05:14:45.9	20.78	1.00	1.17
107814	02:17:27.75	−05:13:30.3	20.68	1.00	1.02
110641	02:17:21.17	−05:12:24.0	19.90	1.00	1.91
117875	02:17:29.65	−05:09:47.6	20.51	1.00	1.62
104128	02:17:28.87	−05:14:48.8	20.20	1.02	1.17
109330	02:17:24.39	−05:12:52.2	19.17	1.02	4.47
120725	02:18:11.26	−05:08:49.5	20.75	1.02	1.29
121549	02:17:21.81	−05:08:23.2	20.44	1.02	1.58
121600	02:17:21.56	−05:08:28.8	21.44	1.02	1.05
107906	02:17:19.33	−05:13:25.6	20.63	1.05	1.32
115478	02:17:22.30	−05:10:38.5	20.29	1.05	2.24
107886	02:17:41.12	−05:13:30.8	20.63	1.07	1.38
111163	02:17:32.53	−05:12:18.0	20.84	1.07	1.51
116097	02:17:39.01	−05:10:32.3	21.39	1.07	1.15
116189	02:17:16.44	−05:10:28.2	20.17	1.07	1.95
117976	02:17:30.84	−05:09:43.8	20.13	1.07	2.24
108718	02:17:15.63	−05:13:07.7	20.37	1.10	1.66
109018	02:17:31.36	−05:13:04.4	21.01	1.10	1.15
105061	02:18:05.72	−05:14:33.8	20.61	1.15	1.55
116928	02:18:09.98	−05:10:08.9	20.05	1.15	3.09
117116	02:17:05.02	−05:10:07.1	20.43	1.15	1.82
120336	02:18:12.03	−05:08:56.8	20.73	1.15	1.07
102534	02:18:09.13	−05:15:30.2	20.06	1.17	1.07
103000	02:18:15.05	−05:15:20.6	20.11	1.17	3.09
108988	02:18:13.70	−05:13:06.4	20.50	1.17	1.35
113554	02:17:06.12	−05:11:23.0	20.91	1.17	1.26
102857	02:17:04.77	−05:15:18.1	19.97	1.20	3.80
113491	02:17:06.45	−05:11:23.1	20.14	1.20	2.95
116852	02:17:17.49	−05:10:03.3	19.87	1.20	1.48
118791	02:17:41.09	−05:09:26.3	20.17	1.20	3.24
104282	02:17:43.91	−05:14:50.7	21.93	1.25	1.02
120093	02:17:13.51	−05:09:03.2	21.43	1.25	1.20
120134	02:18:07.80	−05:09:00.9	21.75	1.27	1.20
112575	02:17:15.55	−05:11:47.9	21.58	1.30	1.07
105017	02:18:06.10	−05:14:33.7	21.03	1.32	1.23
109704	02:18:06.16	−05:12:44.9	20.23	1.32	1.32
113419	02:17:05.68	−05:11:31.6	20.70	1.32	1.58
113972	02:17:40.35	−05:11:16.8	20.77	1.35	1.45
122843	02:18:16.99	−05:07:55.7	21.20	1.35	1.55
102704	02:18:20.21	−05:15:30.5	21.52	1.37	1.00
104371	02:17:30.82	−05:14:47.5	21.03	1.37	1.41
113151	02:17:15.83	−05:11:37.2	20.67	1.37	1.70
107026	02:17:12.46	−05:13:48.5	21.14	1.40	1.70
107210	02:17:17.69	−05:13:47.3	21.53	1.40	1.74
100222	02:17:51.22	−05:16:21.8	19.79	1.42	4.68
107573	02:18:07.15	−05:13:39.8	21.57	1.42	1.45
119019	02:17:46.64	−05:09:26.3	21.06	1.42	1.48
102613	02:17:38.51	−05:15:33.3	21.64	1.45	1.20
104240	02:17:55.30	−05:14:52.1	21.53	1.45	1.07
105024	02:17:17.95	−05:14:34.1	21.58	1.45	1.23

Table D1 – *continued*

ID	RA	Dec.	H_{160} total magnitude	$z_{\rm phot}$	Mass/10^{11} $M_{\odot}$
112384	02:17:01.03	−05:11:54.3	21.60	1.45	1.17
114942	02:17:55.53	−05:10:54.0	20.28	1.45	1.45
122919	02:18:20.92	−05:07:59.2	21.02	1.45	2.34
105818	02:17:48.93	−05:14:19.0	22.56	1.47	1.51
118545	02:17:47.44	−05:09:35.7	20.68	1.47	2.45
112149	02:16:54.03	−05:11:59.2	21.83	1.50	1.00
110670	02:18:01.56	−05:12:30.6	21.53	1.52	1.35
100855	02:16:56.99	−05:16:13.6	20.84	1.55	2.63
111783	02:17:20.48	−05:12:06.1	20.99	1.55	2.34
118417	02:17:35.31	−05:09:43.6	22.10	1.55	1.78
123058	02:17:22.66	−05:07:56.8	21.45	1.55	1.20
109795	02:16:59.40	−05:12:50.7	21.77	1.57	2.45
110261	02:17:23.83	−05:12:39.3	21.62	1.57	1.38
121157	02:17:31.87	−05:08:37.1	20.47	1.57	5.25
102712	02:17:56.97	−05:15:31.8	21.04	1.60	1.20
121682	02:17:08.19	−05:08:25.5	21.52	1.60	1.86
102967	02:17:19.38	−05:15:10.6	20.58	1.62	2.82
117838	02:17:25.02	−05:09:52.4	21.38	1.62	1.66
118244	02:17:13.62	−05:09:39.8	20.63	1.62	2.51
113309	02:17:07.58	−05:11:33.0	22.02	1.65	1.74
115725	02:18:21.09	−05:10:33.0	20.52	1.65	3.39
116275	02:18:10.69	−05:10:29.5	21.39	1.65	1.10
121585	02:17:08.63	−05:08:26.1	20.94	1.65	2.88
101385	02:18:11.91	−05:16:04.3	21.78	1.67	1.10
109022	02:17:47.08	−05:13:05.3	21.73	1.67	1.48
110839	02:17:53.86	−05:12:26.0	21.09	1.67	1.35
113066	02:17:47.22	−05:11:38.6	21.45	1.67	1.29
105503	02:18:04.97	−05:14:24.6	21.94	1.70	1.48
105929	02:17:16.44	−05:14:14.6	21.40	1.70	1.12
110901	02:17:23.65	−05:12:24.9	21.84	1.70	1.15
113549	02:17:58.64	−05:11:32.4	22.49	1.70	1.12
117922	02:18:17.10	−05:09:52.6	21.63	1.70	1.45
119123	02:18:18.96	−05:09:24.9	21.53	1.70	1.86
120201	02:17:58.08	−05:09:01.7	21.63	1.70	1.51
100592	02:17:19.34	−05:16:22.3	21.96	1.72	1.05
111966	02:17:47.26	−05:12:02.5	21.17	1.72	2.45
115630	02:17:35.41	−05:10:42.9	21.54	1.72	1.58
116508	02:18:21.54	−05:10:19.8	20.71	1.72	3.55
120574	02:18:14.44	−05:08:51.1	21.24	1.72	2.24
120940	02:17:15.07	−05:08:40.5	20.76	1.72	2.40
121595	02:17:11.97	−05:08:23.2	20.64	1.72	2.51
104918	02:17:15.54	−05:14:35.7	20.95	1.75	2.82
110317	02:16:53.99	−05:12:39.8	21.63	1.75	1.26
114574	02:18:17.20	−05:11:05.7	21.42	1.75	1.41
115661	02:17:52.70	−05:10:42.9	21.63	1.75	1.74
117377	02:18:17.61	−05:10:04.1	21.05	1.75	3.24
101558	02:17:35.20	−05:15:57.7	21.40	1.77	1.38
102867	02:17:33.59	−05:15:28.7	21.81	1.77	1.58
110152	02:17:33.37	−05:12:41.4	20.71	1.77	1.15
113470	02:17:29.40	−05:11:29.6	20.86	1.77	1.48
117047	02:18:19.32	−05:10:13.4	21.99	1.77	1.20
117332	02:18:10.51	−05:10:06.9	22.17	1.77	1.41
122623	02:17:46.36	−05:08:03.9	21.40	1.77	1.62
103252	02:17:36.13	−05:15:20.0	21.90	1.80	1.02
106944	02:18:14.05	−05:13:54.7	22.07	1.80	1.32
113302	02:17:14.07	−05:11:34.2	21.48	1.80	1.17
117258	02:17:33.50	−05:10:05.1	21.36	1.80	1.95
119091	02:17:51.06	−05:09:26.1	21.77	1.80	1.07
121062	02:17:37.41	−05:08:41.5	21.69	1.80	2.14
109905	02:18:10.75	−05:12:43.2	21.85	1.82	1.51
110645	02:18:11.78	−05:12:30.5	21.01	1.82	3.72
114669	02:17:13.84	−05:11:06.2	22.26	1.82	1.32

Table D1 – *continued*

ID	RA	Dec.	H_{160} total magnitude	$z_{\rm phot}$	Mass/10^{11} $M_\odot$
115841	02:18:19.29	−05:10:38.8	22.12	1.82	1.02
117884	02:17:37.16	−05:09:53.9	21.74	1.82	2.34
120014	02:17:21.57	−05:08:58.7	21.13	1.85	1.74
100741	02:17:25.11	−05:16:17.8	22.27	1.87	1.10
104404	02:17:55.36	−05:14:51.2	22.35	1.87	1.29
105238	02:17:54.64	−05:14:30.5	22.03	1.87	1.62
118954	02:17:48.86	−05:09:32.1	21.75	1.90	1.86
102297	02:17:23.47	−05:15:40.3	21.71	1.97	1.48
106298	02:18:08.72	−05:14:09.9	21.95	1.97	1.66
110734	02:17:05.00	−05:12:28.3	22.76	1.97	1.95
120314	02:17:20.29	−05:09:00.2	22.34	1.97	1.41
120345	02:17:20.77	−05:08:56.4	21.68	1.97	1.17
107080	02:17:17.43	−05:13:48.1	22.46	2.00	1.17
121825	02:18:03.95	−05:08:25.9	22.45	2.00	1.00
123330	02:17:46.90	−05:07:49.8	22.67	2.00	1.29
123457	02:17:04.19	−05:07:46.7	23.23	2.00	1.02
100934	02:17:39.09	−05:16:12.9	22.00	2.02	1.15
107453	02:18:05.43	−05:13:43.3	21.78	2.02	1.51
111656	02:17:14.06	−05:12:09.4	22.91	2.02	1.15
113744	02:18:16.84	−05:11:27.7	22.76	2.02	1.00
115054	02:17:52.44	−05:10:56.6	22.95	2.02	2.09
119667	02:17:56.45	−05:09:15.1	23.55	2.02	1.35
119944	02:17:04.63	−05:09:06.3	22.05	2.02	1.45
120268	02:17:19.69	−05:08:56.6	21.86	2.02	2.34
120920	02:17:55.69	−05:08:37.2	21.41	2.02	1.70
102986	02:17:50.41	−05:15:27.2	22.91	2.05	1.10
109891	02:18:09.54	−05:12:49.5	22.40	2.05	1.05
111030	02:17:31.66	−05:12:24.2	22.93	2.05	1.51
111336	02:18:03.03	−05:12:17.9	22.17	2.05	1.17
114933	02:17:26.10	−05:10:58.2	21.78	2.05	1.58
116891	02:17:39.79	−05:10:18.7	23.48	2.05	1.12
118757	02:17:05.22	−05:09:36.2	23.17	2.05	1.10
122721	02:17:51.33	−05:08:03.4	22.81	2.05	1.26
103749	02:17:04.68	−05:15:09.7	23.29	2.07	1.17
103751	02:17:21.88	−05:15:08.1	22.03	2.07	1.29
107730	02:17:06.71	−05:13:38.3	22.22	2.07	1.41
111461	02:17:57.64	−05:12:14.4	22.44	2.07	1.38
111782	02:17:50.68	−05:12:04.6	22.31	2.07	1.00
119679	02:18:06.56	−05:09:15.4	22.52	2.07	1.00
123325	02:17:24.79	−05:07:51.3	22.44	2.07	1.02
100894	02:17:42.33	−05:16:15.5	23.02	2.10	1.07
107689	02:17:06.93	−05:13:35.9	21.78	2.10	2.04
108249	02:18:07.84	−05:13:25.1	22.45	2.10	1.07
108777	02:17:20.80	−05:13:16.0	23.63	2.10	1.32
115620	02:18:21.31	−05:10:44.0	22.23	2.10	1.48
117347	02:17:13.48	−05:10:05.6	22.66	2.10	1.38
121641	02:17:40.41	−05:08:30.3	22.72	2.10	1.05
100858	02:17:30.39	−05:16:16.6	23.96	2.12	1.55
102168	02:17:05.60	−05:15:43.5	21.20	2.12	2.63
104794	02:17:19.60	−05:14:43.0	23.11	2.12	1.12
110029	02:17:41.59	−05:12:46.6	23.15	2.12	1.12
116835	02:17:31.35	−05:10:18.3	22.05	2.12	1.66
119583	02:17:07.61	−05:09:17.5	23.25	2.12	1.35
121896	02:18:03.20	−05:08:23.1	22.17	2.12	1.51
109051	02:17:20.02	−05:13:05.7	22.66	2.15	2.34
112374	02:17:32.56	−05:11:56.3	23.06	2.15	1.02
114727	02:17:21.18	−05:11:02.7	21.81	2.15	3.72
102387	02:18:03.40	−05:15:41.3	22.25	2.17	1.48
110626	02:17:04.97	−05:12:31.4	22.38	2.17	1.20
116591	02:17:35.58	−05:10:23.1	22.01	2.17	2.14

Table D1 – *continued*

ID	RA	Dec.	H_{160} total magnitude	z_{phot}	Mass/10^{11} $M_\odot$
116644	02:16:55.05	−05:10:22.8	22.27	2.17	1.38
101298	02:17:19.82	−05:16:04.5	23.12	2.20	1.02
108854	02:17:12.54	−05:13:09.2	22.39	2.20	1.45
111731	02:17:27.41	−05:12:08.0	22.05	2.20	1.02
109877	02:17:11.07	−05:12:49.1	22.32	2.22	1.17
111146	02:17:07.97	−05:12:21.6	22.58	2.22	1.41
111909	02:17:27.16	−05:11:57.7	21.18	2.22	2.40
123324	02:17:43.95	−05:07:51.3	23.12	2.22	1.58
107752	02:18:08.19	−05:13:38.4	22.09	2.25	1.10
111836	02:17:41.80	−05:12:06.7	23.09	2.25	1.38
119585	02:17:42.89	−05:09:17.9	22.71	2.25	1.32
103664	02:17:57.56	−05:15:08.6	22.46	2.27	2.51
107610	02:17:13.69	−05:13:41.3	22.54	2.27	1.45
100564	02:17:25.97	−05:16:21.3	21.79	2.30	2.69
101313	02:17:24.85	−05:16:06.3	22.91	2.30	1.38
101818	02:17:44.98	−05:15:51.0	22.10	2.30	1.45
109082	02:17:37.39	−05:13:07.9	22.44	2.30	1.86
109262	02:18:11.09	−05:13:04.4	22.81	2.30	1.35
114138	02:18:11.78	−05:11:15.9	22.21	2.30	1.41
104698	02:17:17.29	−05:14:44.6	22.94	2.32	1.55
101714	02:17:37.25	−05:15:49.6	22.30	2.35	1.86
103841	02:17:51.76	−05:15:07.0	24.27	2.35	2.57
108887	02:16:55.80	−05:13:12.7	22.50	2.35	1.95
108892	02:17:18.39	−05:13:10.7	22.48	2.35	1.74
115739	02:17:56.02	−05:10:43.3	24.37	2.35	1.00
113904	02:17:03.66	−05:11:22.2	22.57	2.40	1.00
121971	02:16:57.46	−05:08:23.1	22.50	2.40	2.82
110871	02:17:25.20	−05:12:29.7	24.03	2.43	1.05
108716	02:17:41.32	−05:13:14.6	23.36	2.48	1.15
104392	02:17:43.16	−05:14:51.3	23.66	2.50	1.26
121395	02:17:20.95	−05:08:37.1	22.95	2.50	2.34
117233	02:17:35.90	−05:10:09.4	22.91	2.55	1.86
120369	02:18:17.17	−05:08:59.4	21.88	2.55	2.09
114460	02:17:34.76	−05:11:11.1	23.35	2.58	1.32
115338	02:17:41.37	−05:10:51.8	23.86	2.58	1.74
101548	02:16:54.85	−05:16:01.1	23.38	2.60	1.32
110846	02:18:21.40	−05:12:29.2	22.56	2.60	1.35
101885	02:17:09.17	−05:15:45.4	22.63	2.63	1.26
106767	02:17:01.41	−05:14:01.8	24.16	2.63	3.24
116142	02:17:13.11	−05:10:32.5	22.39	2.65	2.14
110731	02:18:04.64	−05:12:32.3	22.96	2.78	1.15
122586	02:18:06.38	−05:08:09.7	22.77	2.98	3.72
107762	02:17:05.79	−05:13:38.5	23.46	3.00	1.07

Table D2. The fitted parameters for each object. Objects with an unacceptable single component model have been flagged with an asterisks in the Sérsic index column, while objects with unacceptable double component models are flagged similarly in the bulge effective radius column. Obtaining individual uncertainties for all the parameters of multiple-component fits listed here is impractical as the degree of systematic and correlated errors varies on an object-by-object basis. However, from the detailed parameter space search conducted for our single-Sérsic models, we determined errors of the order of 10 per cent for effective radii and 5 per cent for Sérsic indices, with errors being somewhat smaller for better constrained parameters such as axial ratios. Therefore, we estimate that the multiple-component errors will be a factor of $\sqrt{2}$ larger, giving errors on fitted parameters up to 15 per cent. However, we note that in the case of weak secondary components the errors can potentially be much larger, but as our science plots use only parameters from significant components the errors should be similar to those of the single component models.

ID	n	r_e (kpc)	Axial ratio	PSF (per cent)	Bulge r_e (kpc)	Disc r_e (kpc)	Bulge axial ratio	Disc axial ratio	Bulge (per cent)	Disc (per cent)	PSF (per cent)
					Best-fitting parameters						
104291	2.7	3.8	0.5	0.0	4.6	3.3	0.57	0.45	74.0	26.0	0.0
107814	0.8 *	6.2	0.5	0.0	−*	6.4	–	0.49	0.0	100.0	0.0

Table D2 – *continued*

ID	n	r_e (kpc)	Axial ratio	PSF (per cent)	Bulge r_e (kpc)	Disc r_e (kpc)	Bulge axial ratio	Disc axial ratio	Bulge (per cent)	Disc (per cent)	PSF (per cent)
110641	2.8 *	5.2	0.6	0.0	3.5 *	6.7	0.43	0.93	64.0	36.0	0.0
117875	11.7 *	3.8	0.6	0.0	1.2	12.0	0.42	0.70	83.0	17.0	0.0
104128	1.2	4.2	0.5	15.0	0.8	4.5	0.28	0.56	28.0	72.0	0.0
109330	5.7 *	7.1	0.6	0.0	7.1 *	–	0.64	–	87.0	0.0	13.0
120725	1.9	2.9	0.4	0.0	5.2	2.6	0.47	0.33	45.0	55.0	0.0
121549	7.0	4.0	0.7	0.0	6.2	1.1	0.62	0.69	68.0	20.0	12.0
121600	4.6	1.5	0.7	0.0	1.4	–	0.66	–	100.0	0.0	0.0
107906	3.5	2.3	0.5	0.0	2.5	2.0	0.55	0.27	86.0	14.0	0.0
115478	2.7 *	5.3	0.5	0.0	3.7 *	7.4	0.31	0.60	65.0	35.0	0.0
107886	3.4 *	1.6	0.5	0.0	2.6	1.9	0.61	0.26	50.0	35.0	15.0
111163	1.4	2.5	0.8	12.0	8.6	2.6	0.68	0.69	11.0	73.0	16.0
116097	1.4	3.0	0.7	0.0	1.1	3.6	0.30	0.67	17.0	83.0	0.0
116189	0.8	3.9	0.6	42.0	0.2	3.8	0.24	0.64	40.0	60.0	0.0
117976	3.4	2.8	0.8	0.0	2.3	5.4	0.75	0.63	82.0	18.0	0.0
108718	3.7	4.8	0.4	0.0	8.7	2.9	0.55	0.17	62.0	38.0	0.0
109018	2.7	2.9	0.5	19.0	0.9	6.2	0.59	0.37	70.0	30.0	0.0
105061	2.4 *	3.3	0.5	27.0	0.7 *	5.2	0.48	0.47	62.0	38.0	0.0
116928	4.5	1.8	0.9	0.0	1.7	–	0.94	–	100.0	0.0	0.0
117116	4.2	4.2	0.9	0.0	4.0	–	0.87	–	100.0	0.0	0.0
120336	1.1	3.7	0.8	0.0	–	3.7	–	0.75	0.0	100.0	0.0
102534	1.3 *	5.8	0.9	0.0	0.9 *	6.2	0.34	0.88	11.0	89.0	0.0
103000	1.8	4.4	1.0	11.0	1.2	5.4	0.98	0.99	39.0	61.0	0.0
108988	2.3	2.8	0.8	31.0	0.6	4.7	0.78	0.76	68.0	32.0	0.0
113554	1.8	2.7	0.3	22.0	1.6	3.4	0.46	0.22	53.0	35.0	12.0
102857	3.9	4.1	0.9	0.0	4.1	–	0.95	–	100.0	0.0	0.0
113491	3.5	4.9	0.8	0.0	3.7	9.2	0.92	0.50	84.0	16.0	0.0
116852	3.1 *	3.9	0.7	0.0	3.1 *	6.7	0.76	0.59	82.0	18.0	0.0
118791	3.2 *	4.6	0.5	0.0	3.1 *	7.1	0.40	0.54	72.0	28.0	0.0
104282	5.2	2.3	0.6	0.0	1.3	7.0	0.44	0.64	76.0	24.0	0.0
120093	0.4	5.2	0.3	17.0	–*	5.1	–	0.32	0.0	88.0	12.0
120134	0.7	6.5	0.4	0.0	–	7.0	–	0.36	0.0	100.0	0.0
112575	2.0	1.6	0.7	18.0	3.3	1.7	0.88	0.54	23.0	53.0	24.0
105017	4.5	2.6	1.0	0.0	1.4	5.4	0.90	0.90	72.0	28.0	0.0
109704	3.2	5.2	0.7	0.0	5.1	6.1	0.81	0.42	81.0	19.0	0.0
113419	1.8	2.4	0.7	11.0	1.2	3.1	0.65	0.62	57.0	43.0	0.0
113972	1.9	2.0	0.8	0.0	2.3	2.3	0.80	0.54	47.0	53.0	0.0
122843	2.3 *	7.1	0.6	0.0	7.0	5.9	0.27	0.92	44.0	56.0	0.0
102704	2.4	4.5	0.3	0.0	1.4	5.9	0.65	0.20	36.0	64.0	0.0
104371	1.2	1.9	0.7	15.0	0.8	2.2	0.78	0.60	46.0	54.0	0.0
113151	1.0	3.1	0.8	17.0	–	3.1	–	0.77	0.0	83.0	17.0
107026	3.5	3.2	0.8	0.0	2.9	5.6	0.85	0.59	88.0	12.0	0.0
107210	1.8	2.0	0.5	0.0	1.6	2.4	0.87	0.41	44.0	56.0	0.0
100222	2.3	2.2	0.5	0.0	2.4	2.5	0.58	0.43	60.0	40.0	0.0
107573	1.0	4.1	0.6	0.0	–	4.1	–	0.60	0.0	100.0	0.0
119019	1.7	3.0	0.2	22.0	0.9	4.4	0.26	0.17	59.0	41.0	0.0
102613	4.6	1.1	0.7	0.0	2.0	0.7	0.87	0.40	64.0	36.0	0.0
104240	1.2	3.4	0.8	0.0	12.4	3.5	0.47	0.67	17.0	83.0	0.0
105024	3.5	1.5	0.8	0.0	2.2	1.3	0.93	0.32	67.0	33.0	0.0
112384	3.5	1.7	1.0	0.0	1.7	3.2	0.89	0.50	90.0	10.0	0.0
114942	1.6 *	5.0	0.8	0.0	10.0 *	5.2	0.56	0.67	36.0	64.0	0.0
122919	0.9	4.8	0.5	14.0	–	4.8	–	0.54	0.0	87.0	13.0
105818	2.8	2.3	0.6	13.0	1.1	4.3	0.56	0.64	74.0	26.0	0.0
118545	2.8	3.2	0.7	16.0	1.5	6.0	0.64	0.72	79.0	21.0	0.0
112149	4.8	1.2	0.6	0.0	1.2	–	0.56	–	100.0	0.0	0.0
110670	3.2	2.1	0.8	0.0	1.3	4.3	0.78	0.50	66.0	34.0	0.0
100855	3.2	2.1	0.5	0.0	2.4	2.0	0.44	0.36	81.0	19.0	0.0
111783	3.1	2.1	0.6	12.0	1.1	4.4	0.46	0.72	77.0	23.0	0.0
118417	1.8	1.9	0.6	0.0	1.4	2.4	0.65	0.50	39.0	61.0	0.0
123058	3.2	0.7	0.9	0.0	0.4	2.3	0.84	0.64	78.0	22.0	0.0

Table D2 – *continued*

ID	n	r_e (kpc)	Axial ratio	PSF (per cent)	Bulge r_e (kpc)	Disc r_e (kpc)	Bulge axial ratio	Disc axial ratio	Bulge (per cent)	Disc (per cent)	PSF (per cent)
109795	0.8	4.2	0.6	0.0	–	4.2	–	0.57	0.0	100.0	0.0
110261	3.7	1.3	0.7	0.0	1.4	–	0.69	–	100.0	0.0	0.0
121157	1.9 *	6.1	0.3	0.0	6.4	6.7	0.39	0.23	46.0	54.0	0.0
102712	2.1	1.5	0.6	22.0	1.0	2.0	0.71	0.41	51.0	31.0	19.0
121682	3.2	4.4	0.7	0.0	4.2	6.1	0.73	0.35	82.0	18.0	0.0
102967	3.7	3.7	0.6	0.0	1.8	7.1	0.61	0.53	66.0	34.0	0.0
117838	1.9	3.6	0.3	15.0	1.6	5.0	0.23	0.36	60.0	40.0	0.0
118244	1.6 *	3.9	0.7	17.0	1.5 *	4.9	0.70	0.71	52.0	48.0	0.0
113309	3.6	5.1	0.4	0.0	9.2	1.8	0.36	0.56	70.0	30.0	0.0
115725	2.4	3.3	0.5	0.0	2.4	4.7	0.48	0.37	59.0	41.0	0.0
116275	2.5	1.0	0.7	0.0	1.2	1.0	0.91	0.54	59.0	41.0	0.0
121585	1.9	2.8	0.6	17.0	0.7	4.2	0.90	0.43	56.0	44.0	0.0
101385	0.8	1.4	0.6	24.0	–	1.3	–	0.58	0.0	80.0	20.0
109022	4.1	3.8	0.6	0.0	3.8	–	0.63	–	100.0	0.0	0.0
110839	1.2	5.2	0.6	11.0	0.4	5.4	0.11	0.58	16.0	84.0	0.0
113066	2.6	1.9	0.8	0.0	3.9	1.4	0.80	0.84	54.0	46.0	0.0
105503	1.9	2.2	0.7	0.0	2.5	2.3	0.48	0.70	47.0	53.0	0.0
105929	1.1 *	2.7	0.8	22.0	–*	2.8	–	0.83	0.0	76.0	24.0
110901	1.3	4.7	0.5	14.0	0.6	5.2	0.43	0.51	26.0	74.0	0.0
113549	1.7	1.3	0.5	0.0	0.6	1.6	0.42	0.36	28.0	72.0	0.0
117922	2.4	2.2	0.9	0.0	1.2	3.2	0.72	0.74	42.0	58.0	0.0
119123	4.1	3.5	0.9	0.0	2.7	6.8	0.89	0.78	85.0	15.0	0.0
120201	3.0	2.0	0.6	0.0	2.2	2.3	0.63	0.34	80.0	20.0	0.0
100592	2.1	1.1	0.3	0.0	0.9	1.4	0.43	0.16	56.0	44.0	0.0
111966	1.7	1.9	0.4	14.0	0.8	2.6	0.34	0.35	53.0	47.0	0.0
115630	3.9	1.4	0.4	0.0	3.8	1.7	0.60	0.21	38.0	42.0	20.0
116508	3.1	5.4	0.7	16.0	1.7	7.7	0.62	0.91	68.0	32.0	0.0
120574	2.0	5.8	0.3	0.0	1.6	6.6	0.20	0.37	24.0	76.0	0.0
120940	1.4 *	6.1	0.7	0.0	2.3	7.0	0.59	0.62	18.0	82.0	0.0
121595	2.4	4.0	0.6	10.0	1.8	5.2	0.44	0.78	58.0	42.0	0.0
104918	1.2	4.0	0.7	26.0	0.4	4.5	0.44	0.64	37.0	63.0	0.0
110317	2.5	2.2	0.6	0.0	1.2	3.1	0.35	0.69	45.0	55.0	0.0
114574	1.7	2.4	0.7	0.0	–	2.7	–	0.71	0.0	88.0	12.0
115661	3.7	1.0	0.8	0.0	1.3	0.7	0.76	0.76	78.0	22.0	0.0
117377	2.1	2.3	0.2	18.0	0.9	3.6	0.35	0.16	68.0	32.0	0.0
101558	0.9	4.9	0.9	16.0	–	4.9	–	0.87	0.0	85.0	15.0
102867	2.5	1.9	0.9	14.0	0.7	3.7	0.57	0.61	57.0	43.0	0.0
110152	1.3 *	5.0	0.7	0.0	0.8 *	5.6	0.15	0.69	13.0	87.0	0.0
113470	0.9	4.8	0.9	12.0	1.3	4.9	0.22	0.94	21.0	79.0	0.0
117047	1.5	1.9	0.2	0.0	–	1.9	–	0.22	0.0	100.0	0.0
117332	2.4	2.4	0.4	0.0	3.2	2.2	0.64	0.19	59.0	41.0	0.0
122623	2.3	2.4	1.0	0.0	1.9	3.5	0.71	0.80	56.0	44.0	0.0
103252	0.7	4.1	0.3	0.0	–	4.1	–	0.34	0.0	100.0	0.0
106944	3.2	2.6	0.8	0.0	1.5	4.1	0.59	0.83	56.0	44.0	0.0
113302	11.6	2.9	0.7	14.0	0.8	11.4	0.70	0.60	85.0	15.0	0.0
117258	3.3	1.5	0.8	0.0	2.0	1.6	0.65	0.36	80.0	20.0	0.0
119091	3.5	5.0	0.5	0.0	2.7	5.5	0.29	0.98	56.0	44.0	0.0
121062	4.8	1.7	1.0	0.0	2.8	1.5	0.79	0.41	72.0	18.0	10.0
109905	2.4	1.6	0.7	0.0	1.3	2.1	0.87	0.55	63.0	37.0	0.0
110645	2.1	3.1	0.7	12.0	1.3	4.4	0.69	0.72	56.0	44.0	0.0
114669	1.4	1.6	0.3	12.0	0.4	2.0	0.47	0.23	36.0	64.0	0.0
115841	3.9	1.1	0.7	0.0	1.1	–	0.73	–	100.0	0.0	0.0
117884	1.3	2.8	0.8	25.0	0.4	3.3	0.50	0.80	39.0	61.0	0.0
120014	7.6	9.9	0.8	0.0	1.8	10.9	0.69	0.74	68.0	32.0	0.0
100741	1.7	2.7	0.5	0.0	–	2.5	–	0.52	0.0	100.0	0.0
104404	6.3	10.4	0.9	0.0	5.3	–	0.91	–	100.0	0.0	0.0
105238	1.9	3.1	0.7	0.0	5.2	2.8	0.55	0.69	49.0	51.0	0.0
118954	1.8	1.0	0.4	0.0	1.0	1.1	0.46	0.38	37.0	63.0	0.0
102297	2.7	2.7	0.8	0.0	5.2	2.1	0.71	0.43	67.0	33.0	0.0
106298	1.1	2.1	0.9	17.0	–	2.2	–	0.86	0.0	82.0	18.0

Table D2 – *continued*

ID	n	r_e (kpc)	Axial ratio	PSF (per cent)	Bulge r_e (kpc)	Disc r_e (kpc)	Bulge axial ratio	Disc axial ratio	Bulge (per cent)	Disc (per cent)	PSF (per cent)
110734	5.1	17.1	0.4	0.0	11.5	–	0.42	–	100.0	0.0	0.0
120314	4.2	1.1	0.8	0.0	1.1	–	0.82	–	100.0	0.0	0.0
120345	4.9	1.9	0.8	0.0	2.3	0.6	0.85	0.06	87.0	13.0	0.0
107080	0.9	3.8	0.9	17.0	0.4	4.0	0.36	0.85	21.0	79.0	0.0
121825	3.5	2.4	1.0	0.0	1.2	4.0	0.84	0.89	60.0	40.0	0.0
123330	1.2	4.8	0.5	0.0	–	4.6	–	0.51	0.0	100.0	0.0
123457	0.6	4.7	0.6	0.0	–	5.0	–	0.65	0.0	100.0	0.0
100934	15.3	6.3	0.5	0.0	1.3	10.5	0.30	0.47	63.0	25.0	12.0
107453	0.8	3.2	0.7	23.0	–	3.2	–	0.68	0.0	79.0	21.0
111656	8.4	2.6	0.5	0.0	2.5	–	0.50	–	86.0	0.0	14.0
113744	2.1	1.0	0.3	0.0	0.6	1.4	0.46	0.07	49.0	51.0	0.0
115054	1.3	4.4	0.8	17.0	0.4	5.1	0.48	0.74	27.0	73.0	0.0
119667	1.6	4.2	0.5	0.0	–	3.7	–	0.50	0.0	100.0	0.0
119944	1.0	5.4	0.7	0.0	–	5.5	–	0.70	0.0	100.0	0.0
120268	2.7	8.0	0.4	0.0	4.5	8.3	0.16	0.48	42.0	58.0	0.0
120920	4.6	2.3	0.8	0.0	1.4	5.9	0.87	0.69	81.0	19.0	0.0
102986	5.8	1.8	0.8	0.0	0.9	6.3	0.73	0.72	74.0	26.0	0.0
109891	8.7	2.3	0.7	0.0	4.6	0.5	0.65	0.67	63.0	37.0	0.0
111030	1.6	7.0	0.3	0.0	–	6.2	–	0.30	0.0	100.0	0.0
111336	1.7	2.2	0.6	0.0	1.2	2.9	0.43	0.51	28.0	72.0	0.0
114933	1.6	4.7	0.9	0.0	–	4.2	–	0.88	0.0	100.0	0.0
116891	0.6	3.1	0.5	21.0	–	3.0	–	0.50	0.0	84.0	16.0
118757	0.7	6.4	0.7	0.0	–	7.0	–	0.71	0.0	100.0	0.0
122721	2.5	1.3	0.5	0.0	1.5	–	0.51	–	100.0	0.0	0.0
103749	3.4	1.5	0.8	0.0	1.0	4.1	0.66	0.33	69.0	31.0	0.0
103751	2.1	1.4	0.8	0.0	0.7	2.1	0.81	0.64	46.0	54.0	0.0
107730	4.0	1.2	0.8	0.0	1.2	–	0.78	–	100.0	0.0	0.0
111461	1.3	2.4	0.8	15.0	0.8	3.0	0.32	0.80	36.0	64.0	0.0
111782	0.7	4.7	0.5	0.0	–	5.0	–	0.46	0.0	100.0	0.0
119679	3.6	0.8	0.8	0.0	0.8	–	0.80	–	100.0	0.0	0.0
123325	1.2	1.1	0.9	26.0	–	1.2	–	0.88	0.0	70.0	30.0
100894	0.7	4.0	0.7	0.0	–	4.4	–	0.66	0.0	100.0	0.0
107689	2.9	2.8	0.8	0.0	2.1	3.8	0.90	0.59	67.0	33.0	0.0
108249	20.0	1.6	0.7	0.0	0.4	19.5	0.76	0.31	82.0	18.0	0.0
108777	2.1	5.0	0.5	0.0	8.8	–	0.49	–	100.0	0.0	0.0
115620	0.7	7.8	0.4	0.0	–	8.4	–	0.38	0.0	100.0	0.0
117347	0.7	3.5	0.8	17.0	–	3.6	–	0.73	0.0	85.0	15.0
121641	1.6	2.0	0.8	0.0	0.8	2.5	0.30	0.79	20.0	80.0	0.0
100858	0.5	4.2	0.6	0.0	–	4.5	–	0.67	0.0	100.0	0.0
102168	3.8	1.8	0.6	0.0	1.3	4.4	0.65	0.52	82.0	18.0	0.0
104794	1.5	3.8	0.4	0.0	–	3.5	–	0.44	0.0	100.0	0.0
110029	0.3	4.6	0.6	0.0	–	5.3	–	0.66	0.0	100.0	0.0
116835	2.5	0.9	0.9	0.0	0.6	1.7	0.66	0.71	59.0	41.0	0.0
119583	0.5	3.0	0.9	0.0	–	3.4	–	0.90	0.0	100.0	0.0
121896	2.7	1.1	0.5	0.0	1.8	0.9	0.40	0.57	58.0	42.0	0.0
109051	2.1	6.0	0.6	0.0	4.7	5.2	0.18	0.89	30.0	70.0	0.0
112374	0.9	1.5	0.9	0.0	–	1.5	–	0.93	0.0	100.0	0.0
114727	2.1	2.1	0.3	0.0	1.9	2.5	0.54	0.19	55.0	45.0	0.0
102387	2.8	0.7	0.6	0.0	1.3	0.6	0.56	0.54	42.0	58.0	0.0
110626	1.2	4.4	0.8	0.0	–	4.1	–	0.78	0.0	100.0	0.0
116591	1.5	1.8	0.8	0.0	0.6	2.0	0.14	0.80	17.0	83.0	0.0
116644	1.5	1.2	0.6	17.0	–	1.4	–	0.65	0.0	75.0	25.0
101298	7.8	2.5	0.8	0.0	2.7	–	0.83	–	84.0	0.0	16.0
108854	4.2	11.2	0.4	16.0	0.9	10.6	0.60	0.34	50.0	50.0	0.0
111731	19.9	0.7	0.6	0.0	4.7	0.5	0.46	0.01	42.0	58.0	0.0
109877	1.9	1.9	0.9	0.0	1.1	2.4	0.73	0.83	37.0	63.0	0.0
111146	5.5	1.0	0.9	0.0	0.7	5.2	0.88	0.53	83.0	17.0	0.0
111909	1.4 *	5.9	0.8	0.0	4.8	6.9	0.35	0.67	22.0	78.0	0.0
123324	1.1	2.8	0.8	10.0	–	2.8	–	0.81	0.0	89.0	11.0
107752	1.1	1.6	0.8	0.0	–	1.6	–	0.75	0.0	100.0	0.0
111836	0.9	2.5	0.9	0.0	–	2.5	–	0.94	0.0	100.0	0.0

Table D2 – *continued*

ID	n	r_e (kpc)	Axial ratio	PSF (per cent)	Bulge r_e (kpc)	Disc r_e (kpc)	Bulge axial ratio	Disc axial ratio	Bulge (per cent)	Disc (per cent)	PSF (per cent)
119585	1.9	1.4	0.8	13.0	1.1	2.0	0.63	0.56	70.0	30.0	0.0
103664	1.3 *	4.2	0.7	0.0	–*	4.1	–	0.69	0.0	100.0	0.0
107610	0.3	4.8	0.4	0.0	–	5.5	–	0.33	0.0	100.0	0.0
100564	2.6	1.9	0.9	21.0	1.5	3.4	0.75	0.59	67.0	18.0	14.0
101313	1.7	1.1	0.5	0.0	–	1.3	–	0.47	0.0	87.0	13.0
101818	1.1	2.5	0.8	0.0	–	2.5	–	0.85	0.0	100.0	0.0
109082	2.8	0.9	0.9	0.0	1.0	1.0	0.85	0.70	76.0	24.0	0.0
109262	1.2	2.4	0.7	14.0	–	2.4	–	0.67	0.0	84.0	16.0
114138	2.2	3.1	0.8	0.0	1.7	4.3	0.80	0.60	41.0	59.0	0.0
104698	2.0	2.9	0.7	0.0	7.3	1.9	0.51	0.81	50.0	50.0	0.0
101714	4.0	1.1	0.6	0.0	1.1	–	0.64	–	100.0	0.0	0.0
103841	0.9 *	68.7	0.1	36.0	–	0.0	–	0.05	0.0	100.0	0.0
108887	3.9	1.0	0.4	0.0	1.0	–	0.39	–	100.0	0.0	0.0
108892	9.7	5.3	0.8	0.0	0.9	6.4	0.60	0.88	65.0	35.0	0.0
115739	0.1	4.0	0.6	0.0	–	5.0	–	0.52	0.0	100.0	0.0
113904	1.2	3.4	0.7	20.0	–	3.4	–	0.71	0.0	78.0	22.0
121971	2.2	1.4	0.5	0.0	1.5	1.7	0.78	0.25	59.0	41.0	0.0
110871	0.8	4.2	0.6	0.0	–	4.4	–	0.60	0.0	100.0	0.0
108716	19.7	1.0	0.6	0.0	0.6	–	0.59	–	100.0	0.0	0.0
104392	0.6	5.7	0.3	0.0	–	6.4	–	0.27	0.0	100.0	0.0
121395	4.1 *	0.0	0.9	0.0	0.0	–	1.00	–	100.0	0.0	0.0
117233	1.0	4.9	0.5	12.0	0.6	5.2	0.23	0.55	18.0	82.0	0.0
120369	2.4	0.9	0.4	0.0	5.3	1.2	0.17	0.41	11.0	67.0	22.0
114460	19.3 *	96.6	0.4	0.0	1.3	23.0	0.48	0.29	68.0	32.0	0.0
115338	0.8	3.4	0.6	10.0	–	2.8	–	0.64	0.0	100.0	0.0
101548	0.7	2.6	0.7	0.0	–	2.6	–	0.74	0.0	100.0	0.0
110846	3.4	1.1	0.7	0.0	1.5	0.9	0.55	0.03	85.0	15.0	0.0
101885	20.0	2.4	1.0	0.0	10.0	–	0.51	–	51.0	0.0	49.0
106767	3.2	1.6	0.3	0.0	1.8	–	0.31	–	100.0	0.0	0.0
116142	1.1	4.7	0.6	14.0	0.4	5.1	0.35	0.66	21.0	79.0	0.0
110731	1.9	1.2	0.5	30.0	0.7	–	0.49	–	100.0	0.0	0.0
122586	2.6	1.3	0.4	0.0	1.0	1.9	0.28	0.44	66.0	34.0	0.0
107762	0.9	1.8	0.8	10.0	–	1.5	–	0.76	0.0	100.0	0.0

SUPPORTING INFORMATION

Additional Supporting Information may be found in the online version of this article:

Table S1. Machine-readable table combining data from Tables D1 and D2.

Please note: Wiley-Blackwell are not responsible for the content or functionality of any supporting materials supplied by the authors. Any queries (other than missing material) should be directed to the corresponding author for the article.

This paper has been typeset from a TEX/LATEX file prepared by the author.